Polymorphism in small organic compounds

Laura Elizabeth Budd

A thesis presented for the degree of Doctor of Philosophy in the College of Science and Engineering at the University of Edinburgh
2009

Declaration

This thesis has been entirely written by me and has not previously been submitted for any degree at this or any institution. The work detailed in this thesis is my own except where specific reference is made to the work of another.

Laura Budd

Abstract

The effect of temperature on the crystal structure of deuterated piperidine has been studied using neutron powder diffraction. Differential scanning calorimetry indicates that there are multiple phases accessible *via* changes in temperature however there is no evidence of this in the neutron powder diffraction study with only one phase observed in the range 2 – 250 K and under various crystallisation conditions. The effect of pressure up to 2.79 GPa has also been determined. The compression of the structure is facilitated through the closing up of voids in the structure and no phase transition is observed.

Differential scanning calorimetry has shown N-methyl and N,N-dimethylformamide both exhibit a thermal event prior to melting. Low temperature neutron powder diffraction has shown these transitions are associated with the onset of methyl group rotation.

Neutron powder diffraction studies show formamide exhibits remarkable polymorphism at ambient temperature and pressures between 0.1 GPa and 3.6 GPa, forming four new polymorphs. All the structures consist of N-H…O hydrogen bonded chains. The formation of the various polymorphs can be rationalised in terms of the orientation of the molecules within the hydrogen bonded chains and the resultant structures formed by further hydrogen bonds between the chains. This is in stark contrast to the effect of varying conditions of temperature where only one structure exists from 2 K right up to the melting point.

The effect of temperature on the crystal structure of pyrazine in the range 8 – 315 K is described. At temperatures below 90 K the structure undergoes a phase transition to a previously uncharacterised phase, designated phase IV, which is closely related to the previously known phase I. The crystal structure of phase III has been determined at 315 K. The crystal structure of pyrazine has been determined at room temperature at pressures between 0.11 GPa and 9.36 GPa. At 0.94 GPa a transition

from phase I to phase IV is observed. This is the same phase as observed at low temperatures.

Crystal growth at 215 K results in the formation of two different phases of mesitylene; phase II and a new previously unknown phase designated phase IV. The structure of phase IV has been determined and found to be stable in the range 90 – 221 K. On cooling a crystal of deuterated mesitylene in phase II to 90 K a transition to phase III was observed and the resultant crystal structure is closely related to that of phase II.

Acknowledgements

Firstly, I would like to thank my supervisor Simon Parsons for all his help and advice over the last four years and for giving me the opportunity to do this project in the first place. I would also like to thank my second supervisor Richard Ibberson for his help and useful chats. Without Richard and Bill Marshall, most of the data in this thesis would not have been collected so many thanks to you both.

The members of the crystallography group, past and present, have definitely had their part to play in getting me through these four years. There are too many of you to list everyone, but Fraser, Steve, Anna and Russell in particular deserve a mention for their advice and for helping me keep things in perspective.

Anna and Helen are responsible for getting me addicted to knitting but have provided plenty of good food and been great friends over the last few years so I will let them off!

Many thanks to my family for all their support over the years, in particular for putting up with me these last few months. Finally, I would like to say a huge thank-you to Rob for putting up with me all this time and for just being Rob! Without him I wouldn't have moved to Edinburgh in the first place and I definitely wouldn't have got through the last four years without him. Cheers Bobster!

Lecture Courses and Meetings Attended

Courses

Sep. 2005	Basic Radiation Protection course	Edinburgh
Sep. 2005	Laser Safety course	Edinburgh
Jan. 2006	ISIS Neutron Training course	ISIS
May 2006	EaStChem Academic Paper Writing course	St Andrews
Sep. 2006	EPSRC Advanced Refinement Techniques course	Southampton
Jan. 2007	PCG Rietveld Refinement School	Durham
Mar. 2007	BCA/CCG Intensive Crystallography School	Durham
Oct. 2007	SHELX workshop	Gottingen

Meetings Attended

Nov. 2005	BCA/CCG Autumn Meeting	Daresbury	
Apr. 2006	BCA Spring Meeting	Lancaster	Poster
Apr. 2007	BCA Spring Meeting	Canterbury	Poster
Oct. 2007	Bruker User Meeting	Gottingen	
Apr. 2008	BCA Spring Meeting	York	Poster

Contents

Chapter 1
Introduction

1.1 Introduction

The ability to understand and predict the relationship between structure and function is one of the key challenges of chemistry. Development of *ab initio* methods allows the structure of an individual molecule to be predicted, however predicting solid state structures is an entirely different matter. The arrangement of molecules in three-dimensions is the result of the balance between the magnitude and nature of both intra- and inter-molecular interactions. If we are to understand and predict solid state structures, then a detailed understanding of the interplay between these interactions is surely a key component.

A unique feature of the solid state is the ability to exhibit polymorphism; the ability for the same compound to crystallise with different three-dimensional packing arrangements. There may be a number of different ways in which a molecule can pack, resulting in a range of different intermolecular interactions. The properties of a material in the solid state depend on its structure, therefore different polymorphs of a compound can have different properties including melting point, solubility and thermal stability (Bernstein, 2002). The variation in properties between polymorphs means that the phenomenon of polymorphism is of interest in many research areas, in particular materials science and the pharmaceutical industry where there is a desire to have control over the properties of a compound. In the case of a pharmaceutical compound, a difference in solubility between polymorphs may affect the bioavailability of a drug and consequently have implications for dosage administration. Polymorphs can even be patented separately. Understanding the factors which determine the formation of different polymorphs is therefore an important industrial and academic research area.

There are many experimental conditions to consider when determining the conditions under which polymorphs form. Indeed, experimental approaches to polymorph searching often involve performing exhaustive crystallisations under a variety of conditions. Typically the temperature and choice of solvent are varied. The thermodynamic variable of pressure is not extensively used despite its potential for affecting the structure. Consider the Gibbs free energy:

$$G = U + PV - TS$$

where the terms have their usual thermodynamic meanings. For organic compounds, the temperature range accessible is typically limited to approximately 500 K before decomposition occurs. By comparison, a pressure of 1 GPa (= 9869 atm) represents an increase of four orders of magnitude relative to ambient pressure. By the standards of modern high pressure science, this is a somewhat modest figure; therefore pressure is a powerful thermodynamic variable in the search for polymorphs.

The ability to predict accurately the crystal structure of a molecule and any polymorphs prior to any crystallisation experiments falls into the field of crystal structure prediction and is addressed by a number of research groups (Lommerse *et al.*, 2000; Day *et al.*, 2005; Motherwell *et al.*, 2002). The success of crystal structure prediction is influenced by a number of factors, in particular the ability to accurately model intermolecular interactions. While interactions such as hydrogen bonds are strongly directional, others such as van der Waals interactions arise from effects which are much harder to model. Consequently, the computational models are highly complex. Despite this, the calculation of the lattice energies of the predicted structures needs to be more accurate than the difference between the correct structure and the other possible structures which may only be a few kJ mol^{-1}. Add to this conformational flexibility of the molecule and the number of plausible structures generated which are close in energy can be numerous. Whether or not the correct structure was predicted is determined relative to the experimentally observed structure. Of course it is possible that the observed structure may not be the most thermodynamically stable structure and there may be other polymorphs not yet discovered.

The three-dimensional packing of molecules in the solid state depends on the balance of competing intermolecular interactions. By choosing simple, small model molecular systems it is possible to study these fundamental interactions in isolation. Although intermolecular interactions such as hydrogen bonds and van der Waals

interactions are observed in many compounds, mono-functional small organic molecules have the advantage of allowing a single type of interaction to be studied in the absence of other effects. Such simple molecules are also more amenable to high level theoretical calculations and could provide crucial information for developing computational techniques for predicting the solid state and understanding more complex systems. Intermolecular interactions are distance dependent, therefore perturbing the structure by modifying these distances *via* changes in the temperature or pressure provides information about the nature of the interaction and an effective way of searching for polymorphs.

Structural studies on seemingly simple compounds, including acetone (Allan *et al.*, 1999) and cyclohexane (Kahn *et al.*, 1973; Pravica *et al.*, 2007; Wilding *et al.*, 1993), have shown that they can exhibit rich phase behaviour under conditions of varying temperature or pressure. Simple molecules can therefore potentially provide a wealth of information on intermolecular interactions and studying the phase behaviour of small simple organic compounds forms the basis of this thesis. For each of the compounds studied in this thesis there is evidence of interesting phase behaviour which is yet to be fully characterised.

The crystal structure of piperidine has previously been determined at low temperature by X-ray single crystal diffraction (Parkin *et al.*, 2004), however differential scanning calorimetry (DSC) indicated the presence of other phases accessible *via* changes in temperature. Neutron powder diffraction studies have been undertaken to characterise the behaviour of deuterated piperidine from 2 K right up to the melting point. The crystal structure at high pressure has also been investigated. DSC traces of N-methyl- and N,N-dimethyl-formamide show the presence of an endothermic transition on heating in each compound (Dawson, 2003) though the nature of the transitions has not been characterised. The low temperature behaviour of these compounds has been studied *via* neutron powder diffraction to allow subtle changes in the structures to be characterised. Although the crystal structure of formamide at low temperature has been studied on several occasions (Ladell & Post, 1954; Stevens, 1977), the crystal structure at high pressure has not been well studied

despite evidence of a phase transition at 5 GPa based on Raman spectroscopy data (Shimizu *et al.*, 1988). The effect of pressure on the crystal structure of formamide has therefore been investigated. Pyrazine is known to exhibit rich phase diversity (Bougeard *et al.*, 1978) yet little structural information is known. Variable temperature and high-pressure neutron powder diffraction studies have been performed in order to fully characterise the phase behaviour of pyrazine. Interest in the structure and dynamics of mesitylene in the solid state has been fuelled by its potential use as a neutron moderator (Utsuro & Sugimoto, 1977; Unlu *et al.*, 1995) and has led to several experimental studies employing a wide variety of techniques. Despite this, the behaviour of mesitylene at low temperatures is still not fully understood. With this in mind, X-ray single crystal studies have been performed with the aim of fully characterising all the polymorphs of mesitylene.

The remainder of this chapter will discuss the experimental techniques employed in the work described in this thesis.

1.2 Experimental techniques

The use of a variety of complementary experimental techniques is often essential if we are to fully characterise the phase behaviour of a compound. This section discusses the experimental and structural analysis methods employed in the studies described in this thesis.

1.2.1 Differential scanning calorimetry

Differential scanning calorimetry (DSC) is a powerful technique for determining the presence of temperature induced transitions in a sample. The amount of energy absorbed or released as the sample is heated, relative to a reference material, is measured as a function of temperature. When the sample undergoes a physical transformation more or less energy, depending on the nature of the transformation, is required to maintain the sample and reference material at the same temperature. The resultant curve is a measure of heat flow as a function of temperature. By convention, endothermic events are depicted as positive peaks. A DSC trace displaying typical features is shown in Figure 1.1.

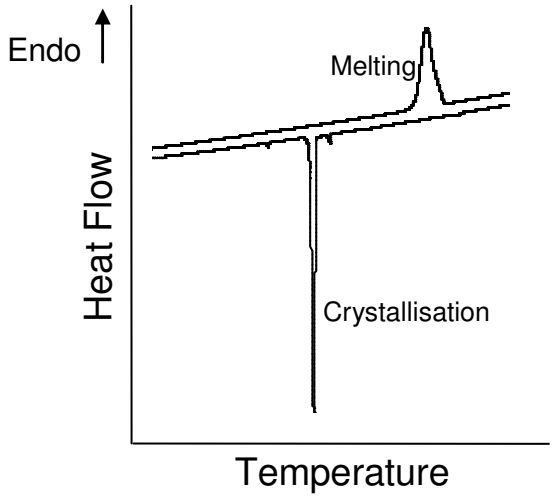

Figure 1.1 Typical features of a DSC trace.

While DSC can be used to measure a variety of properties of a sample, the main application is in the study of phase transitions. The ability to determine crystallisation temperature, melting temperature and transition temperatures for a sample makes DSC a valuable tool in determining the phase diagram for compounds and it is often used in conjunction with variable temperature diffraction studies. It is also possible to measure the enthalpy change associated with a transition, ΔH_{trans}.

1.2.2 X-ray Single crystal diffraction

While X-ray single crystal diffraction is the method of choice for determining the crystal structure of many compounds, one disadvantage of simple organic molecules is that they are often liquids or gases under ambient conditions. Consequently single crystals of these compounds have to be grown *in situ*. In general, there are two methods for growing a single crystal *in situ*; either through careful control of the temperature or using the laser assisted zone refinement method of Boese and Nussbaumer (1994). In either case, the liquid sample is loaded into a capillary and sealed before being mounted on a conventional diffractometer. The sample is then flash frozen using liquid nitrogen. A single crystal can be grown through careful manipulation of the temperature *via* the cryostream; melting the sample until only one seed crystallite remains and allowing it to grow as the sample cools slowly. Alternatively, the laser assisted zone refinement method can be employed. An infra-

red carbon dioxide laser is used to heat the sample, with the power and position of the laser computer controlled. By manipulating the power of the laser and the time taken to move the laser along the capillary, the flash-frozen solid is carefully annealed to form a single crystal over a period of several hours. The laser-assisted method has been used to successfully grow single crystals of a variety of low melting compounds including nitrobenzene (Boese *et al.*, 1992), cyclobutanol (McGregor *et al.*, 2005), monofluoro- and monochloro-phenols (Oswald *et al.*, 2005) and even ammonia (Boese *et al.*, 1997).

X-ray single crystal diffraction measurements can be performed at high pressures using a standard diffractometer *via* the use of a Merrill-Bassett diamond-anvil cell (Merrill & Bassett, 1974). A similar method to the careful manipulation of temperature used to grow single crystals at low temperatures can be used to grow a single crystal at high pressure inside the diamond anvil cell. The liquid sample is loaded into the cell and pressure applied to form a polycrystalline mass. The cell is heated to melt the sample until a single seed crystallite remains. A single crystal then grows from the cooling melt at high pressure. The diamond anvil cell can then be attached to a normal goniometer head. The success of this method for obtaining a single crystal of a compound which is liquid under ambient conditions is exemplified by studies of, amongst other compounds, methanol (Allan *et al.*, 1998), ethanol and acetic acid (Allan & Clark, 1999).

Despite development of these methods, growing a single crystal of a compound which is liquid under ambient conditions can be difficult or not always possible. Even if a single crystal suitable for structure determination can be obtained, the crystal may lose crystallinity during a phase transition; thus the sample is no longer suitable for data collection. Studies of phase behaviour in the solid state often combine X-ray single crystal diffraction with complementary powder diffraction investigations. Neutron powder diffraction is particularly useful in studies of small organic compounds with single crystal diffraction used for structure solution and initial refinement and neutron powder diffraction used for refinement of subtle structural details.

1.2.3 Powder diffraction

Powder diffraction is a powerful technique, particularly useful for the study of polymorphism. As discussed above, growing a suitable single crystal can be difficult, particularly for low melting point compounds; however it can be relatively straightforward to obtain a crystalline powder suitable for powder diffraction. Despite the relative ease of sample preparation, consideration of preferred orientation and particle size effects is important especially when preparing low melting point materials. Simply freezing the sample directly from the liquid phase *in situ* promotes the growth of large crystallites resulting in significant preferred orientation effects. A number of techniques have been developed to overcome this effect with varying degrees of success. The inclusion of an appropriate material, such as glass wool, in the sample container facilitates the formation of small crystallites though this can be of limited success. The technique of freezing and hand grinding the sample using a liquid nitrogen chilled stainless steel mortar (Ibberson, 1996) is a straightforward way of preparing high quality powder samples from materials which are liquid under ambient conditions.

Neutron powder diffraction, in particular, is extremely useful for investigating the phase behaviour of organic compounds as phase transitions are often the result of changes in the positions of hydrogen atoms. Accurate location of hydrogen atoms is often very difficult or even impossible using X-ray data, however not only can their location be determined precisely from neutron data but their positions and anisotropic displacement parameters can also be refined. Unlike X-rays which interact with electrons, neutrons interact with the nucleus of an atom. Consequently, the scattering power of an atom is not strongly related to its atomic number and indeed the neutron scattering powers vary erratically across the periodic table. In terms of studying organic compounds, one of the key advantages of this is the ability to accurately locate light atoms, such as hydrogen, in the presence of much heavier atoms. As the neutrons interact with the nucleus of an atom, isotopes of the same element often have very different scattering powers. For example, hydrogen has a large incoherent scattering cross-section whereas deuterium has a relatively large

coherent scattering cross-section. As a result, samples for neutron diffraction must be deuterated.

The nature of the interaction between the neutron and the nucleus of an atom means that, unlike X-rays, the scattering power of neutrons does not fall off with scattering angle. For stationary atoms the neutron scattering power of an atom is almost constant, whereas for X-rays it falls off rapidly, Figure 1.2. Neutron diffraction is therefore ideal for high resolution studies and consequently determination of highly precise structures. Accurate determination of anisotropic displacement parameters allows an assessment of the effect of thermal motion on the structure to be made, particularly for bonds involving hydrogen atoms.

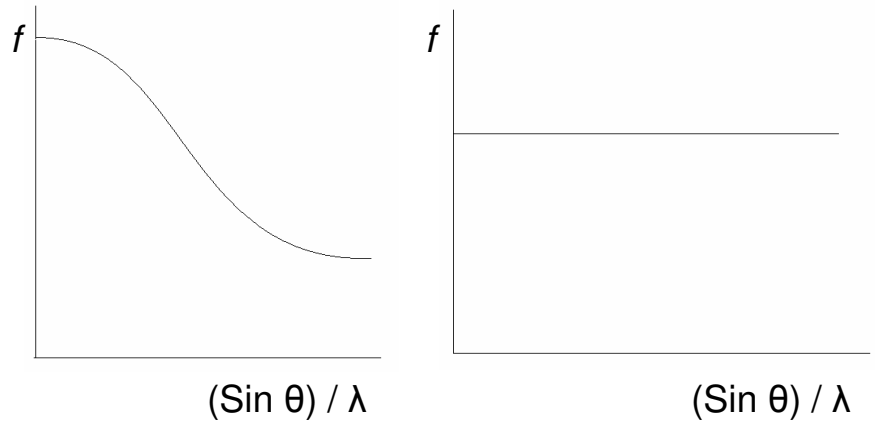

(a) X-ray (b) Neutron

Figure 1.2 Scattering factors as a function of scattering angle.

The interaction of a neutron with a nucleus is weak, therefore large sample volumes are required. Consequently, powder averaging is better than for X-ray methods which typically have smaller sample volumes. The weak interaction with nuclei makes neutrons a highly penetrating probe. This feature means the use of complex sample environment equipment such as cryostats for low temperature studies and the Paris-Edinburgh cell (Besson *et al*., 1992) for high pressure studies is widely applied.

1.2.4 Structure solution and refinement

From an experimental perspective, the use of powder diffraction rather than single crystal diffraction has a number of advantages; however from a refinement perspective the use of powder diffraction alone is not necessarily straightforward. Some of the difficulties encountered are discussed below.

1.2.4.1 Indexing and structure solution

Indexing and structure solution from good quality single crystal data is now considered almost routine. In a powder pattern the information contained in the spatial distribution of the reflections is lost, with all the data collapsed into a single dimension. As a result, indexing of a powder pattern and the extraction of specific intensities for structure solution is often difficult or impossible due to overlapping reflections and the resulting ambiguity in the data. Consequently it is often difficult to index, and subsequently solve, an unknown structure from powder diffraction alone.

In cases where there are relatively few reflections in the powder pattern there may be very little or no overlap of reflections in which case it is possible to index the pattern and extract intensities which can be used in Patterson or direct methods for structure solution as with single crystals. If the pattern can be indexed but peak overlap is sufficient that individual intensities cannot be extracted then structure solution by global optimisation strategies may be possible, the most widely used of which is simulated annealing. Instead of extracting individual intensities, random structural models are generated and their calculated powder patterns tested against the experimental data. A Monte-Carlo procedure is used to generate a random model by making stepwise changes to the structural parameters. This may result in either a better fit or a worse fit between the calculated and observed powder patterns. The fact that the new model may give a worse fit is crucial as it allows escape from local minima. The tolerance for changes which result in a worse fit is gradually reduced as the minimisation proceeds until steps in both directions are exhausted. By employing chemical knowledge of the molecular connectivity, an internal coordinate system can

be used to describe the molecule as a rigid body. Thus the number of structural parameters to be varied is reduced

1.2.4.2 Structure refinement

The Rietveld method (Rietveld, 1969) of structural refinement overcomes the problem of overlapping reflections by refining against the whole pattern, rather than considering each reflection individually. One drawback is that more parameters are required for Rietveld refinement than for single crystal refinement, for example to model the background and profile functions. Both of these would be dealt with during integration of single crystal data, not included in the refinement model. The real drawback is of course the loss of information associated with collapsing three dimensional information into one dimension.

With single crystal data it is possible to freely refine many parameters simultaneously early on in the refinement, such as atomic coordinates and anisotropic displacement parameters for every atom. Considerably more care is required with the model used in structural refinement against powder diffraction data; allowing the atomic coordinates and anisotropic displacement parameters to refine freely for each atom often results in dissociation of molecules or physically unreasonable parameters, particularly if the starting model is inadequate. Various techniques can be employed to reduce the number of parameters being refined and maintain a physically reasonable model.

1.2.4.3 Rigid bodies

A popular method is to treat small molecules or ions as rigid bodies. This can be achieved either by using a Z-matrix or by using fractional, or Cartesian, coordinates. The work presented in this thesis has made use of Cartesian coordinates for planar molecules and Z-matrices for non-planar molecules. In both models, chemical knowledge of the molecular arrangement is used to define each atom in terms of bond lengths and bond angles. As a result, the number of parameters required to describe the positions of the atoms is reduced from three parameters per atom to just six for the whole molecule; three translation parameters for the position and three

rotation parameters for the orientation of the molecule in the asymmetric unit. Even for a small organic molecule such as N,N-dimethylformamide, employing the rigid body model reduces the number of parameters describing position and orientation of the molecule by 30, down from 36. The implementation of rigid body refinement in TOPAS-Academic (Coelho, 2007) also allows individual parameters in the Z-matrix to be refined easily.

1.2.4.4 TLS model of thermal motion

In reality atoms in a crystal are vibrating about their equilibrium positions and a displacement parameter can be refined for each atom to describe this motion. Refining a single parameter for each atom assumes that the atom is vibrating equally in all directions (isotropic motion). However, typically atoms vibrate by differing amounts in different directions (anisotropic motion). Usually six displacement parameters are refined for each atom to describe this motion; one for each axis and three cross-terms. This results in nine refined parameters for each independent atom; three positional parameters and six displacement parameters. For N,N-dimethyl formamide this gives a total of 108 parameters per molecule.

During refinement the anisotropic displacement parameters, U_{ij} parameters, are usually treated as independent variables with any correlation that may exist between the U_{ij} parameters of different atoms in the asymmetric unit ignored. If the crystal contains almost rigid groups of atoms, such as molecules, the translational and librational motions of these groups introduce strong correlations among the U_{ij} parameters of different atoms. If the groups were truly rigid then the U_{ij} parameters would be entirely determined by these translational and librational motions. In reality, molecules are not truly rigid, however any contribution from internal vibrations is generally much smaller than those from translational and librational motions and it is therefore reasonable to use a rigid body approximation.

Cruickshank (1956) analysed the rigid body motion of molecules in crystals in terms of two symmetric tensors; one for translation, T, and one for libration, L. In the original analysis it was assumed that the librational axes are orthogonal and intersect

at the origin of the coordinate system. Schomaker and Trueblood (1968) later showed that the assumption of intersecting librational axes is not necessarily correct unless the existence of an intersection point is a result of crystal symmetry.

The most general motion of a rigid body is a screw motion; a rotation about an axis, coupled with a translation parallel to this axis. The libration tensor, L, for this motion is independent of any assumptions about the positions of the libration axes, however the translational tensor, T, varies depending on the assumptions made about the position of the libration axes. Thus, in this two tensor analysis the calculated U_{ij} values will depend on the choice of origin. Schomaker and Trueblood (1968) overcame this difficulty by introducing a third tensor, S, to account for this screw type motion arising from correlation between libration and translation. Inclusion of this tensor means that the calculated U_{ij} values are independent of the origin chosen however the components of the T and S tensors will vary with the choice of origin. There is therefore an inherent element of arbitrariness in the description of the rigid body motion; however to eliminate this, the origin is chosen so as to make S symmetric and to include a standard constraint to make the equations determinate (trace (S) = 0). If the molecular centre is situated on a crystallographic inversion centre, the S tensor is zero and the analysis reduces to Cruickshank's original two tensor model.

In terms of the T, L and S tensors the displacement parameters can be written as

$$U_{ij} = G_{ijkl}L_{kl} + H_{ijkl}S_{kl} + T_{ij}$$

where G_{ijkl} and H_{ijkl} are arrays involving the atomic coordinates (Dunitz, 1995), Table 1.1. The resultant equations for each of the displacement parameters are given below, where *x, y* and *z* are Cartesian coordinates in the local system of the TLS model. .

$$U_{11} = z^2L_{22} + y^2L_{33} - 2yzL_{23} - 2yS_{31} + 2zS_{21} + T_{11}$$

$$U_{22} = z^2L_{11} + x^2L_{33} - 2xzL_{31} - 2zS_{12} + 2xS_{32} + T_{22}$$

$$U_{33} = y^2L_{11} + x^2L_{22} - 2xyL_{12} - 2xS_{23} + 2yS_{13} + T_{33}$$

$$U_{23} = -yzL_{11} - x^2L_{23} + xyL_{31} + xzL_{12} - xS_{22} + xS_{33} + yS_{12} - zS_{13} + T_{23}$$

$$U_{31} = -xzL_{22} + xyL_{23} - y^2L_{31} + yzL_{12} + yS_{11} - yS_{33} + zS_{23} - xS_{21} + T_{31}$$

$$U_{12} = -xyL_{33} + xzL_{23} + yzL_{31} - z^2L_{12} - zS_{11} + zS_{22} + xS_{31} - yS_{32} + T_{12}$$

Analysis of the thermal motion of rigid bodies *via* the TLS method reduces the number of refined parameters to describe the thermal motion of a molecule to 20; 3 positional parameters to describe the centre of action, 6 elements of the T tensor, 6 elements of the L tensor and 5 elements of the S tensor. In the case of N,N-dimethyl formamide, adopting the TLS model reduces the number of refined displacement parameters from 72 per molecule to just 20 per molecule.

G_{ijkl} *ij*	*kl*	11	22	33	23	31	12
11		0	z^2	y^2	$-2yz$	0	0
22		z^2	0	x^2	0	$-2xz$	0
33		y^2	x^2	0	0	0	$-2xy$
23		$-yz$	0	0	$-x^2$	xy	xz
31		0	$-xz$	0	xy	$-y^2$	yz
12		0	0	$-xy$	xz	yz	$-z^2$

H_{ijkl} *ij*	*kl*	11	22	33	23	31	12	32	13	21
11		0	0	0	0	$-2y$	0	0	0	$2z$
22		0	0	0	0	0	$-2z$	$2x$	0	0
33		0	0	0	$-2x$	0	0	0	$2y$	0
23		0	$-x$	x	0	0	y	0	$-z$	0
31		y	0	$-y$	z	0	0	0	0	$-x$
12		$-z$	z	0	0	x	0	$-y$	0	0

Table 1.1 The arrays G_{ijkl} and H_{ijkl} used in the equation $U_{ij} = G_{ijkl}L_{kl} + H_{ijkl}S_{kl} + T_{ij}$ (Dunitz, 1995).

The TLS model assumes that the axes are orthogonal. However, in the case of monoclinic and triclinic structures this is not true. It is therefore necessary to convert from crystal fractional coordinates to Cartesian coordinates, using the following matrix:

$$A = \begin{bmatrix} a & b\cos\gamma & c\cos\beta \\ 0 & b\sin\gamma & \dfrac{c(\cos\alpha - \cos\beta\cos\gamma)}{\sin\gamma} \\ 0 & 0 & \dfrac{c\nu}{\sin\gamma} \end{bmatrix}$$

where $\nu = \dfrac{V}{abc}$.

The corresponding matrix for converting from orthogonal coordinates to crystal coordinates is:

$$B = \begin{bmatrix} \dfrac{1}{a} & \dfrac{-\cos\gamma}{a\sin\gamma} & \dfrac{\cos\gamma\cos\alpha - \cos\beta}{a\nu\sin\gamma} \\ 0 & \dfrac{1}{b\sin\gamma} & \dfrac{\cos\gamma\cos\beta - \cos\alpha)}{b\nu\sin\gamma} \\ 0 & 0 & \dfrac{\sin\gamma}{c\nu} \end{bmatrix}$$

The U_{ij} parameters are evaluated in the Cartesian frame before being converted back to the crystal axis frame using the following:

$$U_{crystal} = D^{-1} B U_{Cartesian} B^T D^{-1}$$

where D is the diagonal matrix

$$\begin{bmatrix} a* & 0 & 0 \\ 0 & b* & 0 \\ 0 & 0 & c* \end{bmatrix}$$

The resultant equations for the conversion of the U_{ij} parameters from Cartesian to crystal axes are given below.

$$U_{11crystal} = \frac{\begin{array}{c} U_{11}\tan^2\gamma - 2U_{12}\tan\gamma + 2U_{13}\cos\beta * a * a\tan^2\gamma + \\ U_{22} - 2U_{23}\cos\beta * a * a\tan\gamma + U_{33}\cos^2\beta * a^{*2}\, a^2\tan^2\gamma \end{array}}{a^{*2}\, a^2\tan^2\gamma}$$

$$U_{22crystal} = \frac{U_{22} + 2U_{23}\cos\alpha * bb * \sin\gamma + U_{33}\cos^2\alpha * b^2 b^{*2}\sin^2\gamma}{b^2 b^{*2}\sin^2\gamma}$$

$$U_{33crystal} = U_{33}$$

$$U_{23crystal} = \frac{U_{23} + U_{33}\cos\alpha * bb * \sin\gamma}{bb * \sin\gamma}$$

$$U_{13crystal} = \frac{U_{13}\tan\gamma - U_{23} + U_{33}\cos\beta * a * a\tan\gamma}{a * a\tan\gamma}$$

$$U_{12crystal} = \frac{\begin{array}{l} U_{12}\tan\gamma + U_{13}\tan\gamma\cos\alpha * bb * \sin\gamma - U_{23}\cos\alpha * bb * \sin\gamma - U_{22} \\ + U_{23}\cos\beta * a * a\tan\gamma + U_{33}\cos\beta * a * a\tan\gamma\cos\alpha * bb * \sin\gamma \end{array}}{a * a\tan\gamma bb * \sin\gamma}$$

The contributions of the T, L and S tensors to the anisotropic displacement parameters are shown in Figure 1.3. In Figures 1.3a and b only the translation tensor is contributing to the displacement parameters. If the translation is equal in all directions, 1.3a, then the result is analogous to isotropic refinement. Introducing one term which is different results in the displacement parameters elongating in that direction, Figure 1.3b. By introducing an element of libration in a single direction, Figure 1.3c, it is evident that the whole molecule is not affected equally. The displacement parameters of the atoms close to the centre of action, the black spot, remain largely spherical, however those further away exhibit a larger amplitude of motion, elongating in one direction.

Combining the use of Z-matrix or Cartesian representations of rigid bodies with the TLS method for analysis of the anisotropic displacement parameters is particularly useful in the refinement of small organic compounds from powder diffraction data and achieves a significant reduction in the number of independent parameters refined while still fully describing the motion of the molecules.

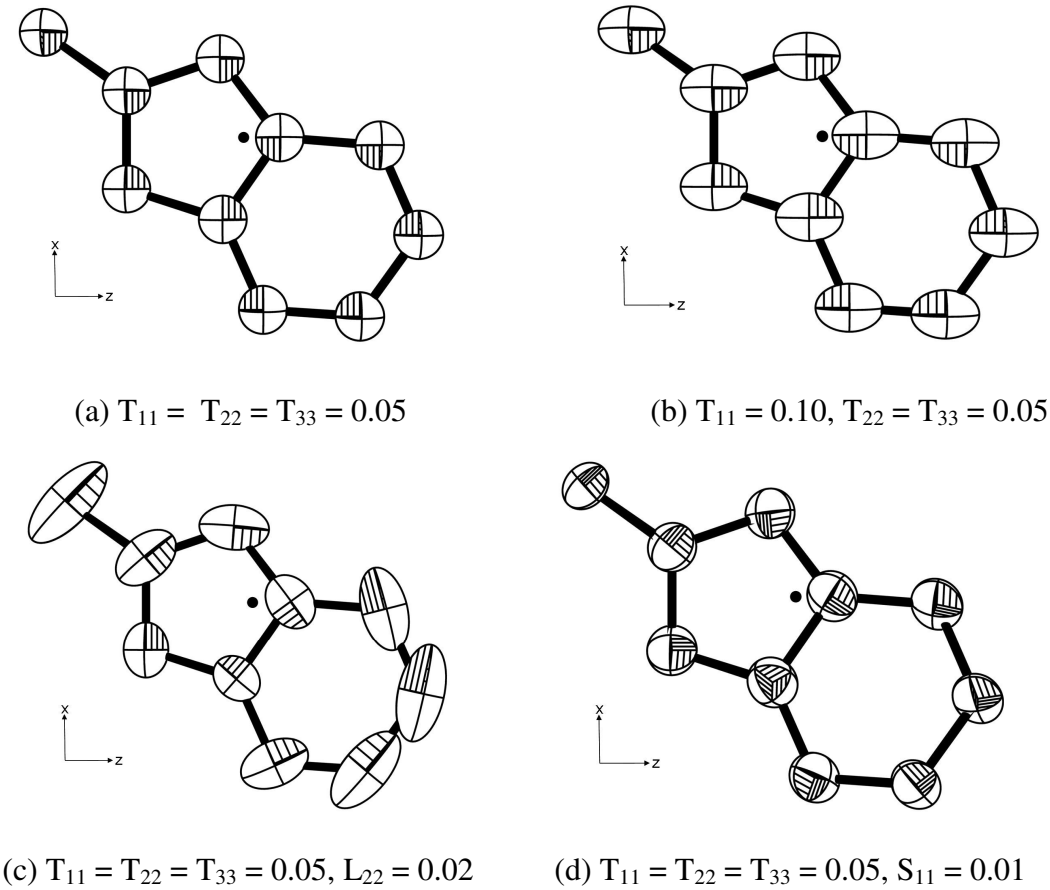

(a) $T_{11} = T_{22} = T_{33} = 0.05$ (b) $T_{11} = 0.10$, $T_{22} = T_{33} = 0.05$

(c) $T_{11} = T_{22} = T_{33} = 0.05$, $L_{22} = 0.02$ (d) $T_{11} = T_{22} = T_{33} = 0.05$, $S_{11} = 0.01$

Figure 1.3 Contribution of the T, L and S tensors to the anisotropic displacement parameters. In each figure, all terms other than those specified are zero. The centre of action corresponds to the black spot.

1.2.5 The PIXEL method

The PIXEL method, also referred to as the semi-classical density sums method, allows the calculation of intermolecular interaction energies (Gavezzotti, 2005a; Dunitz & Gavezzotti, 2005). Calculations can be performed using the OPiX package (Gavezzotti, 2003) with both full lattice and specific dimer energies computed along with a breakdown of the energies into four components: Coulombic, repulsion, dispersion and polarisation.

The geometry of the molecule is taken from the crystal structure and, if necessary, X-H distances extended to standard neutron distances (C-H 1.083 Å, N-H 1.009 Å (Desiraju & Steiner, 1999)) Without optimising the molecular geometry, an electron

density map is calculated at the MP2/6-31G** level of theory using a standard quantum chemical package such as GAUSSIAN03 (Frisch *et al.*, 2004). The result is a density map on a three dimensional grid of step size 0.08 Å. In order to speed up the subsequent calculations, the grid of pixels is condensed into super-pixels of size n x n x n, where n is the condensation level. As standard, the condensation level is set to 4 for lattice energy calculations. The resulting pixels are screened so as to remove any with a charge below a specified threshold (default 10^{-6} electrons) before renormalizing the remaining pixels so that the electrical charge balances the total nuclear charge. The next stage in the calculation is to generate the required cluster of molecules. In the case of a lattice calculation, a sphere of molecules is generated *via* the space group symmetry operations. For a small uncharged organic molecule the radius of the cluster is usually set to 18 Å. Following generation of the cluster, it is possible to begin the intermolecular energy calculations.

Coulombic energies, E_{COUL}, are calculated as the sum of pixel-pixel, pixel-nucleus and nucleus-nucleus Coulombic terms. The formula used to calculate the Coulombic energy for each interaction is the standard electrostatic potential energy for two charges, q_1 and q_2, separated by distance r:

$$E_{COUL} = \frac{q_1 q_2}{4\pi\varepsilon^o r}$$

The first stage in calculating the polarisation energy is to assign a polarisability to each pixel, α_i. Each pixel is assigned to the nearest atom in the molecule and the pixel polarisability calculated according to:

$$\alpha_i = (q_i / Z_{atom})\alpha_{atom}$$

where Z_{atom} is the number of valence electrons of the atom and α_{atom} is the polarisability of the atom. The total polarisation energy, E_{POL}, is calculated as the sum of all the pixel contributions, $E_{POL,i}$, which are calculated using the following damped formula:

$$E_{POL,i} = -\frac{1}{2}\alpha_i [\varepsilon_i d_i]^2$$

$$d_i = \exp[-\varepsilon_i / (\varepsilon_{\max} - \varepsilon_i)]$$

where ε_i is the electric field at pixel i exerted by surrounding molecules. The damping parameter, ε_{max}, is an adjustable empirical parameter optimised for organic structures. If $\varepsilon > \varepsilon_{max}$, $E_{POL,i} = 0$.

The original London formula for the dispersion energy between two molecules of polarisability α and ionisation energy E_{ION} is given by:

$$E = -\frac{3}{4}\left[\frac{\left(E_{ION}\alpha^2\right)}{\left(4\pi\varepsilon^O\right)^2\left(R_{ij}\right)^6}\right]$$

The dispersion energies, E_{DISP}, are calculated as a sum of pixel-pixel terms in a London-type formula involving the pixel polarisabilities defined above. A standard quantum mechanical damping term, $f(R)$, is included to avoid singularities arising due to very short pixel-pixel distances. The resulting expression for the dispersion energy for a two molecule interaction is:

$$E_{DISP,AB} = -\frac{3}{4}E_{ION}\sum\sum\frac{f(R)\alpha_i\alpha_j}{\left[\left(4\pi\varepsilon^O\right)^2\left(R_{ij}\right)^6\right]}$$

$$f(R) = \exp\left[-\left(D/R_{ij}-1\right)^2\right] for\ R_{ij} < D$$

$$f(R) = 1\ for\ R_{ij} > D$$

where D is the damping threshold distance parameter which is an adjustable empirical parameter.

The repulsion energy, E_{REP}, between two molecules, A & B, is obtained from the overlap of the electron densities of the two molecules, S_{AB}, according to the equation:

$$E_{REP,AB} = K\left(S_{AB}\right)^{\gamma}$$

$$S_{AB} = \sum\sum\left[\rho_i(A)\rho_j(B)\right]V$$

where K and γ are also adjustable empirical parameters. The calculation of S_{AB} uses the original uncondensed electron density grid for each of the molecules.

The total intermolecular interaction energy is then given by:

$$E_{TOT} = E_{COUL} + E_{POL} + E_{DISP} + E_{REP}$$

with four adjustable parameters (ε_{max}, D, K and γ) used in the calculations. These parameters have been optimised to reproduce experimental sublimation enthalpies for a range of organic molecular crystal structures though they can in principle be adjusted. Tests have shown that the results of PIXEL calculations compare well with the results of DFT and intermolecular perturbation theory calculations (Gavezzotti, 2005b), however PIXEL calculations are typically less computationally demanding and run quickly on an ordinary desk-top PC.

1.3 References

Allan, D. R. & Clark, S. J. (1999). *Physical Review B* **60**, 6328-6334.

Allan, D. R., Clark, S. J., Brugmans, M. J. P., Ackland, G. J. & Vos, W. L. (1998). *Physical Review B* **58**, R11809-R11812.

Allan, D. R., Clark, S. J., Ibberson, R. M., Parsons, S., Pulham, C. R. & Sawyer, L. (1999). *Chem. Commun.* 751-752.

Bernstein, J. (2002). *Polymorphism in Molecular Crystals*. Oxford: Oxford University Press.

Besson, J. M., Nelmes, R. J., Hamel, G., Loveday, J. S., Weill, G. & Hull, S. (1992). *Physica B*, **180-181**, 907-910.

Boese, R., Blaser, D., Nussbaumer, M. & Krygowski, T. M. (1992). *Struct. Chem.* **3**, 363-368.

Boese, R., Niederprum, N., Blaser, D., Maulitz, A., Anitpin, M. Y. & Mallinson, P. R. (1997). *J. Phys. Chem. B* **101**, 5794-5799.

Boese, R. & Nussbaumer, M. (1994). *Correlations, Transformations and Interactions in Organic Crystal Chemistry*. Oxford: Oxford University Press.

Bougeard, D., LeCalve, N. & Novak, A. (1978). *Molecular Crystals and Liquid Crystals* **44**, 113-124.

Coelho, A. (2007). *TOPAS-A: General Profile and Structure Analysis Software for Powder Diffraction Data.*

Cruickshank, D. W. J. (1956). *Acta. Cryst.* **9**, 754.

Dawson, A. (2003). PhD thesis, The University of Edinburgh.

Day, G. M., Motherwell, W. D. S., Ammon, H. L., Boerrigter, S. X. M., Della Valle, R. G., Venuti, E., Dzyabchenko, A., Dunitz, J. D., Schweizer, B., Van Eijck, B. P.,

Erk, P., Facelli, J. C., Bazterra, V. E., Ferraro, M. B., Hofmann, D. W. M., Leusen, F. J. J., Liang, C., Pantelides, C. C., Karamertzanis, P. G., Price, S. L., Lewis, T. C., Nowell, H., Torrisi, A., Scheraga, H. A., Arnautova, Y. A., Schmidt, M. U. & Verwer, P. (2005). *Acta Crystallographica, Section B* **61**, 511-527.

Desiraju, G. R. & Steiner, T. (1999). *The Weak Hydrogen Bond in Structural Chemistry and Biology*. Oxford, UK: Oxford University Press.

Dunitz, J. D. (1995). *X-ray Analysis and the Structure of Organic Molecules*, 2nd ed. VCH.

Dunitz, J. D. & Gavezzotti, A. (2005). *Angew. Chem. Int. Ed.* **44**, 1766-1787.

Frisch, M. J., Trucks, G. W., Schlegel, H. B., Scuseria, G. E., Robb, M. A., Cheeseman, J. R., J. A. Montgomery, J., Vreven, T., Kudin, K. N., Burant, J. C., Millam, J. M., Iyengar, S. S., Tomasi, J., Barone, V., Mennucci, B., Cossi, M., Scalmani, G., Rega, N., Petersson, G. A., Nakatsuji, H., Hada, M., Ehara, M., Toyota, K., Fukuda, R., Hasegawa, J., Ishida, M., Nakajima, T., Honda, Y., Kitao, O., Nakai, H., Klene, M., Li, X., Knox, J. E., Hratchian, H. P., Cross, J. B., Bakken, V., Adamo, C., Jaramillo, J., Gomperts, R., Stratmann, R. E., Yazyev, O., Austin, A. J., Cammi, R., Pomelli, C., Ochterski, J. W., Ayala, P. Y., Morokuma, K., Voth, G. A., Salvador, P., Dannenberg, J. J., Zakrzewski, V. G., Dapprich, S., Daniels, A. D., Strain, M. C., Farkas, O., Malick, D. K., Rabuck, A. D., Raghavachari, K., Foresman, J. B., Ortiz, J. V., Cui, Q., Baboul, A. G., Clifford, S., Cioslowski, J., Stefanov, B. B., Liu, G., Liashenko, A., Piskorz, P., Komaromi, I., Martin, R. L., Fox, D. J., Keith, T., Al-Laham, M. A., Peng, C. Y., Nanayakkara, A., Challacombe, M., Gill, P. M. W., Johnson, B., Chen, W., Wong, M. W., Gonzalez, C. & Pople, J. A. (2004). *Gaussian03.* Version Revision E.01. Wallingford CT.

Gavezzotti, A. (2003). *OPiX: A computer program package for the calculation of intermolecular interactions and crystal energies.* University of Milan, Italy.

Gavezzotti, A. (2005a). *Struct. Chem.* **220**, 499-510.

Gavezzotti, A. (2005b). *Z. Kristallogr.* **220**, 499-510.

Ibberson, R. M. (1996). *J. Appl. Crystallogr.* **29**, 498-500.

Kahn, R., Fourme, R., André, D. & Renaud, M. (1973). *Acta Crystallographica, Section B* **29**, 131-138.

Ladell, J. & Post, B. (1954). *Acta. Cryst.* **7**, 559-564.

Lommerse, J. P. M., Motherwell, W. D. S., Ammon, H. L., D, D. J., Gavezzotti, A., Hofmann, D. W. M., Leusen, F. J. J., Mooji, W. T. M., Price, S. L., Schweizer, B., Schmidt, M. U., Van Eijck, B. P., Verwer, P. & Williams, D. E. (2000). *Acta Crystallographica, Section B* **56**, 697-714.

McGregor, P. A., Allan, D. R., Parsons, S. & Pulham, C. R. (2005). *Acta Crystallographica, Section B* **61**, 449-454.

Merrill, L. & Bassett, W. A. (1974). *Rev. Sci. Instrum.* **45**, 290-294.

Motherwell, W. D. S., Ammon, H. L., Dunitz, J. D., Dzyabchenko, A., Erk, P., Gavezzotti, A., Hofmann, D. W. M., Leusen, F. J. J., Lommerse, J. P. M., Mooji, W. T. M., Price, S. L., Scheraga, H., Schweizer, B., Schmidt, M. U., Van Eijck, B. P., Verwer, P. & Williams, D. E. (2002). *Acta Crystallographica, Section B* **58**, 647-661.

Oswald, I. D. H., Allan, D. R., Motherwell, W. D. S. & Parsons, S. (2005). *Acta Crystallographica, Section B* **61**, 69-79.

Parkin, A., Oswald, I. D. H. & Parsons, S. (2004). *Acta Crystallographica, Section B* **60**, 219-227.

Pravica, M., Shen, Y., Quine, Z., Romano, E. & Hartnett, D. (2007). *J. Phys. Chem. B* **111**, 4103-4108.

Rietveld, H. M. (1969). *J. Appl. Cryst.* **2**, 65-71.

Schomaker, V. & Trueblood, K. N. (1968). *Acta. Cryst.* **B24**, 63-76.

Shimizu, H., Nagata, K. & Sasaki, S. (1988). *J. Chem. Phys.* **89**, 2743-2747.

Stevens, E. D. (1977). *Acta. Cryst.* **B34**, 544-551.

Unlu, K., Rios-Martinez, C. & Wehring, B. W. (1995). *J. Radioanal. Nucl. Chem.* **193**, 145-154.

Utsuro, M. & Sugimoto, M. (1977). *J. Nucl. Sci. Technol.* **14**, 390-392.

Wilding, N. B., Crain, J., Hatton, P. D. & Bushnell-Wye, G. (1993). *Acta Crystallographica, Section B* **49**, 320-328.

Chapter 2
Phase behaviour of piperidine

2.1 Introduction

Cyclohexane has been studied extensively and despite being a relatively simple organic molecular compound it has been shown to exhibit significant phase diversity with crystal structures of five polymorphs being determined (Kahn *et al.*, 1973; Wilding *et al.*, 1991; Wilding *et al.*, 1993; Pravica *et al.*, 2007). The heterocyclic analogues tetrahydropyran, 1,4-dioxane (Buschmann *et al.*, 1986) and 1,3,5-trioxane (Busetti *et al.*, 1969), related to cyclohexane by substitution of one or more CH_2 groups by O, also show interesting phase behaviour under varying temperature conditions. Parkin *et al.* (2004) extended the analogy by studying a series of heterocyclic analogues containing groups capable of hydrogen bonding; piperidine, piperazine and morpholine. The compounds are related to cyclohexane by substitution of one or more CH_2 groups by NH and, in the case of morpholine, NH and O. The crystal structures showed a structural relationship with cyclohexane however their behaviour under conditions of varying temperature is more straightforward. Differential scanning calorimetry (DSC) revealed no thermal events other than melting and freezing for piperazine and morpholine in the temperature range examined.

The DSC trace for piperidine was more complex and revealed that after crystallising at 244 K, a phase transition occurred at 239 K on cooling. It was therefore assumed that the structure reported at 150 K corresponded to the second phase. No transformation back to the first phase was observed upon heating, though there was a clear shoulder on the melting peak. It was also noted that the initial crystal growth of piperidine yielded a different unit cell to the reported structure, but the crystal was of insufficient quality for data collection to be pursued.

With this in mind the phase behaviour of piperidine has been investigated more closely using neutron powder diffraction under conditions of varying temperature and, separately, high pressure.

2.2 Experimental

Piperidine-h_{11} and -d_{11} were obtained from Aldrich and used as received.

2.2.1 Variable Temperature

Variable temperature time-of-flight neutron powder diffraction data were recorded using the HRPD instrument at ISIS. As piperidine is liquid under ambient conditions, piperidine-d_{11} was cold-ground in a liquid nitrogen chilled stainless steel mortar (Ibberson, 1996) before being loaded into a rectangular aluminium sample can fitted with a heater. The sample was then placed in a cryostat held at 100 K. After confirming the sample was in the known phase, the temperature was reduced to 2 K and data collected at this temperature. Data were then collected every 5 K in a rapid scan from 5 K to 250 K; there was no indication of a phase transition in this range. No evidence of a pre-melting transition was found on increasing the temperature further to 255 K.

In order to investigate the possibility of a second phase close to the melting point, the sample was removed from the cryostat and allowed to melt. It was then transferred to a cylindrical vanadium can containing glass wool before being placed in a cryostat held at 245 K. The sample was loaded with glass wool as previous work has shown it to promote the formation of small crystallites. This should have been well above the transition temperature (239 K) reported by Parkin *et al.* (2004), however upon crystallisation the known low temperature phase was obtained.

Quenching a sample of piperidine in liquid nitrogen also resulted in the sample crystallising into the same phase. No evidence for a second phase of piperidine was observed.

2.2.2 High Pressure

Ambient temperature, high pressure neutron powder diffraction data were collected using the time-of-flight technique using the PEARL beamline high pressure facility (HiPr) at ISIS. Piperidine-d_{11} was contained in a null-scattering Ti-Zr alloy capsule gasket (Marshall & Francis, 2002) and loaded into a Paris-Edinburgh cell. The

sample was loaded with powdered silica wool as previous work has shown it to aid formation of a good powder when crystallising liquids *in situ* and a small pellet of lead was included as a pressure marker. The pressure was calculated from the refined lead cell parameter using a Birch-Murnaghan equation of state (Birch, 1947) with $V_o = 30.3128$ Å^3, $B_o = 41.92$ GPa, $B' = 5.72$. These parameters were derived by Fortes (2004) as averages of the values determined in three earlier studies (Kuznetsov *et al.*, 2002; Miller & Schuele, 1969; Waldorf & Alers, 1962).

On increasing the pressure to 0.22 GPa the sample crystallised in the monoclinic phase observed at low temperature. The pressure was increased in small steps to a final pressure of 2.79 GPa. Peak broadening was pronounced by this pressure therefore the sample was decompressed to approximately 0.23 GPa. Over a period of four hours the pressure decreased slightly resulting in the sample melting. Recompressing the sample to 0.30 GPa resulted in the sample recrystallising in the same phase.

2.2.3 Structure Refinement

Rietveld refinements were performed using TOPAS-Academic (Coelho, 2007). During refinement of the high pressure data the piperidine molecules were treated as rigid groups using the Z-matrix formalism in TOPAS. Bond lengths and angles were taken from the previously determined structure (Parkin *et al.*, 2004, CSD refcode ITOBAU) with deuterium distances set to standard neutron distances (N-H 1.009 Å, C-H 1.083 Å). Bond lengths, angles and torsion angles were not refined. All non-hydrogen atoms were refined with a common isotropic displacement parameter, as were all deuterium atoms. A fourth order spherical harmonic preferred orientation correction was included as the sample was crystallised *in situ*. Ni and WC phases were also included in the refinement. The presence of these is due to the anvils of the Paris-Edinburgh cell. Rietveld refinement profiles up to 1.09 GPa are shown in Figure 2.1, with crystal and refinement data given in Table 2.1. Above 1.09 GPa peak broadening was quite pronounced therefore intensity-only fits were performed to obtain the lattice parameters instead of Rietveld refinement.

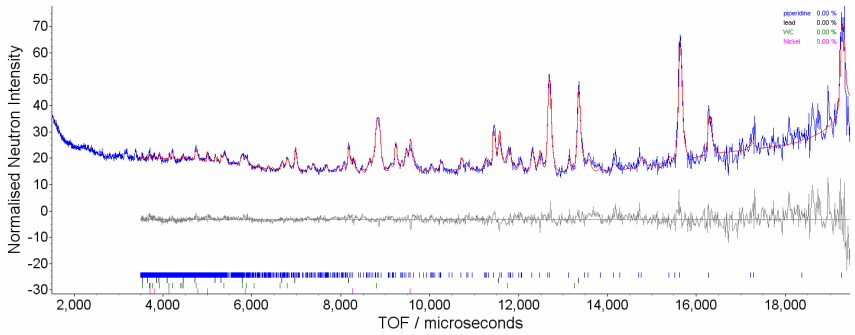

(a) 0.22 GPa

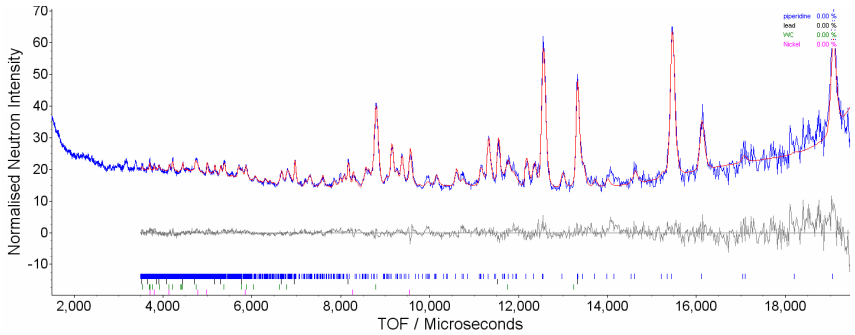

(b) 0.49 GPa

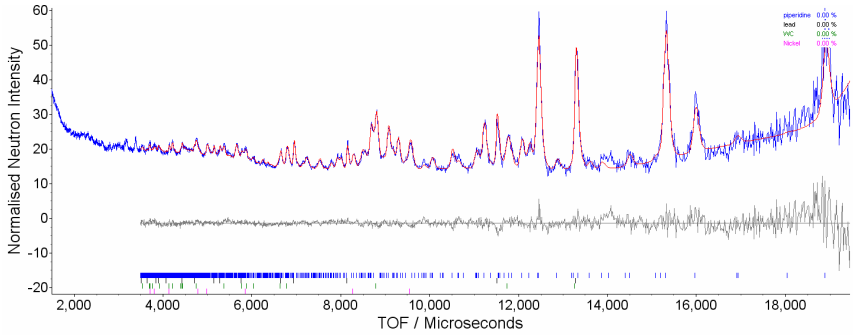

(c) 0.80 GPa

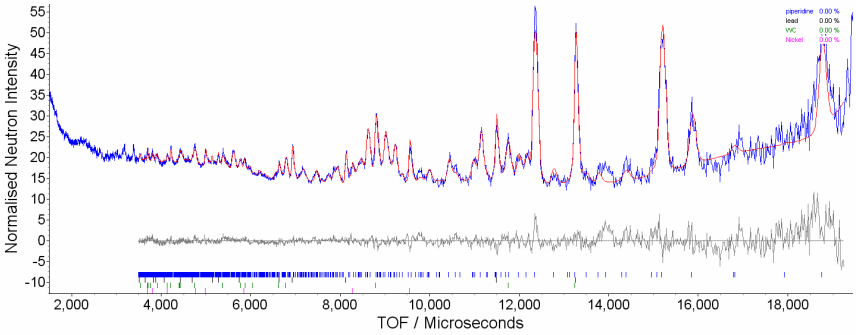

(d) 1.09 GPa

Figure 2.1 Rietveld refinement profiles for the high pressure study of piperidine. Blue and red lines correspond to observed and calculated data respectively. The difference is shown in grey.

Piperidine-d_{11}					
Pressure (GPa)	0.22	0.49	0.80	1.09	Ambient
Temperature (K)	298	298	298	298	2
Crystal Data					
Chemical formula	$C_5D_{11}N$	$C_5D_{11}N$	$C_5D_{11}N$	$C_5D_{11}N$	$C_5D_{11}N$
M_r	96.17	96.17	96.17	96.17	96.17
Cell setting, space group	Monoclinic, $P2_1/c$	Monoclinic, $P2_1/c$	Monoclinic, $P2_1/c$	Monoclinic, $P2_1/c$	Monoclinic, $P2_1/c$
a, b, c (Å)	8.6994(17), 5.2552(9), 11.9045(16)	8.5969(12), 5.2010(7), 11.7936(12)	8.5150(14), 5.1577(8), 11.6988(14)	8.4452(15), 5.1204(9), 11.6181(16)	8.59695(4), 5.21506(2), 11.93271(4)
α, β, γ (°)	90, 96.468(17), 90	90, 96.507(14), 90	90, 96.532(15), 90	90, 96.558(17), 90	90, 96.8790(4), 90
V ($Å^3$)	540.77(16)	523.93(12)	510.45(13)	499.11(14)	531.135(4)
Z	4	4	4	4	4
D_{calc} (g cm^{-3})	1.181	1.219	1.251	1.280	1.203
Radiation type	Neutron	Neutron	Neutron	Neutron	Neutron
Specimen form	Powder	Powder	Powder	Powder	Powder
Data Collection					
Diffractometer	PEARL, ISIS	PEARL, ISIS	PEARL, ISIS	PEARL, ISIS	HRPD, ISIS
Collection method	Time of flight	Time of flight	Time of flight	Time of flight	Time of flight
Range of *d* (Å)	0.75 – 4.17	0.75 – 4.17	0.75 – 4.17	0.75 – 4.12	0.83 – 2.51
Refinement					
Method	Rietveld	Rietveld	Rietveld	Rietveld	Rietveld
R_p	5.329	4.484	4.370	4.363	4.626
R_{wp}	4.226	3.485	3.265	3.396	5.589
S	1.294	1.432	1.344	1.395	1.544
Background	9 term Chebychev polynomial	9 term Chebychev polynomial	9 term Chebychev polynomial	9 term Chebychev polynomial	6 term Chebychev polynomial
Profile function	Back-to-back exponential convoluted with Voigt function	Back-to-back exponential convoluted with Voigt function	Back-to-back exponential convoluted with Voigt function	Back-to-back exponential convoluted with Voigt function	Back-to-back exponential
Number of parameters	42	42	42	42	74
Weighting scheme	$1/\sigma^2$	$1/\sigma^2$	$1/\sigma^2$	$1/\sigma^2$	$1/\sigma^2$

Table 2.1 Crystal and refinement data for piperidine.

During refinement of the data collected at 2 K the piperidine molecules were treated using the Z-matrix formalism in TOPAS. Bond lengths and angles were refined, though all C-D distances were constrained to be equal. Anisotropic displacement parameters were modelled using the TLS formalism. A fourth order spherical harmonic preferred orientation was also included. The Rietveld refinement profile is shown in Figure 2.2 with crystal and refinement data given in Table 2.1. Intensity-only fits were performed on the rapid scan data to obtain the lattice parameters.

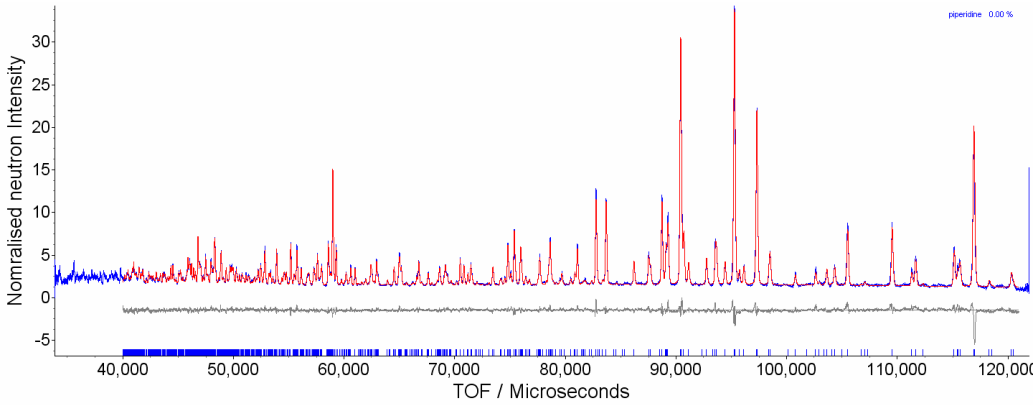

Figure 2.2 Rietveld refinement profile for piperidine at 2 K. Blue and red lines correspond to observed and calculated data respectively. The difference is shown in grey.

2.2.4 Differential Scanning Calorimetry

Differential scanning calorimetry (DSC) traces were recorded on piperidine-h_{11} and piperidine-d_{11} using a Perkin Elmer Pyris 1 DSC instrument with the samples contained in closed aluminium pans. Samples were loaded at room temperature and initially cooled to 100 K and then heated to 293 K at a rate of 10 K/min. A second trace was recorded for each compound under the same experimental conditions using the same sample used for the first trace.

2.2.4 Other programs used

Strain tensors were calculated using the program STRAIN and visualised using DIAMOND. Vinet equation-of-state calculations were performed using EOSfit. All fitting of the unit cell parameters was performed using Origin.

2.3 Results

The crystal structure of piperidine has been reported by Parkin *et al.* (2004) at 150 K. Variable temperature neutron powder diffraction revealed the structure exists between 2 K and 255 K.

Crystallisation *via* the application of pressure resulted in the same crystal structure as obtained at low temperature. No phase transitions were evident upon compression to 2.79 GPa.

2.3.1 The crystal structure of piperidine

Piperidine crystallises in the monoclinic space group $P2_1/c$ with one molecule in the asymmetric unit occupying a general position. The molecule adopts a chair conformation with the hydrogen atom attached to nitrogen in an equatorial position. Primary bond distances and angles are unremarkable.

The most significant intermolecular interaction is an N-H…N hydrogen bond (2.141(3) Å at 2 K) which links the molecules to form chains parallel to the *b* axis, Figure 2.3. Successive molecules along the chains are related by the 2_1 screw axis. These chains are related to neighbouring chains by the *c* glide plane and the result is interleaving of the chains.

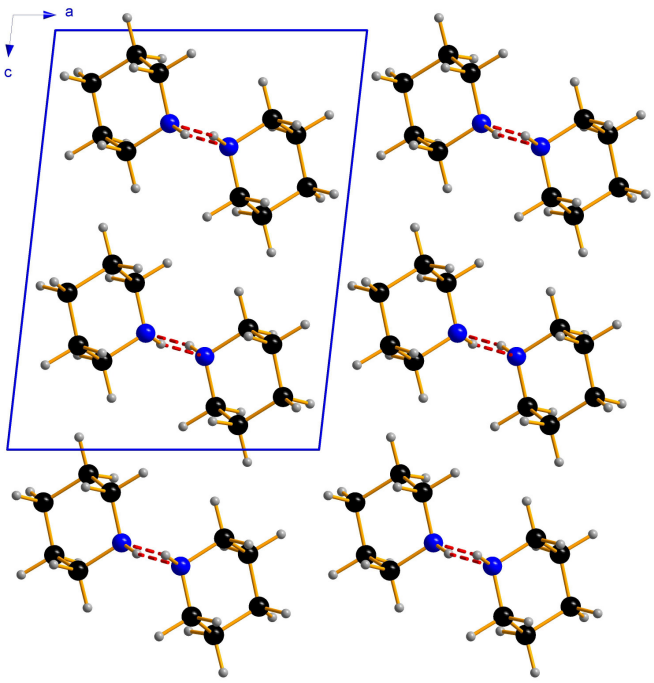

(a) Packing of hydrogen bonded chains

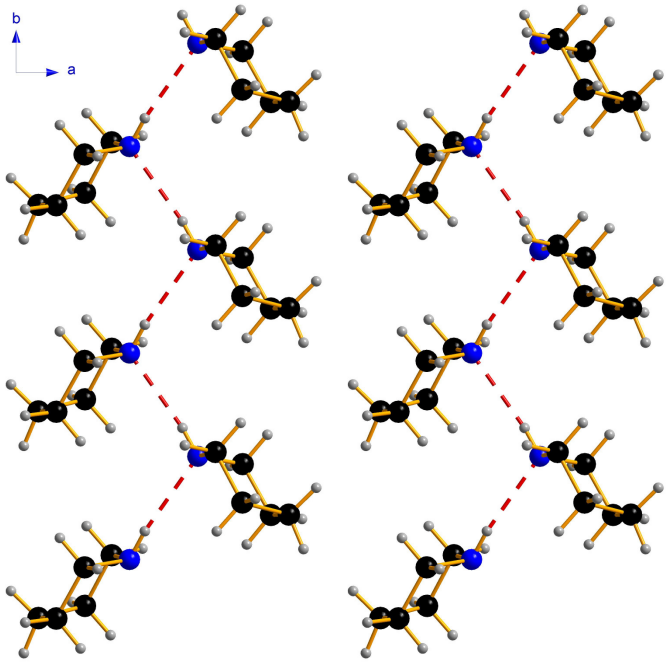

(b) Interleaving of hydrogen bonded chains

Figure 2.3 Hydrogen bonded chains in piperidine.

2.3.2 The effect of temperature on the structure of piperidine

The low temperature behaviour of piperidine was surveyed *via* a rapid scan from 5 K to 255 K with data collected every 5 K. The extracted lattice parameters are given in Table 2.2 and displayed in Figure 2.4. The data exhibit a smooth expansion of the unit cell with no evidence of a phase transition. The structure previously determined by Parkin *et al.* (2004) at 150 K was found to exist over the entire temperature range studied.

The increase in unit cell volume between 2 K and 255 K is 31.16 $Å^3$ which represents 5.9% of the volume at 2 K. The largest expansion is in the *a* lattice parameter, 2.6% of the value at 2 K, and the smallest expansion in the *c* lattice parameter (1.1% of the 2 K value). The beta angle decreases with increasing temperature, decreasing by 0.35% of the value at 2 K.

The unit cell parameters were initially fitted to an Einstein expression of the form $X = X_o + K/(e^{\theta/T} - 1)$ where X_o is the parameter X at 0 K, K is the Einstein constant, T is the temperature in Kelvin between 2 & 255 and θ is the effective Einstein temperature. However the fits did not adequately model the variation as a function of temperature, ad in particular the low temperature behaviour as illustrated for the unit cell volume in Figure 2.5.

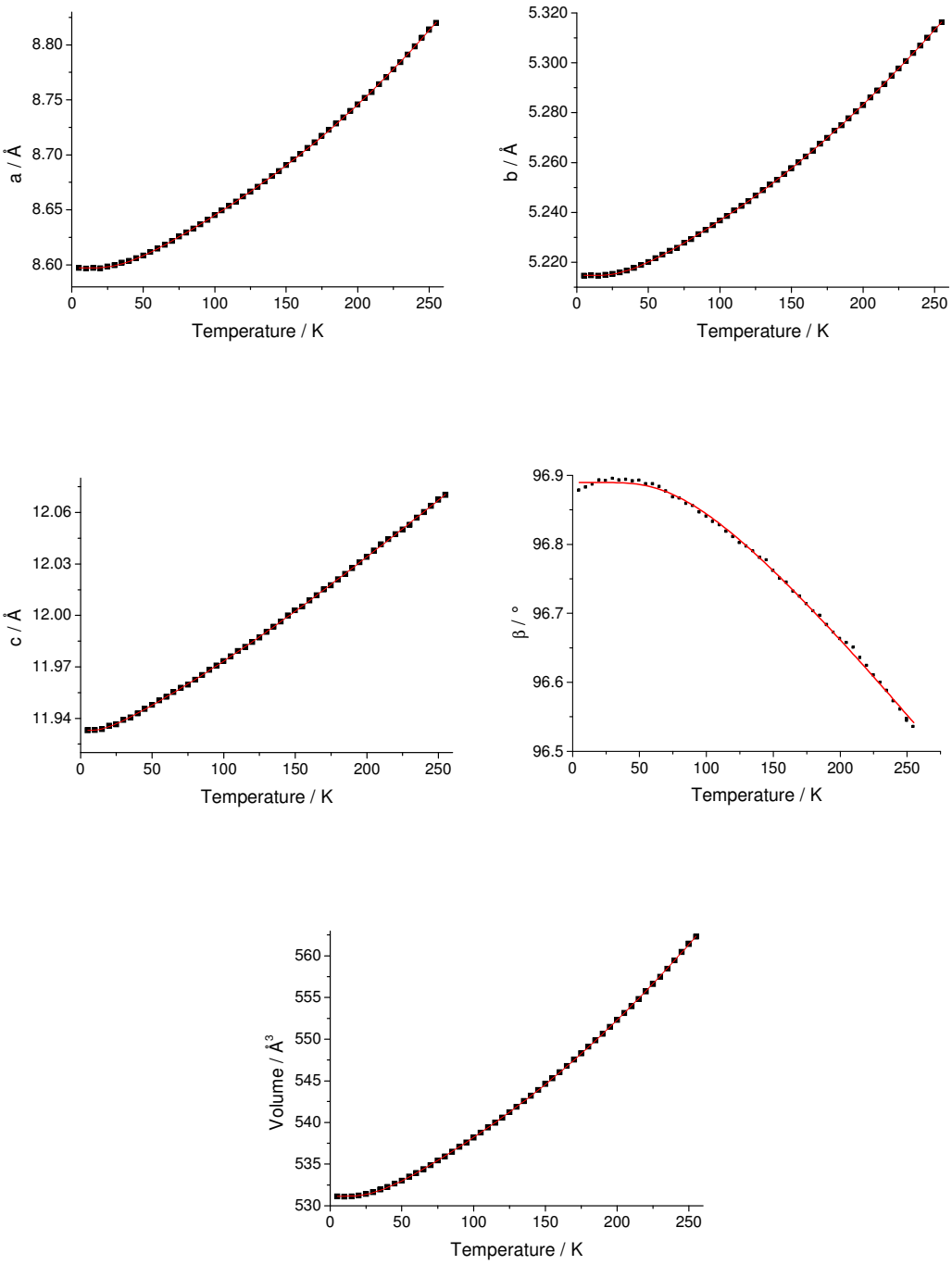

Figure 2.4 Variation of the lattice parameters and volume of piperidine as a function of temperature. The calculated fits are represented by double-Einstein functions, except for β which is represented by a single Einstein function.

Temperature / K	*a* / Å	*b* / Å	*c* / Å	β / Å	Volume / Å^3
2	8.59695(4)	5.21506(2)	11.93271(4)	96.8790(4)	531.135(4)
5	8.59703(13)	5.21457(5)	11.93308(15)	96.8779(9)	531.108(12)
10	8.59652(14)	5.21462(5)	11.93312(15)	96.8822(9)	531.078(12)
15	8.59719(14)	5.21455(5)	11.93369(15)	96.8865(9)	531.133(12)
20	8.59692(14)	5.21495(5)	11.93568(15)	96.8928(10)	531.239(12)
25	8.59843(14)	5.21525(5)	11.93648(16)	96.8921(10)	531.399(12)
30	8.59951(14)	5.21593(5)	11.93905(15)	96.8951(9)	531.646(12)
35	8.60191(14)	5.21665(5)	11.94060(16)	96.8929(10)	531.940(12)
40	8.60352(14)	5.21771(5)	11.94282(15)	96.8935(10)	532.246(12)
45	8.60595(15)	5.21884(5)	11.94551(16)	96.8913(10)	532.634(12)
50	8.60847(15)	5.22007(5)	11.94790(16)	96.8926(10)	533.020(12)
55	8.61166(15)	5.22160(5)	11.95043(15)	96.8870(10)	533.494(12)
60	8.61463(14)	5.22301(5)	11.95253(14)	96.8870(10)	533.915(12)
65	8.61798(14)	5.22450(5)	11.95517(14)	96.8833(10)	534.397(12)
70	8.62161(14)	5.22578(5)	11.95782(13)	96.8768(10)	534.879(12)
75	8.62564(14)	5.22773(5)	11.95952(13)	96.8682(10)	535.415(12)
80	8.62928(14)	5.22921(5)	11.96249(12)	96.8662(10)	535.928(11)
85	8.63290(14)	5.23117(5)	11.96526(13)	96.8588(10)	536.486(12)
90	8.63689(13)	5.23288(5)	11.96831(12)	96.8555(10)	537.050(11)
95	8.64081(14)	5.23474(5)	11.97077(12)	96.8463(10)	537.606(11)
100	8.64514(12)	5.23669(4)	11.97339(11)	96.8403(10)	538.200(10)
105	8.64943(11)	5.23851(4)	11.97618(10)	96.8327(9)	538.788(10)
110	8.65336(11)	5.24067(4)	11.97923(10)	96.8277(9)	539.399(9)
115	8.65756(10)	5.24244(4)	11.98167(10)	96.8183(9)	539.963(9)
120	8.66207(11)	5.24444(4)	11.98449(10)	96.8106(9)	540.586(9)
125	8.66645(11)	5.24674(4)	11.98710(10)	96.8018(9)	541.225(9)
130	8.67104(11)	5.24884(4)	11.99029(10)	96.7968(9)	541.878(9)
135	8.67578(11)	5.25111(4)	11.99339(10)	96.7897(9)	542.556(9)
140	8.68072(10)	5.25303(4)	11.99639(10)	96.7804(9)	543.210(9)
145	8.68517(11)	5.25541(4)	11.99991(11)	96.7768(9)	543.899(9)
150	8.69052(10)	5.25767(4)	12.00287(10)	96.7618(8)	544.619(9)
155	8.69578(11)	5.26003(4)	12.00522(11)	96.7506(8)	545.313(10)
160	8.70075(11)	5.26238(4)	12.00882(11)	96.7444(9)	546.038(9)
165	8.70615(11)	5.26483(4)	12.01173(11)	96.7316(9)	546.779(10)
170	8.71154(10)	5.26747(4)	12.01520(12)	96.7243(9)	547.559(9)
175	8.71731(10)	5.26983(4)	12.01758(14)	96.7134(9)	548.287(10)
180	8.72277(10)	5.27274(4)	12.02106(15)	96.7030(9)	549.104(10)
185	8.72844(10)	5.27496(4)	12.02405(15)	96.6966(9)	549.837(10)
190	8.73391(9)	5.27773(4)	12.02755(17)	96.6830(9)	550.646(11)
195	8.74000(10)	5.28040(4)	12.03096(16)	96.6722(9)	551.477(11)
200	8.74598(9)	5.28304(4)	12.03411(16)	96.6629(9)	552.285(10)
205	8.75172(10)	5.28610(4)	12.03777(16)	96.6571(9)	553.142(10)
210	8.75712(10)	5.28888(5)	12.04141(17)	96.6500(9)	553.950(11)
215	8.76418(10)	5.29150(5)	12.04442(19)	96.6353(9)	554.827(12)
220	8.77059(10)	5.29479(5)	12.0473(2)	96.6240(9)	555.725(12)
225	8.77769(11)	5.29766(4)	12.0501(2)	96.6100(10)	556.620(13)
230	8.78434(11)	5.30071(5)	12.0528(2)	96.5993(10)	557.502(13)
235	8.79102(11)	5.30389(5)	12.0560(2)	96.5876(11)	558.461(14)
240	8.79865(11)	5.30688(5)	12.0602(2)	96.5723(12)	559.433(15)
245	8.80653(11)	5.31010(5)	12.0638(2)	96.5605(12)	560.456(15)
250	8.81407(9)	5.31328(4)	12.0676(2)	96.5442(9)	561.464(11)
255	8.82002(11)	5.31626(5)	12.0702(2)	96.5355(11)	562.290(14)

Table 2.2 Lattice parameters of piperidine from 2 to 255 K.

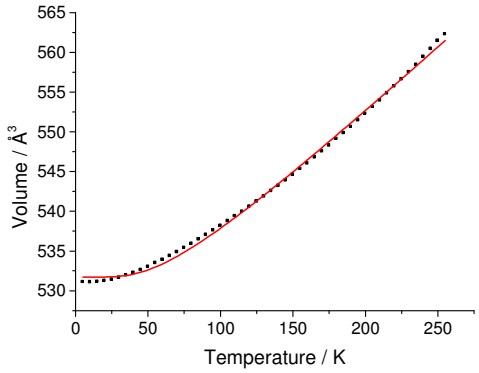

Figure 2.5 Variation of the unit cell volume as a function of temperature modelled using a single Einstein function.

The unit cell parameters are well fitted to a double-Einstein expression of the form $X = X_o + K_1/(e^{\theta_1/T} - 1) + K_2/(e^{\theta_2/T} - 1)$ where X_o is the parameter X at 0 K, K_1 & K_2 are the Einstein constants, T is the temperature in Kelvin between 2 & 255 and θ_1 & θ_2 are the effective Einstein temperatures. The angle β is modelled equally well using single Einstein and double Einstein functions therefore a single Einstein function was chosen. The results of the fits are displayed graphically in Figure 2.4 and tabulated in Table 2.3.

	X_o	K_1	θ_1 / K	K_2	θ_2 / K	Adjusted R^2
a	8.59716(16) Å	1.49(15)	928(31)	0.107(3)	118(2)	0.99996
b	5.214706(6) Å	0.38(2)	770(18)	0.0456(10)	113(2)	0.99998
c	11.9330(2) Å	0.095(8)	458(36)	0.026(2)	51(3)	0.99994
β	96.8895(12) °	-0.69(3)	278(6)	-	-	0.99803
Volume	531.15(2) Å^3	123(7)	788(20)	12.5(3)	102(2)	0.99998

Table 2.3 Results from the double-Einstein function data-fitting. The parameter β was fitted to a single Einstein function.

The Einstein model assumes a single frequency for all oscillations. The need for the inclusion of a second Einstein expression in order to fit the temperature variation of the unit cell parameters indicates that this assumption is not valid in piperidine and suggests that both intra- and inter-molecular modes are activated.

The instantaneous thermal expansion is related to the unit cell parameter X (Schofield *et al.*, 1996), where $\alpha_X = (1/X_o)(\delta X/\delta T)$. The resultant general expression is given in Equation 2.1 and the expressions for the cell parameters are given in Equations 2.2 – 2.6.

$$\alpha_X = \left(\frac{1}{X_o}\right)\left(\frac{\delta X}{\delta T}\right) = \frac{K_1\theta_1}{X_o}\cdot\left[\frac{e^{\theta_1/T}}{(e^{\theta_1/T}-1)^2T^2}\right] + \frac{K_2\theta_2}{X_o}\cdot\left[\frac{e^{\theta_2/T}}{(e^{\theta_2/T}-1)^2T^2}\right] \quad (2.1)$$

$$\alpha_a = \left(\frac{1}{a_o}\right)\left(\frac{\delta a}{\delta T}\right) = \frac{K_1\theta_1}{a_o}\cdot\left[\frac{e^{\theta_1/T}}{(e^{\theta_1/T}-1)^2T^2}\right] + \frac{K_2\theta_2}{a_o}\cdot\left[\frac{e^{\theta_2/T}}{(e^{\theta_2/T}-1)^2T^2}\right] \quad (2.2)$$

$$= 160.834\cdot\left[\frac{e^{\theta_1/T}}{(e^{\theta_1/T}-1)^2T^2}\right] + 1.469\cdot\left[\frac{e^{\theta_2/T}}{(e^{\theta_2/T}-1)^2T^2}\right]$$

$$\alpha_b = \left(\frac{1}{b_o}\right)\left(\frac{\delta b}{\delta T}\right) = \frac{K_1\theta_1}{b_o}\cdot\left[\frac{e^{\theta_1/T}}{(e^{\theta_1/T}-1)^2T^2}\right] + \frac{K_2\theta_2}{b_o}\cdot\left[\frac{e^{\theta_2/T}}{(e^{\theta_2/T}-1)^2T^2}\right] \quad (2.3)$$

$$= 56.110\cdot\left[\frac{e^{\theta_1/T}}{(e^{\theta_1/T}-1)^2T^2}\right] + 0.988\cdot\left[\frac{e^{\theta_2/T}}{(e^{\theta_2/T}-1)^2T^2}\right]$$

$$\alpha_c = \left(\frac{1}{c_o}\right)\left(\frac{\delta c}{\delta T}\right) = \frac{K_1\theta_1}{c_o}\cdot\left[\frac{e^{\theta_1/T}}{(e^{\theta_1/T}-1)^2T^2}\right] + \frac{K_2\theta_2}{c_o}\cdot\left[\frac{e^{\theta_2/T}}{(e^{\theta_2/T}-1)^2T^2}\right] \quad (2.4)$$

$$= 3.646\cdot\left[\frac{e^{\theta_1/T}}{(e^{\theta_1/T}-1)^2T^2}\right] + 0.111\cdot\left[\frac{e^{\theta_2/T}}{(e^{\theta_2/T}-1)^2T^2}\right]$$

$$\alpha_\beta = \left(\frac{1}{\beta_o}\right)\left(\frac{\delta\beta}{\delta T}\right) = \frac{K_1\theta_1}{\beta_o}\cdot\left[\frac{e^{\theta_1/T}}{(e^{\theta_1/T}-1)^2T^2}\right] \qquad (2.5)$$

$$= -1.980\cdot\left[\frac{e^{\theta_1/T}}{(e^{\theta_1/T}-1)^2T^2}\right]$$

$$\alpha_V = \left(\frac{1}{V_o}\right)\left(\frac{\delta V}{\delta T}\right) = \frac{K_1\theta_1}{V_o}\cdot\left[\frac{e^{\theta_1/T}}{(e^{\theta_1/T}-1)^2T^2}\right] + \frac{K_2\theta_2}{V_o}\cdot\left[\frac{e^{\theta_2/T}}{(e^{\theta_2/T}-1)^2T^2}\right] \qquad (2.6)$$

$$= 182.479\cdot\left[\frac{e^{\theta_1/T}}{(e^{\theta_1/T}-1)^2T^2}\right] + 2.400\cdot\left[\frac{e^{\theta_2/T}}{(e^{\theta_2/T}-1)^2T^2}\right]$$

In mineralogical studies, a Taylor expansion is used to simplify the expression for the thermal expansion. At high temperatures $e^{\theta/T} \approx 1+(\theta/T)$ and consequently, $(1/X_o)(\delta X/\delta T) \approx K_1/(X_o\theta_1)\cdot[1+(\theta_1/T)] + K_2/(X_o\theta_2)\cdot[1+(\theta_2/T)]$. Piperidine is at low temperatures therefore this high temperature simplification is not valid, however, the resultant expressions for the cell parameters are given in Equations 2.7 – 2.11 for comparison.

$$\alpha_a = \left(\frac{1}{a_o}\right)\left(\frac{\delta a}{\delta T}\right) \approx \frac{K_1}{(a_o\theta_1)}\cdot\left[1+\left(\frac{\theta_1}{T}\right)\right] + \frac{K_2}{(a_o\theta_2)}\cdot\left[1+\left(\frac{\theta_2}{T}\right)\right] \qquad (2.7)$$

$$= 1.87\times10^{-4}\left[1+\left(\frac{\theta_1}{T}\right)\right] + 1.05\times10^{-4}\left[1+\left(\frac{\theta_2}{T}\right)\right]$$

$$\alpha_b = \left(\frac{1}{b_o}\right)\left(\frac{\delta b}{\delta T}\right) \approx \frac{K_1}{(b_o\theta_1)}\cdot\left[1+\left(\frac{\theta_1}{T}\right)\right] + \frac{K_2}{(b_o\theta_2)}\cdot\left[1+\left(\frac{\theta_2}{T}\right)\right] \qquad (2.8)$$

$$= 9.46\times10^{-5}\left[1+\left(\frac{\theta_1}{T}\right)\right] + 7.74\times10^{-5}\left[1+\left(\frac{\theta_2}{T}\right)\right]$$

$$\alpha_c = \left(\frac{1}{c_o}\right)\left(\frac{\delta c}{\delta T}\right) \approx \frac{K_1}{(c_o\theta_1)} \cdot \left[1+\left(\frac{\theta_1}{T}\right)\right] + \frac{K_2}{(c_o\theta_2)} \cdot \left[1+\left(\frac{\theta_2}{T}\right)\right] \qquad (2.9)$$

$$= 4.27\times10^{-5}\left[1+\left(\frac{\theta_1}{T}\right)\right] + 1.74\times10^{-5}\left[1+\left(\frac{\theta_2}{T}\right)\right]$$

$$\alpha_\beta = \left(\frac{1}{\beta_o}\right)\left(\frac{\delta \beta}{\delta T}\right) \approx \frac{K_1}{(\beta_o\theta_1)} \cdot \left[1+\left(\frac{\theta_1}{T}\right)\right] \qquad (2.10)$$

$$= -2.56\times10^{-5}\left[1+\left(\frac{\theta_1}{T}\right)\right]$$

$$\alpha_V = \left(\frac{1}{V_o}\right)\left(\frac{\delta V}{\delta T}\right) \approx \frac{K_1}{(V_o\theta_1)} \cdot \left[1+\left(\frac{\theta_1}{T}\right)\right] + \frac{K_2}{(V_o\theta_2)} \cdot \left[1+\left(\frac{\theta_2}{T}\right)\right] \qquad (2.11)$$

$$= 2.94\times10^{-4}\left[1+\left(\frac{\theta_1}{T}\right)\right] + 2.31\times10^{-4}\left[1+\left(\frac{\theta_2}{T}\right)\right]$$

The thermal expansion coefficients exhibit the trend $\alpha_a > \alpha_b > \alpha_c$. The principal axes of the strain tensor, shown in Figure 2.6, exhibit the same trend. The largest component, in red, lies predominantly along the *a* axis corresponding to the zig-zag hydrogen bonded chains becoming narrower and a reduction in the distance between the interleaved chains. The smallest component, shown in green, is mainly along the *c* axis which undergoes the smallest change upon varying the temperature.

Further crystallisations revealed no evidence of another phase close to the melting point. Crystallising the sample at 245 K, above the transition temperature reported by Parkin *et al.* (2004), and quenching in liquid nitrogen both produced the same phase as before.

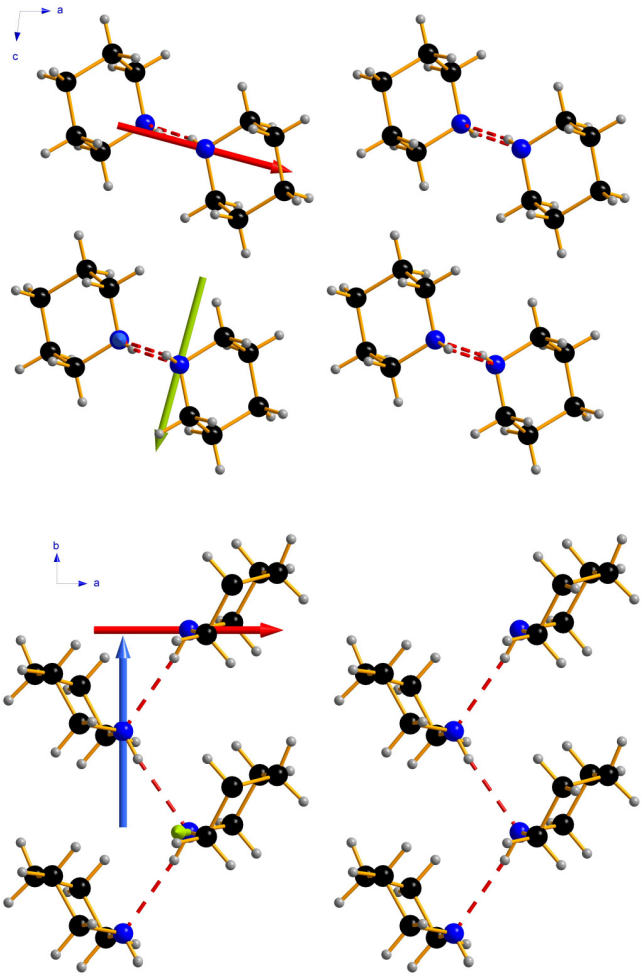

Figure 2.6 Principal axes of the strain tensor. Red (0.116, 0.000, 0.022), blue (0.000, 0.192, 0.000) and green (-0.017, 0.000, 0.082).

2.3.3 The effect of pressure on the structure of piperidine

The liquid piperidine sample loaded into the Paris-Edinburgh cell crystallised when the pressure was increased to 0.22 GPa. The crystal structure obtained corresponds to the structure previously reported by Parkin *et al.* (2004) at 150 K.

Upon increasing the pressure on piperidine a smooth reduction in unit cell volume was observed, Figure 2.7, reducing by 15.5 % of the value at 0.22 GPa by 2.79 GPa. The *a*-axis undergoes the greatest reduction in length (6.2 %) between 0.22 GPa and 2.79 GPa. The *c* axis is the least sensitive to pressure, reducing by 4.5 %. This trend is the same as observed under conditions of varying temperature.

The principal axes of the strain tensor are shown in Figure 2.8. The largest component, shown in red, corresponds to the zig-zag hydrogen bonded chains becoming narrower as the pressure increases and a reduction in the distance between the interleaved chains. The second largest component, shown in blue, lies along the hydrogen bonded chains, parallel to the *b* axis. The result is a shortening of the hydrogen bonds from 3.170(12) Å (N…N) at 0.22 GPa to 3.076(7) Å at 1.09 GPa. The smallest component, shown in green, corresponds to closing up of the voids between the hydrogen bonded chains, Figure 2.9.

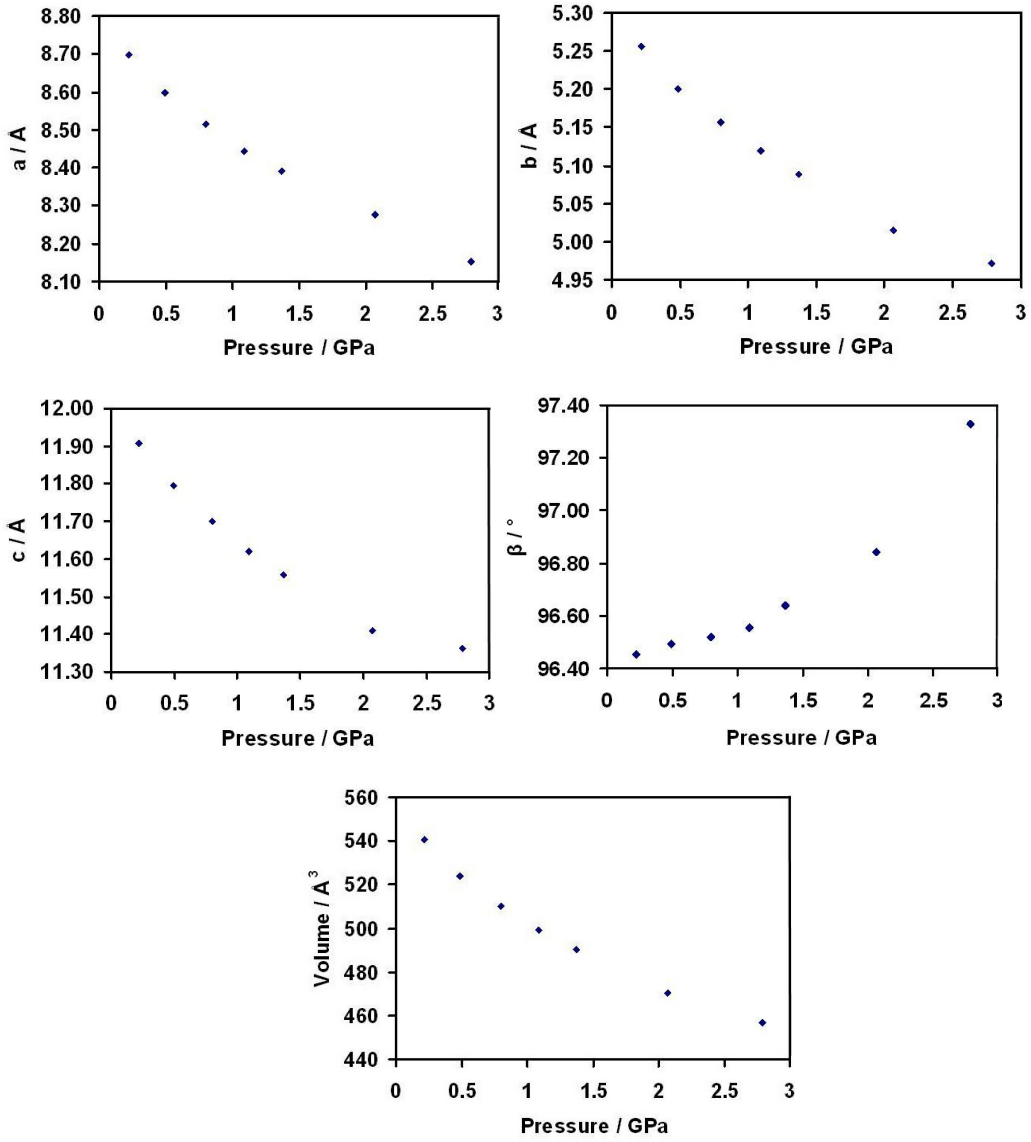

Figure 2.7 Variation of the lattice parameters and volume of piperidine as a function of pressure.

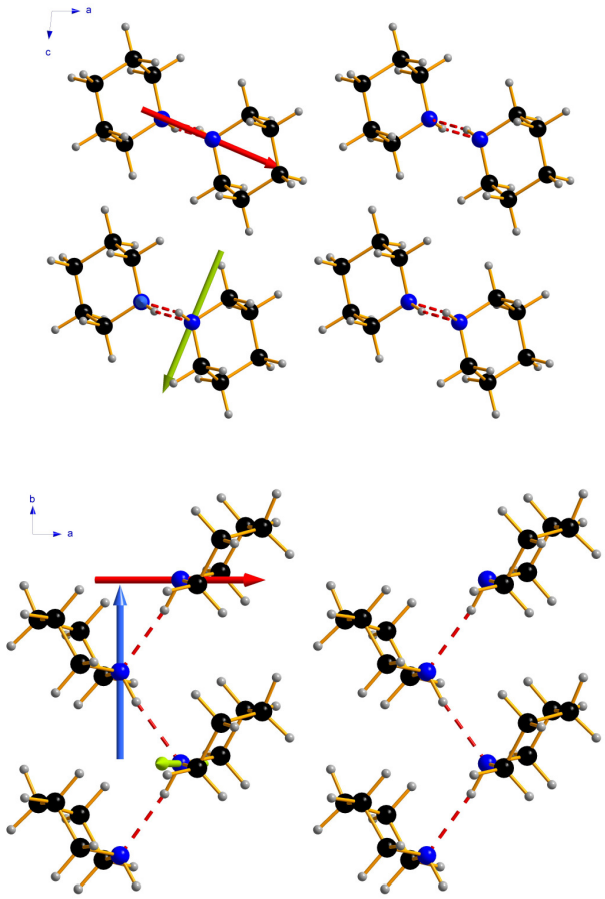

Figure 2.8 Principal axes of the strain tensor. Red (0.111, 0.000, 0.033), blue (0.000, 0.019, 0.000) and green (-0.032, 0.000, 0.078).

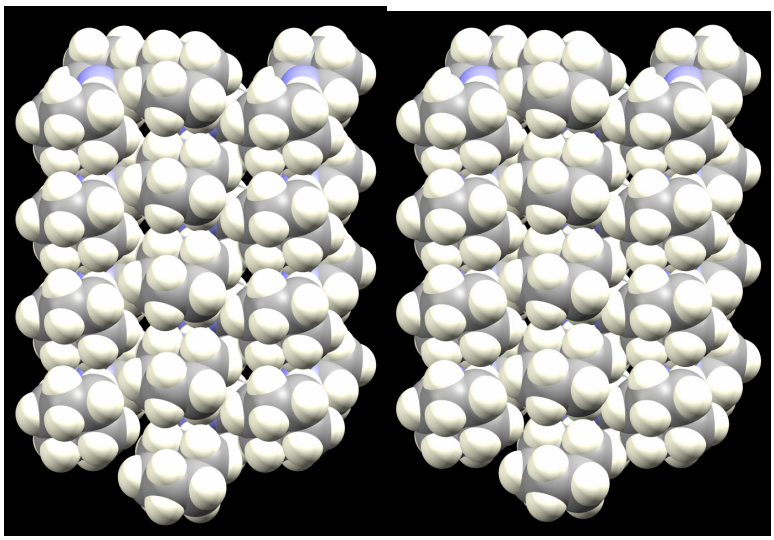

(a) 0.22 GPa (b) 1.09 GPa

Figure 2.9 Voids between hydrogen bonded chains.

The bulk modulus (K_0) refined for a Vinet equation of state (Vinet *et al.*, 1986; Vinet *et al.*, 1987) is 6.3(4) GPa, though the data-set used to calculate this quantity is admittedly rather limited. The values of V_0 and K' refined to 557(1) Å^3 and 8.3(5) respectively, with $R_w = 0.83\%$. Molecular solids typically have $K_0 < 30$ GPa (Angel, 2004) and the following K_0 values are useful for comparison: $Ru_3(CO)_{12}$ 6.6 GPa, salicylaldoxime 13.3 GPa, NaCl 25 GPa, quartz 37 GPa, ceramics 50-300 GPa and diamond 440 GPa (Wood *et al.*, 2006; Slebodnick *et al.*, 2004).

There was no evidence of a phase transition up to 2.79 GPa. After decompressing the sample to 0.23 GPa the pressure slowly decreased further over a period of four hours as has been observed in previous experiments. This resulted in the sample melting directly from this phase. Recompressing to 0.30 GPa recrystallised the sample in the original phase, thus there is no evidence of a second phase of piperidine close to the melting point; the known phase transforms directly to the melt.

2.3.4 Differential scanning calorimetry

Differential scanning calorimetry (DSC) traces were recorded for both piperidine-h_{11} and piperidine-d_{11}. The traces of the two compounds exhibited the same features and are shown in Figure 2.10. On cooling a sharp transition was observed due to the sample crystallising (piperidine-h_{11} at 231 K and piperidine-d_{11} at 241 K). In both cases the crystallisation temperatures are lower than the usual freezing point of the samples; such supercooling often occurs in DSC experiments. The only feature of the heating cycle was the sample melting which appears as a double peak in both compounds. This is likely due to inhomogeneities in the sample pan and has been observed in other compounds which crystallised in the sample pan.

Parkin *et al.* (2004) observed piperidine-h_{11} crystallising at 244 K followed by a phase transition at 239 K upon cooling; however there was no evidence of this transition in the trace recorded here. There were no additional features in the heating cycle of the trace reported by Parkin *et al.* (2004).

As a result of this discrepancy upon cooling a second trace was recorded for both piperidine-h_{11} and piperidine-d_{11} using the same samples as before. The resultant traces were significantly different to the original ones, as shown in Figure 2.10, with several additional thermal events observed. The traces for piperidine-h_{11} and piperidine-d_{11} are different.

Upon cooling piperidine-h_{11} a small exothermic event occurred at 231 K followed immediately by a sharp transition at 229 K. On cooling further a small trough is observed at 211 K. No further events are observed on cooling to 100 K. During the heating cycle there is a small endothermic event at 211 K, thus the transition observed at 211 K upon cooling appears to be reversible. The only other event upon heating is the melting transition which appears as a series of peaks beginning at 251 K.

During the second DSC experiment, piperidine-d_{11} initially crystallised at 260 K followed by a sharp transition at 251 K. Further cooling produces further exothermic events at 245 and 241 K. No further transitions are observed upon cooling to 95 K. On heating the sample the only transition corresponds to the sample melting. As for piperidine-h_{11}, this appears as a series of peaks with the onset of melting at 256 K.

This indicates that the behaviour of piperidine depends on the thermal history of the sample. Parkin *et al.* (2004) noted that the formation of the first phase was not always observed and appeared to depend on the experimental conditions however the two DSC traces recorded for each compound here were performed under the same experimental conditions. Although the second traces recorded for piperidine-h_{11} and piperidine-d_{11} are similar but not identical, both compounds exhibit significantly different behaviour to the initial DSC experiments.

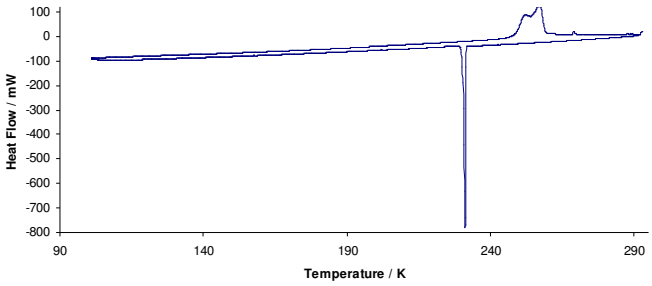

(a) Piperidine-h_{11} first trace

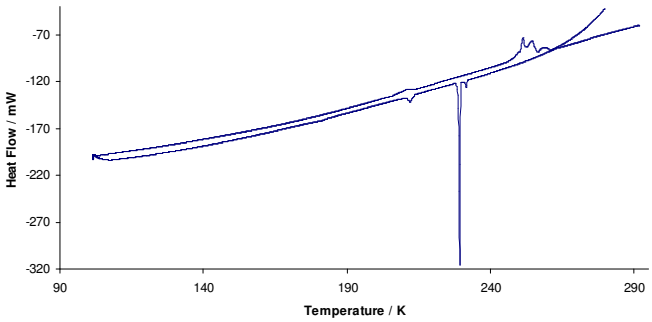

(b) Piperidine-h_{11} second trace

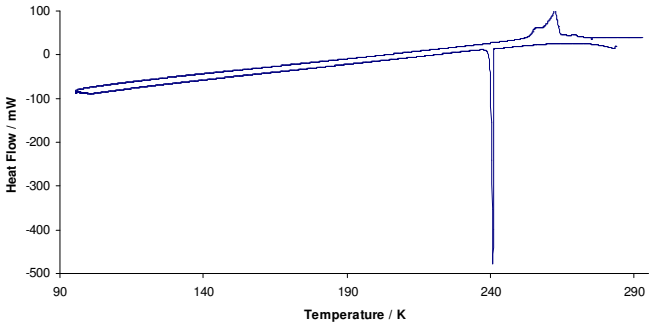

(c) Piperidine-d_{11} first trace

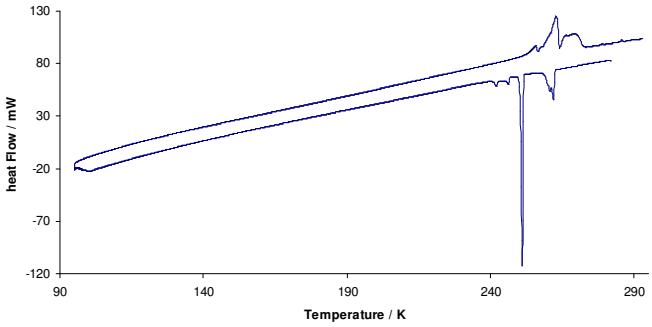

(d) Piperidine-d_{11} second trace

Figure 2.10 DSC traces for piperidine-h_{11} and piperidine-d_{11}.

2.4 Discussion

2.4.1 Comparison of the effect of temperature and pressure

Neutron powder diffraction studies have shown that crystallisation of piperidine at low temperature or *via* the application of pressure results in the formation of the same crystal structure with no evidence of a phase transition in either study. Comparing the response of the unit cell volume to pressure and to temperature, Table 2.4, we see that although the pressure range studied was limited, the reduction in unit cell volume achieved by increasing the pressure to 2.79 GPa was significantly greater than observed upon cooling piperidine to 2 K.

Temperature		**Pressure**	
255 K	562.29 Å^3	0.22 GPa	540.77 Å^3
2 K	531.13 Å^3	2.79 GPa	456.70 Å^3
% Reduction	5.5	% Reduction	15.5

Table 2.4 Comparison of unit cell volume.

The unit cell parameters exhibit an anisotropic response to changes in temperature or pressure. As discussed earlier, reducing the temperature or increasing the pressure has the largest effect on the *a* axis which corresponds to the interleaved hydrogen bonded chains becoming narrower and closer together, while the *c* axis is the least sensitive and indeed at 1.09 GPa there are still voids between the chains (Figure 2.9).

The similarity of the effect of temperature and pressure on the structure is evident when comparing the strain tensors, Figure 2.11. The largest components have very similar orientations, lying approximately along the direction of the N-H...N hydrogen bonds. There is a larger difference between the orientations of the smallest components which lie predominantly along the *c* axis, however this corresponds to the direction which is least sensitive to changes in temperature or pressure. Compression in this direction would affect the N-H…N hydrogen bonding angle. In both cases, the third component of the strain tensor lies parallel to the *b* axis and

therefore the hydrogen bonded chains. Compression in this direction allows the chains to compress in a manner similar to a spring. This affects the hydrogen bond distance but not the angle.

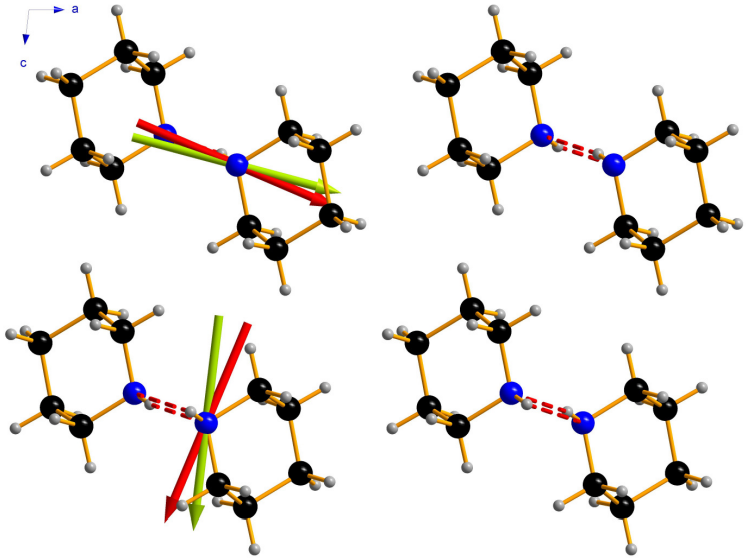

Figure 2.11 Comparison of principal axes of strain tensor for temperature (green) and pressure (red).

Comparison of the N-H…N hydrogen bond distances and angles, Table 2.5, shows that even the rather modest pressure of 1.09 GPa results in the hydrogen bond shortening significantly more than is observed upon cooling to 2 K.

	0.22 GPa	0.49 GPa	0.80 GPa	1.09 GPa	2 K
N1H1…N1[i]					
N1…N1 / Å	3.170(12)	3.126(8)	3.117(7)	3.076(7)	3.1536(18)
H1…N1 / Å	2.175(13)	2.132(8)	2.123(7)	2.085(7)	2.141(3)
∠N1H1N1 / °	168.28	167.78	167.81	166.80	170.67
∠N1N1N1 / °	111.9(6)	112.6(4)	111.7(3)	112.7(4)	111.55(9)

(i) $1 - x, ½ + y, ½ - z$.

Table 2.5 Hydrogen bonding parameters for piperidine.

2.4.2 Evidence of other phases of piperidine

There was no evidence of a second phase of piperidine in the low temperature neutron powder diffraction study which is in agreement with the first DSC traces recorded, however this is not consistent with the findings of Parkin *et al.* (2004). This inconsistency is unlikely to be simply due to deuteration of the sample for the neutron study as the same features were observed in the initial DSC traces of piperidine-h_{11} and piperidine-d_{11}. The difference in melting/freezing temperatures between the two is to be expected as isotopologues usually have slightly different melting points.

The second DSC traces recorded on the same samples indicated that there are other phases of piperidine accessible *via* changes in temperature. The significant differences between the first and second DSC traces recorded for a particular sample suggest that the thermal history of the sample may influence the phase behaviour. Multiple crystallisations were performed using the same sample in the low temperature neutron study however only one phase was obtained irrespective of the method of crystallisation.

During the high pressure study the sample was seen to melt over a period of four hours as the pressure slowly decreased thus the known phase transforms directly to the melt. Increasing the pressure to recrystallise the sample produced the same phase therefore there is no evidence of another phase close to the melting point.

2.5 Conclusions

The effect of temperature on the crystal structure of piperidine has been investigated using neutron powder diffraction. The structure previously determined by Parkin *et al.* (2004) has been found to remain down to 2 K. On cooling to 2 K a smooth reduction in unit cell volume is observed with the N1-H1…N1 hydrogen bonds linking the molecules into chains shortening to 2.141(3) Å at 2 K. There are no significant changes to the structure on cooling. Further crystallisations under different conditions did not indicate a second phase of piperidine close to the melting point.

Initial differential scanning calorimetry (DSC) traces recorded for piperidine-h_{11} and piperidine-d_{11} revealed no thermal events other than freezing and melting of the sample. A second trace recorded using the same samples under the same experimental conditions revealed remarkably different behaviour, far more complex than the original traces. The second traces of piperidine-h_{11} and piperidine-d_{11} revealed differing behaviour between the two compounds though in both cases there was evidence of other phases accessible *via* changes in temperature. It is therefore unlikely that the differing behaviour observed in this work and the work of Parkin *et al.* (2004) is simply due to deuteration of the sample. The DSC traces indicate that the thermal history of the sample may influence the phase behaviour of piperidine.

The effect of pressure up to 2.79 GPa at ambient temperature has also been investigated using neutron powder diffraction. Piperidine-d_{11} crystallised in the same phase observed at low temperature upon increasing the pressure to 0.22 GPa. No phase transitions were observed up to 2.79 GPa. The pressure range studied was limited due to peak broadening. The sample was shown to transform directly to the melt from this phase upon decompression. There was no evidence of a second phase close to the melting point.

The overall effect on the structure was similar in both studies, however the perturbation achieved by the application of even modest pressures was greater than achieved by cooling to 2 K.

2.6 References

Angel, R. J. (2004). edited by A. Katrusiak & P. F. McMillan, pp. 21-36.

Birch, F. (1947). *Physical Review* **71**, 809-824.

Buschmann, J., Mueller, E. & Luger, P. (1986). *Acta Crystallographica, Section C* **42**, 873-876.

Busetti, V., Del Pra, A. & Mammi, M. (1969). *Acta Crystallographica, Section B* **25**, 1191-1194.

Coelho, A. (2007). *TOPAS-A: General Profile and Structure Analysis Software for Powder Diffraction Data.*

Fortes, A. D. (2004). PhD thesis, University of London.

Ibberson, R. M. (1996). *J. Appl. Crystallogr.* **29**, 498-500.

Kahn, R., Fourme, R., André, D. & Renaud, M. (1973). *Acta Crystallographica, Section B* **29**, 131-138.

Kuznetsov, A. Z., Dmitriev, V., Dubrovinsky, L., Prakapenka, V. & Weber, H. P. (2002). *Solid State Commun.* **122**.

Marshall, W. G. & Francis, D. J. (2002). *J. Appl. Crystallogr.* **35**, 122-125.

Miller, R. A. & Schuele, D. E. (1969). *J. Phys. Chem. Solids* **30**, 589-600.

Parkin, A., Oswald, I. D. H. & Parsons, S. (2004). *Acta Crystallographica, Section B* **60**, 219-227.

Pravica, M., Shen, Y., Quine, Z., Romano, E. & Hartnett, D. (2007). *J. Phys. Chem. B* **111**, 4103-4108.

Schofield, P. F., Knight, K. S. & Stretton, I. C. (1996). *Am. Mineral.* **81**, 847-851.

Slebodnick, C., Zhao, J., Angel, R., Hanson, B. E., Song, Y., Liu, Z. & Hemley, R. J. (2004). *Inorg. Chem.* **43**, 5245-5252.

Vinet, P., Ferrante, J., Rose, J. H. & Smith, J. R. (1987). *J. Geophys Res* **92**, 9319-9325.

Vinet, P., Ferrante, J., Smith, J. R. & Rose, J. H. (1986). *J Phys C: Solid State* **19**, L467-L473.

Waldorf, D. L. & Alers, G. A. (1962). *Journal of Applied Physics* **33**, 3266-3269.

Wilding, N. B., Crain, J., Hatton, P. D. & Bushnell-Wye, G. (1993). *Acta Crystallographica, Section B* **49**, 320-328.

Wilding, N. B., Hatton, P. D. & Pawley, G. S. (1991). *Acta Crystallographica, Section B* **47**.

Wood, P. A., Forgan, R. S., Henderson, D., Parsons, S., Pidcock, E., Tasker, P. A. & Warren, J. E. (2006). *Acta Crystallographica Section B* **62**, 1099-1111.

Chapter 3
Low temperature studies of N-methylformamide and N,N-dimethylformamide

3.1 Introduction

Simple amides are of interest for several reasons; in particular they provide simple models of peptide bonds. Formamide is the simplest molecule containing the CONH moiety of the peptide bond and as such has been the subject of a number of structural and theoretical studies, however the closely related compound N-methylformamide (NMF) has also been used to model the peptide bond.

Although the structure of NMF in the liquid phase and amorphous NMF have been the focus of a number of studies (Nasr *et al.*, 2005; Bour *et al.*, 1998; Ludwig *et al.*, 1997), the crystal structure has only relatively recently been determined by X-ray single crystal diffraction (Dawson, 2003). Differential scanning calorimetry (DSC) revealed features other than the melting and freezing of the sample. On heating, a trough was observed at 168 K, followed by a small peak at 223 K before the main melting peak at 271 K. Although Dawson (2003) determined the crystal structure at a number of temperatures no phase transitions were observed.

Further substituting NMF gives the related compound N,N-dimethylformamide (DMF) which also exhibits interesting behaviour at low temperature. The crystal structure was determined by Borrmann *et al.* (2000) at 90 K. They also observed an amorphous-crystalline phase transition at 148 K and a solid-solid transition at 179 K on heating. Dawson (2003) reported that the DSC trace of DMF reveals an exothermic event at 198 K just before the onset of melting but did not observe either of the transitions reported by Borrmann *et al.* (2000).

Variable temperature neutron powder diffraction studies on NMF and DMF have been performed in order to investigate the behaviour of these compounds at low temperature more closely.

3.2 Experimental

N-methylformamide-d_5 and N,N-dimethylformamide-d_7 were obtained from CDN Isotopes and used as received.

3.2.1 N-methylformamide

Variable temperature time-of-flight neutron powder diffraction data were recorded using the HRPD instrument at ISIS. The liquid N-methylformamide (NMF) was loaded into a rectangular aluminium sample can filled with glass wool. The glass wool was included as previous studies have shown it to aid formation of small crystallites and avoid the effects of preferred orientation. Once the sample can was sealed it was quenched in liquid nitrogen before being cooled to 2 K in a cryostat. After confirming the sample was in the known phase, data were collected every 3 K in a rapid scan from 10 K to 228 K.

Initial analysis of the unit cell parameters extracted from the rapid data collections revealed a smooth variation until 155 K. Beyond this temperature the lattice constants deviated from a smooth expansion. In order to investigate this behaviour further, longer data collections suitable for Rietveld analysis were performed on a second sample. The sample was cold-ground (Ibberson, 1996) in a liquid nitrogen chilled stainless steel mortar inside a glove box under a cold dry nitrogen atmosphere before being loaded into a cylindrical vanadium sample can and cooled in a cryostat to 2 K. Data were collected at 2 K, 170 K and 228 K.

3.2.2 N,N-dimethylformamide

Variable temperature time-of-flight neutron powder diffraction data were recorded using the HRPD instrument at ISIS. As N, N-dimethylformamide (DMF) is liquid under ambient conditions, the sample was cold-ground in a liquid nitrogen chilled stainless steel mortar before being loaded into a rectangular aluminium sample can fitted with a heater. The sample was then placed in a cryostat and cooled to 2 K. After confirming the sample was in the known phase, data suitable for Rietveld analysis were collected at 2 K. Data were then collected every 2 K in a rapid scan up to 208 K.

Initial analysis of the unit cell parameters showed a smooth variation up to 186 K, however above this temperature the *c* axis deviated from the smooth expansion, indicating some form of transition. The sample was cooled to 185 K and data collected.

3.2.3 Structure refinement

All refinements were performed using TOPAS-Academic (Coelho, 2007). Pawley fits (Pawley, 1981) were performed on all rapid scan data to extract lattice parameters. During Rietveld refinement the molecules were treated as rigid groups using the Z-matrix formalism in TOPAS.

N-methylformamide

Bond lengths and angles for the CNO skeleton of the molecule were taken from the structure determined by Dawson (2003) and not refined. C-D distances were refined, with all distances within a given methyl group constrained to be equal. Bond angles and torsions were refined for the methyl groups such that they retained a regular shape. At 2 K the thermal motion was modelled isotropically. At 170 K and 228 K anisotropic displacement parameters were modelled using the TLS formalism. As the TLS method works in Cartesian coordinates the calculated displacement parameters were subsequently converted back to the monoclinic crystal axis frame. Additional parameters were required to model the behaviour of the methyl groups with an extra set of libration, L, and correlation, S, parameters included for each of the methyl groups. Based on the magnitude of the anisotropic displacement parameters, the methyl group of molecule 1 (based on C11) exhibited significantly more thermal motion than the methyl group or molecule 2 (based on C12). The deuterium atoms of this methyl group were therefore modelled in two orientations and the occupancy refined. A common isotropic displacement parameter was refined for each of the orientations instead of the TLS formalism. A second order spherical harmonics preferred orientation correction was also included in the refinements. Rietveld refinement profiles are shown in Figure 3.1, with crystal and refinement data given in Table 3.1.

N,N-dimethylformamide

As for N-methylformamide, bond lengths and angles for the CNO skeleton of the molecule taken from the previously determined structure (Borrmann *et al.*, 2000, CSD refcode KAQPUN) and not refined. C-D distances were refined, with all distances within a given methyl group constrained to be equal. Bond angles and torsions were refined for the methyl groups such that they retained a regular shape. At 2 K the thermal motion was modelled isotropically. At 185 K and 208 K anisotropic displacement parameters were modelled using the TLS formalism. The anisotropic displacement parameters were converted from the Cartesian axis frame of the TLS model to the triclinic crystal frame using the method described in Section 1.2.4.4. Based on the magnitude of the anisotropic displacement parameters, one of the four methyl groups in the asymmetric unit exhibited significantly more thermal motion than the other methyl groups in the asymmetric unit. Additional libration, L, and correlation, S, parameters were included to model this behaviour. Rietveld refinement profiles are shown in Figure 3.2, with crystal and refinement data given in Table 3.2.

3.2.3 Differential Scanning Calorimetry

Differential scanning calorimetry (DSC) traces were recorded on N-methylformamide-d_5 and N,N-dimethylformamide-d_7 using a Perkin Elmer Pyris 1 DSC instrument with the samples contained in closed aluminium pans. Samples were loaded at room temperature and initially cooled to 100 K and then heated to 293 K at a rate of 10 K/min.

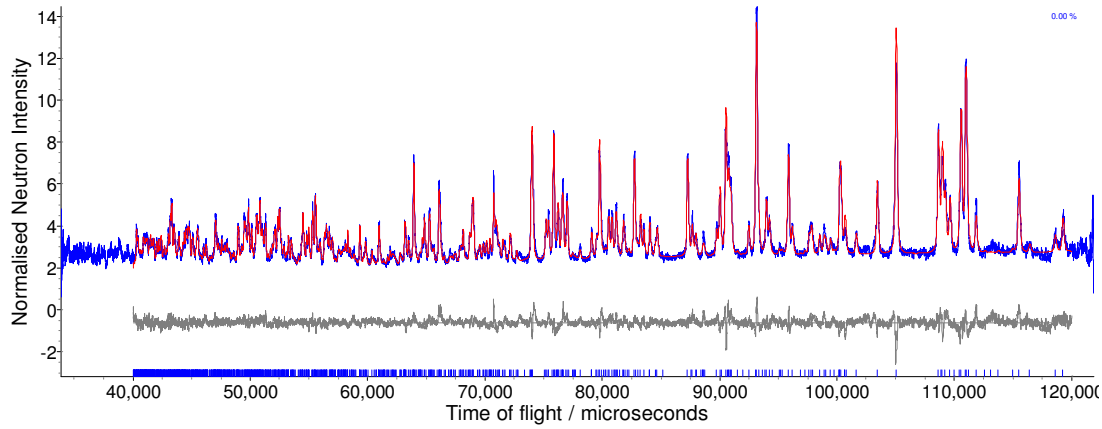

(a) 2 K

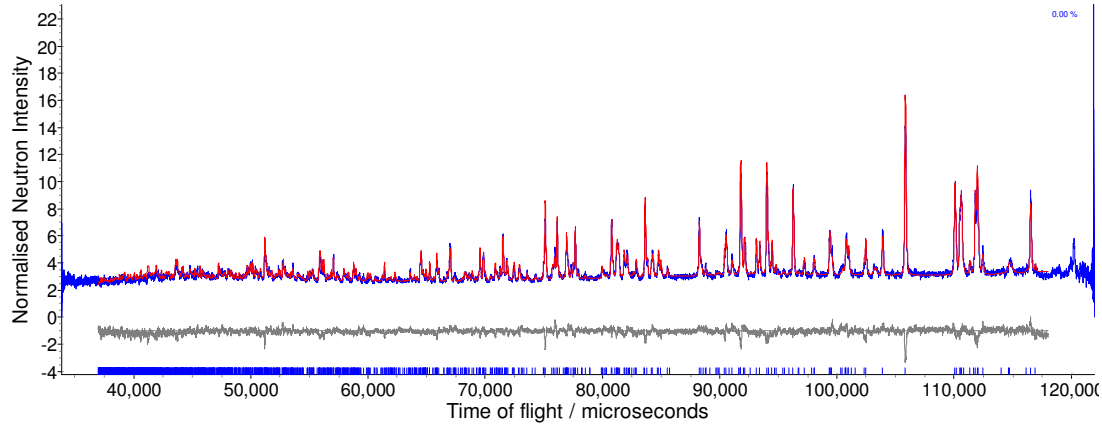

(b) 170 K

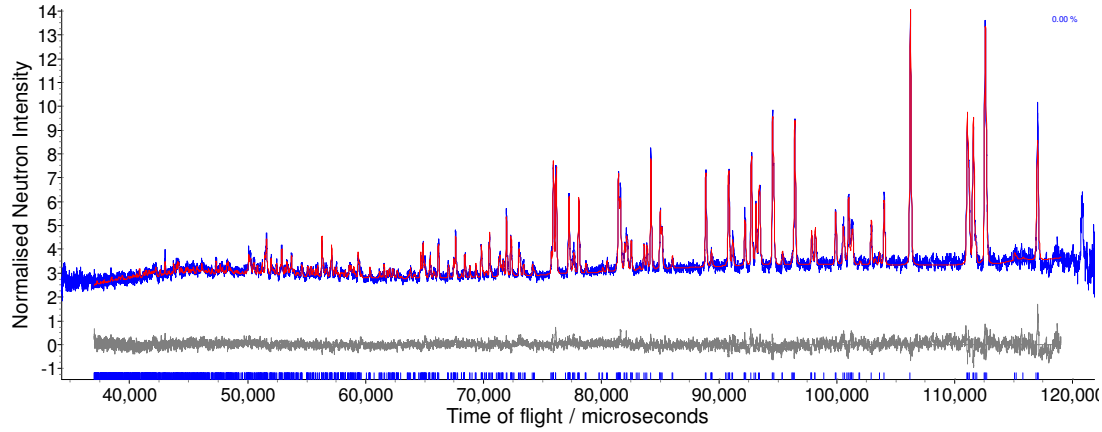

(c) 228 K

Figure 3.1 Rietveld refinement profiles for NMF. Blue and red lines correspond to observed and calculated data respectively. The difference is shown in grey.

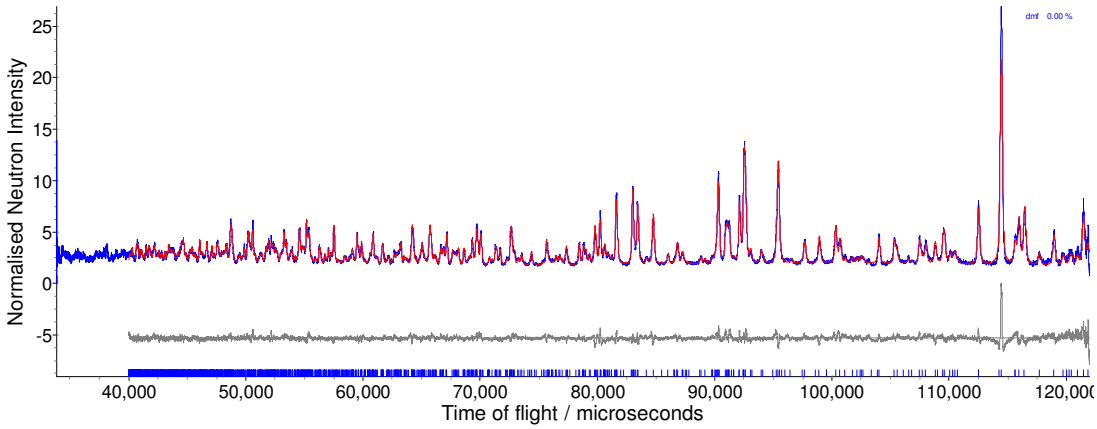

(a) 2 K

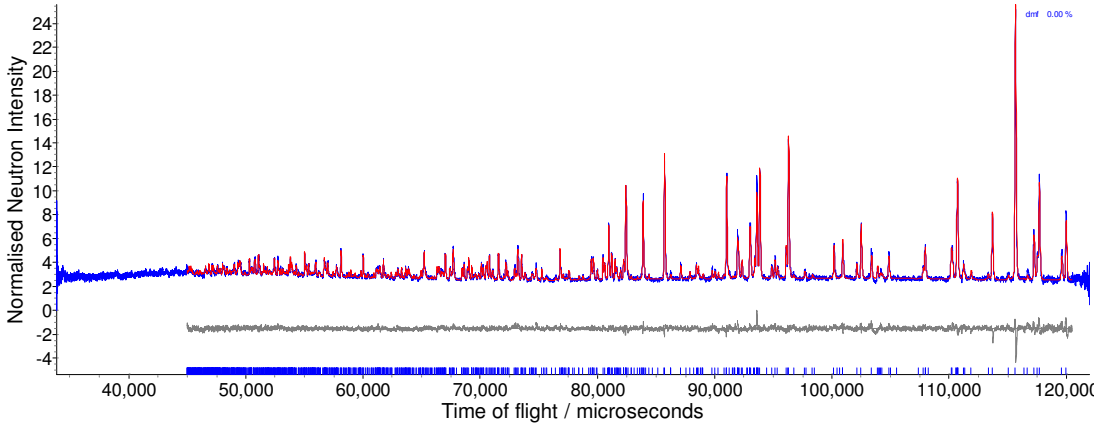

(b) 185 K

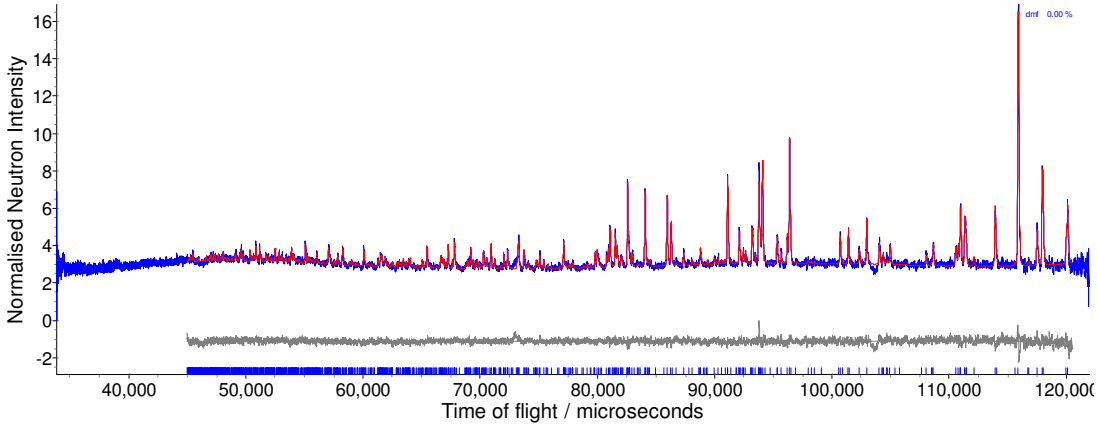

(c) 208 K

Figure 3.2 Rietveld refinement profiles for DMF. Blue and red lines correspond to observed and calculated data respectively. The difference is shown in grey.

N-methylformamide-d_5			
Temperature (K)	2	170	228
Crystal Data			
Chemical formula	C_2D_5NO	C_2D_5NO	C_2D_5NO
M_r	64.08	64.08	64.08
Cell setting, space group	Monoclinic, $P2_1/c$	Monoclinic, $P2_1/c$	Monoclinic, $P2_1/c$
a, b, c (Å)	8.70134(5), 8.33996(6), 8.56807(6)	8.76711(4), 8.47668(5), 8.60610(5)	8.79940(4), 8.58194(5), 8.61445(6)
α, β, γ (°)	90, 90.4907(6), 90	90, 90.2156(5), 90	90, 90.0601(6), 90
V (Å^3)	621.752(7)	639.57(1)	650.53(1)
Z	4	4	4
D_{calc} (g cm^{-3})	1.369	1.331	1.309
Radiation type	Neutron	Neutron	Neutron
Specimen form	Powder	Powder	Powder
Data Collection			
Diffractometer	HRPD, ISIS	HRPD, ISIS	HRPD, ISIS
Collection method	Time of flight	Time of flight	Time of flight
Range of *d* (Å)	0.83 – 2.49	0.77 – 2.44	0.77 – 2.46
Refinement			
Method	Rietveld	Rietveld	Rietveld
R_p	4.114	3.356	3.344
R_{wp}	5.004	4.036	3.958
S	1.654	1.260	1.171
Background	6 term Chebychev polynomial	6 term Chebychev polynomial	6 term Chebychev polynomial
Profile function	Back to back exponential	Back to back exponential	Back to back exponential
Number of parameters	53	97	97
Weighting scheme	$1/\sigma^2$	$1/\sigma^2$	$1/\sigma^2$

Table 3.1 Crystal and refinement data for NMF.

N,N-dimethylformamide-d_7			
Temperature (K)	2	185	208
Crystal Data			
Chemical formula	C_3D_7NO	C_3D_7NO	C_3D_7NO
M_r	80.11	80.11	80.11
Cell setting, space group	Triclinic, $P\bar{1}$	Triclinic, $P\bar{1}$	Triclinic, $P\bar{1}$
a, b, c (Å)	5.91421(4), 6.93334(5), 10.36291(7)	5.99218(2), 7.12041(3), 10.45245(4)	6.00442(3), 7.16734(5), 10.46634(5)
α, β, γ (°)	77.1872(7), 88.1610(6), 75.6129(7)	77.2890(4), 88.2638(3), 75.0933(4)	77.3522(6), 88.3450(5), 75.0285(6)
V (Å^3)	401.239(5)	420.24(1)	424.40(1)
Z	4	4	4
D_{calc} (g cm^{-3})	1.326	1.266	1.254
Radiation type	Neutron	Neutron	Neutron
Specimen form	Powder	Powder	Powder
Data Collection			
Diffractometer	HRPD, ISIS	HRPD, ISIS	HRPD, ISIS
Collection method	Time of flight	Time of flight	Time of flight
Range of *d* (Å)	0.83 - 2.50	0.93 - 2.50	0.93 - 2.50
Refinement			
Method	Rietveld	Rietveld	Rietveld
R_p	4.785	3.121	2.789
R_{wp}	5.592	3.713	3.360
S	1.783	1.288	1.141
Background	6 term Chebychev polynomial	6 term Chebychev polynomial	6 term Chebychev polynomial
Profile function	Back to back exponential	Back to back exponential	Back to back exponential
Number of parameters	72	88	88
Weighting scheme	$1/\sigma^2$	$1/\sigma^2$	$1/\sigma^2$

Table 3.2 Crystal and refinement data for DMF.

3.3 Results

The effect of temperature on the crystal structures of N-methylformamide and N,N-dimethylformamide have been investigated using neutron powder diffraction. Both compounds exhibit a discontinuity in the temperature dependence of the lattice parameters related to the onset of methyl group rotation.

3.3.1 Crystal structure of N-methylformamide

The crystal structure of N-methylformamide (NMF) has previously been determined by Dawson (2003). At low temperature it crystallises in the monoclinic space group $P2_1/c$ with two molecules in the asymmetric unit. Each of the independent molecules forms two N-H…O hydrogen bonds (1.866(4) and 1.831(4) Å at 2 K) which link the molecules into four-fold helical chains parallel to the *b* axis, Figure 3.3. The helices are interleaved parallel to the *c* axis however there are no hydrogen bonding interactions between them.

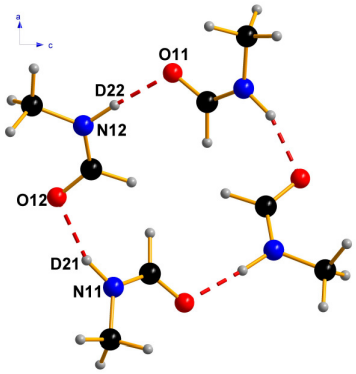

(a) Four-fold helix

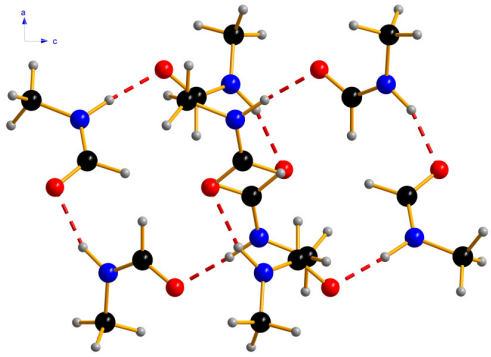

(b) Interleaved helices

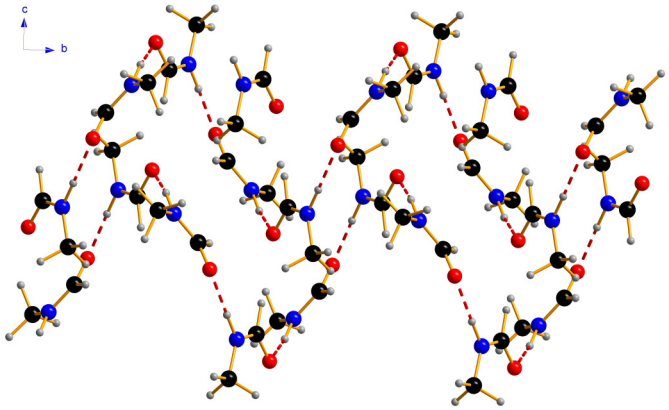

(c) Interleaved helices parallel to *c* axis

Figure 3.3 Interleaved hydrogen bonded helices in NMF.

3.3.2 Effect of temperature on the structure of N-methylformamide

The low temperature behaviour of NMF was surveyed *via* a rapid scan from 10 K to 228 K with data collected every 3 K. The extracted lattice parameters are displayed in Figure 3.4 and listed in the e-appendix. The data exhibit a smooth expansion of the unit cell up to 155 K. Above this temperature a deviation from the smooth expansion of the lattice parameters *a*, *b* and *c* was observed, with the *c* axis exhibiting the most significant deviation.

The increase in the unit cell volume between 10 K and 228 K is 31.39 $Å^3$ which represents 5 % of the volume at 10 K. On increasing the temperature from 10 K to 228 K the *b* axis undergoes the largest expansion, increasing by 0.27 Å, corresponding to 3.24 % of the 10 K value. The effect of temperature on the *a* and *c* axes is much smaller with expansions of 1.19 % and 0.55 % of the 10 K values respectively. The angle β decreases by 0.52 ° (-0.55 %) on increasing the temperature to 228 K.

The unit cell parameters up to the transition at 155 K were initially fitted to an Einstein expression of the form $X = X_o + K/(e^{\theta/T} - 1)$ where X_o is the parameter X at 0 K, K is the Einstein constant, T is the temperature in Kelvin between 10 and 155 K and θ is the effective Einstein temperature. The results of the fits are listed in Table 3.3. The lattice parameters *a* and β are well fitted to an expression of this form, as illustrated in Figure 3.4, however the variation of the *b* axis, *c* axis and the unit cell volume were not as well modelled using this expression. The Einstein model assumes a single frequency for all oscillations which is evidently not the case in NMF. Addition of a second Einstein term results in an expression of the form $X = X_o + K_1/(e^{\theta_1/T} - 1) + K_2/(e^{\theta_2/T} - 1)$ where X_o is the parameter X at 0 K, K_1 and K_2 are the Einstein constants, T is the temperature in Kelvin between 10 and 155 K and θ_1 and θ_2 are the effective Einstein temperatures. The variation of the *b* axis and the unit cell volume are well fitted to a double-Einstein expression of this form as shown in Figure 3.4. Neither the single nor double Einstein expressions accurately model the variation of the *c* axis, particularly above 155 K, indicating that the effect of temperature on this axis is more complicated.

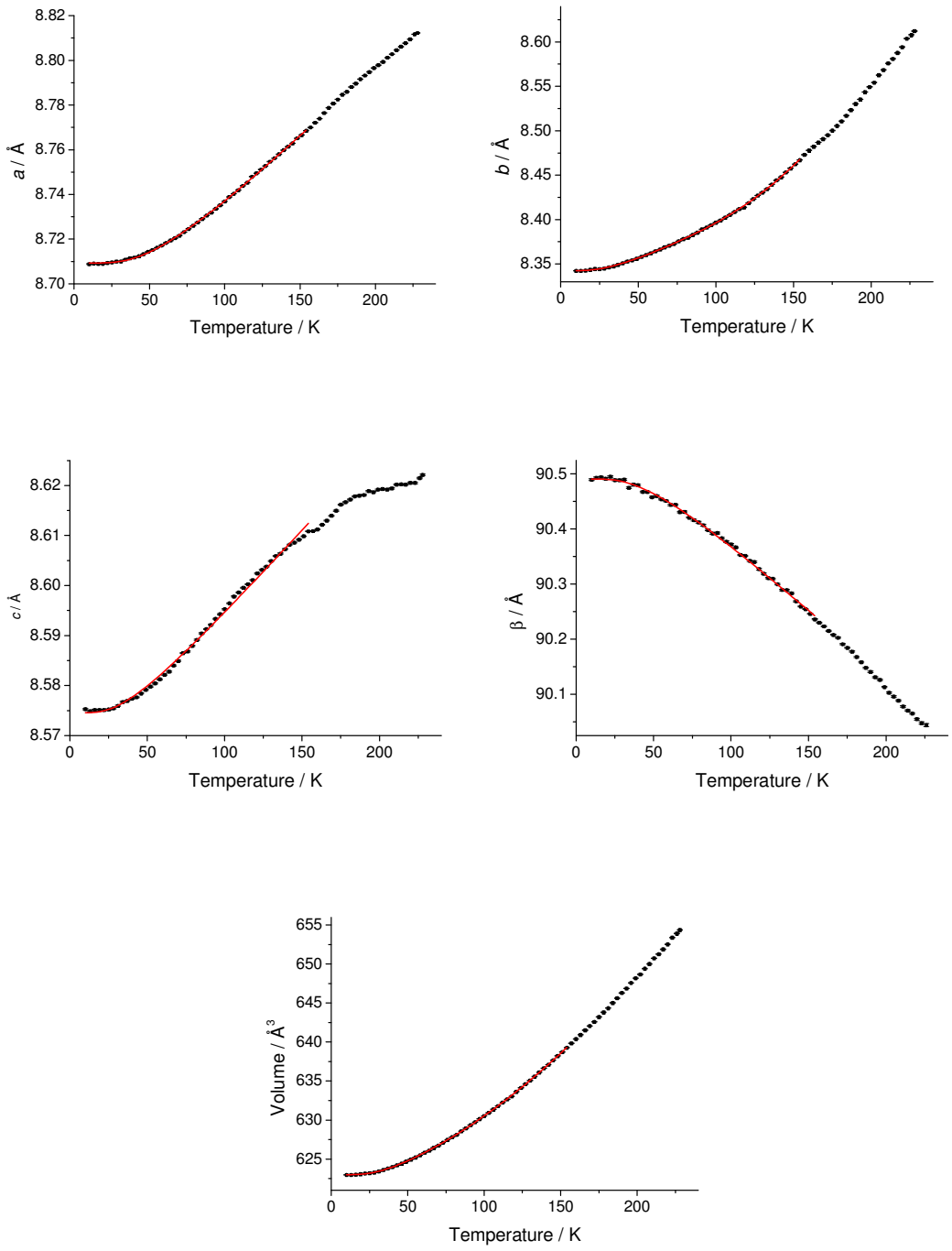

Figure 3.4 Variation of the lattice parameters and volume of NMF as a function of temperature. The calculated fits up to 155 K for *a*, *c* and *β* are represented by single Einstein functions with *b* and the volume represented by double-Einstein functions.

	X_o	K_1	θ_1 / K	K_2	θ_2 / K	Adjusted R^2
a	8.7093(1) Å	0.1032(17)	155(2)	-	-	0.99976
b	8.3426(2) Å	0.083(4)	96(3)	3.2(6)	726(36)	0.99986*
c	8.5746(3) Å	0.035(2)	100(5)	-	-	0.99696
β	90.4905(13) °	-0.333(17)	131(5)	-	-	0.99795
Volume	623.014(14) Å^3	14.5(6)	111(2)	75(9)	523(29)	0.99996*

* Adjusted R^2 for single Einstein function; *b* axis 0.99579, volume 0.99122.

Table 3.3 Results from the Einstein function data-fitting.

The instantaneous thermal expansion (Schofield *et al.*, 1996) is related to the unit cell parameter X, where $\alpha_X = (1/X_o)(\delta X/\delta T)$. The resultant expressions for single and double Einstein expressions are given in Equations 3.1 and 3.2, respectively. The values for $K_1\theta_1/X_o$ and $K_2\theta_2/X_o$, as appropriate, for each of the cell parameters are given in Table 3.4.

.

$$\alpha_X = \left(\frac{1}{X_o}\right)\left(\frac{\delta X}{\delta T}\right) = \frac{K_1\theta_1}{X_o}\cdot\left[\frac{e^{\theta_1/T}}{(e^{\theta_1/T}-1)^2T^2}\right] \qquad (3.1)$$

$$\alpha_X = \left(\frac{1}{X_o}\right)\left(\frac{\delta X}{\delta T}\right) = \frac{K_1\theta_1}{X_o}\cdot\left[\frac{e^{\theta_1/T}}{(e^{\theta_1/T}-1)^2T^2}\right] + \frac{K_2\theta_2}{X_o}\cdot\left[\frac{e^{\theta_2/T}}{(e^{\theta_2/T}-1)^2T^2}\right] \qquad (3.2)$$

	$K_1\theta_1/X_o$	$K_2\theta_2/X_o$
a	1.837	-
b	278.474	0.955
c	0.408	-
β	-0.482	-
Volume	62.960	2.583

Table 3.4 Fitting parameters for thermal expansion coefficients of NMF.

In mineralogical studies, a Taylor expansion is used to simplify the expression for the thermal expansion. At high temperatures $e^{\theta/T} \approx 1+(\theta/T)$, which results in Equations 3.3 and 3.4 for single and double Einstein expressions respectively. Such a simplification is not valid for NMF due to the extremely high temperatures required, however, the resultant fitting parameters are given in Table 3.5 for comparison.

$$\left(\frac{1}{X_o}\right)\left(\frac{\delta X}{\delta T}\right) \approx \frac{K_1}{(X_o\theta_1)} \cdot \left[1+\left(\frac{\theta_1}{T}\right)\right] \tag{3.3}$$

$$\left(\frac{1}{X_o}\right)\left(\frac{\delta X}{\delta T}\right) \approx \frac{K_1}{(X_o\theta_1)} \cdot \left[1+\left(\frac{\theta_1}{T}\right)\right] + \frac{K_2}{(X_o\theta_2)} \cdot \left[1+\left(\frac{\theta_2}{T}\right)\right] \tag{3.4}$$

	$K_1 / X_o\theta_1$	$K_2 / X_o\theta_2$
a	7.645 x 10^{-5}	-
b	5.283 x 10^{-4}	1.036 x 10^{-4}
c	4.083 x 10^{-5}	-
β	-2.809 x 10^{-5}	-
Volume	2.302 x 10^{-4}	2.097 x 10^{-4}

Table 3.5 Fitting parameters for thermal expansion coefficients of NMF using high temperature simplification.

The thermal expansion coefficient for the *b* axis is significantly larger than that for the *a* axis indicating that changes in temperature have a larger effect on the *b* axis.

The lengths of the N-H…O hydrogen are shown in Table 3.6. There is very little difference in the hydrogen bond lengths under the conditions of this study. The only significant change observed in the structure is in the length of the *b* axis, which relates to the expansion length of the helix. This can be seen by considering the angle between three molecules as a function of temperature, Table 3.7.

Temperature / K	N12-D22…O11 / Å	N11-D21…O12 / Å
2	1.831(4)	1.886(4)
170	1.876(4)	1.891(4)
228	1.888(6)	1.900(5)

Table 3.6 Hydrogen bond lengths for NMF.

Temperature / K	Angle / °
2	66.75
170	67.55
228	68.70

Table 3.7 Helix angle in NMF.

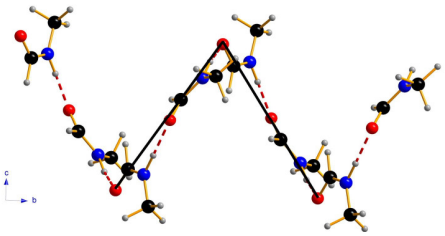

3.3.3 Crystal structure of N, N-dimethylformamide

The crystal structure of N,N-dimethylformamide has previously been determined at 90 K by Borrmann *et al.* (2000). At low temperature it crystallises in the space group $P\bar{1}$ with two molecules in the asymmetric unit. The only significant interactions are weak C-H…O interactions involving the formyl protons (2.262(6) Å at 2 K) and methyl protons (2.328(5) Å at 2 K) linking the molecules into four-fold centrosymmetric rings, Figure 3.5. The four-fold rings are linked together *via* dimer units (2.523(5) Å at 2 K) to form ribbons. The structure is related to the crystal structures observed in formamide, which also exhibit dimers and ring motifs, with C-H…O interactions replacing the N-H…O interactions in formamide.

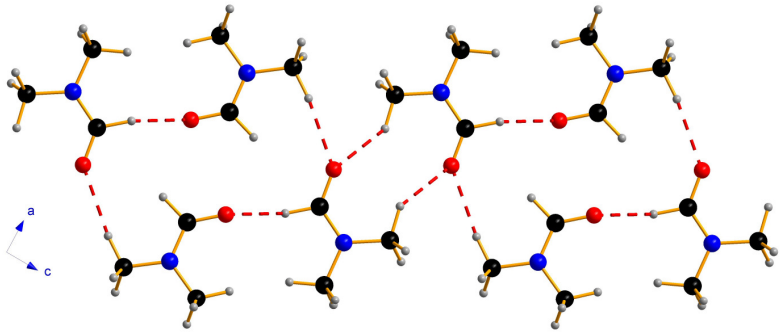

Figure 3.5 Four-fold rings linked by dimer units in DMF.

3.3.4 Effect of temperature on the structure of N, N-dimethylformamide

The low temperature behaviour of DMF was surveyed *via* a rapid scan from 2 K to 208 K with data collected every 2 K. The extracted lattice parameters are displayed in Figure 3.6 and listed in the e-appendix. A smooth variation of the lattice parameters is observed up to 184 K. Above this temperature there is a small deviation from the smooth curve, indicating a possible transition.

The unit cell volume increases by 23.11 $Å^3$ on increasing the temperature from 2 K to 208 K which represents 5.76 % of the volume at 2 K. The unit cell parameters exhibit an anisotropic response to changing temperature, with the largest change observed in the *b* axis which increases by 3.36 % of the 2 K value. Changes in temperature have a much smaller effect on the *a* and *c* axes. On increasing the temperature from 2 K to 208 K they increase by 1.53 % and 0.99 % respectively. Within the temperature range studied very little change is observed in the unit cell angles α and β (0.22 %) and the angle γ decreases by 0.78 % of the 2 K value.

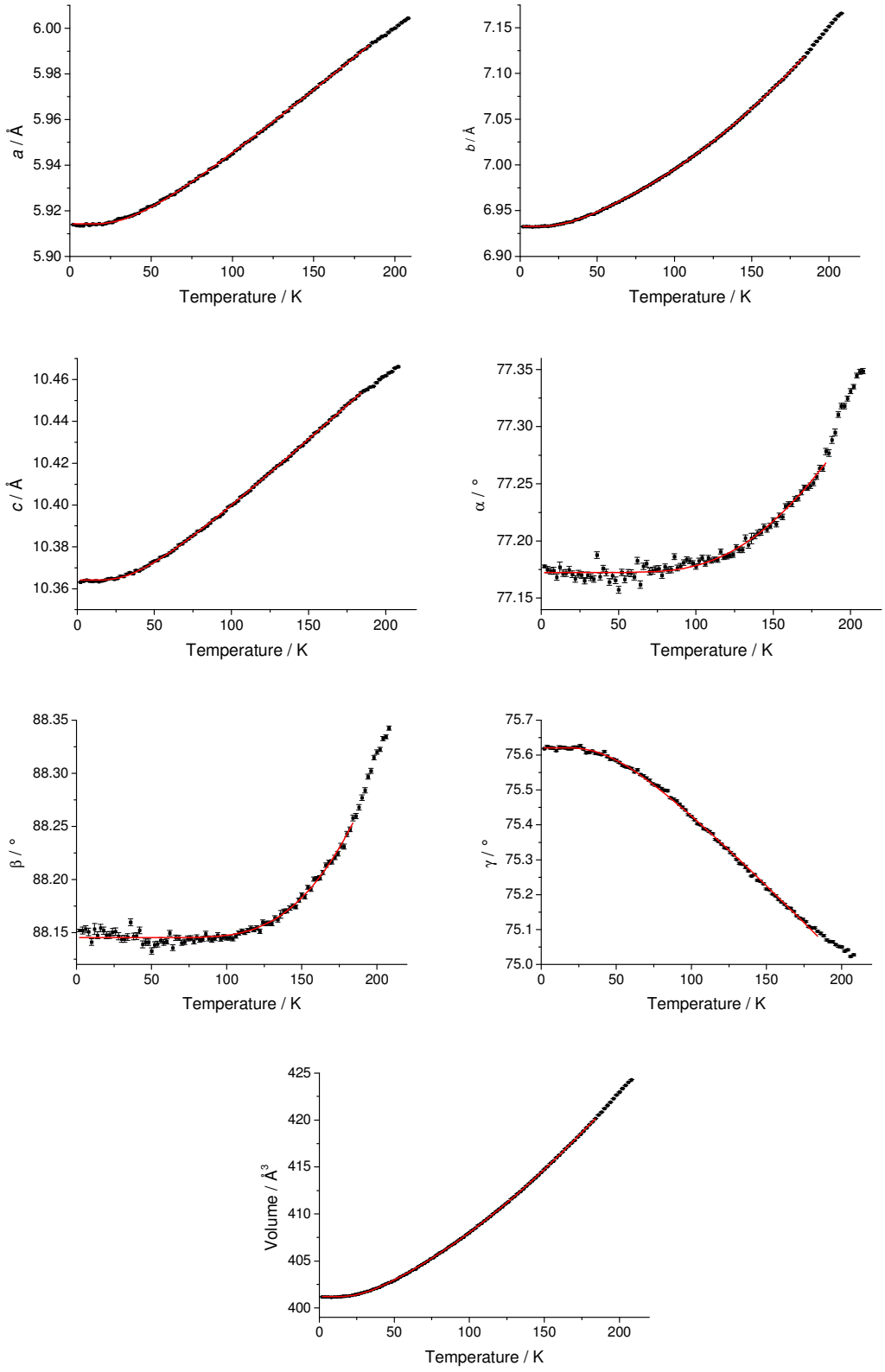

Figure 3.6 Variation of the lattice parameters and volume of DMF as a function of temperature. The calculated fits for *a*, *c*, *α*, *β* and *γ* are represented by single Einstein functions with *b* and the volume represented by double-Einstein functions.

The unit cell parameters up to the transition at 184 K were initially fitted to an Einstein expression of the form $X = X_o + K/(e^{\theta/T} - 1)$ as described in Section 3.3.2 for NMF. All of the lattice parameters except for the *b* axis and the unit cell volume are well fitted to an expression of this form, as illustrated in Figure 3.6. The variation of the *b* axis and the unit cell volume are well fitted to a double-Einstein expression of the form described in Section 3.3.2, illustrated in Figure 3.6. The Einstein model assumes a single frequency for all oscillations, however the need to include a second frequency indicates that both intermolecular and intramolecular modes need consideration. The results of the fits are listed in Table 3.8.

	X_o	K_1	θ_1 / K	K_2	θ_2 / K	Adjusted R^2
a	5.91428(9) Å	0.0700(10)	118(1)	-	-	0.99998
b	6.93279(1) Å	0.104(3)	101(1)	1.01(5)	588(12)	0.99997
c	10.36409(9) Å	0.0787(9)	116(1)	-	-	0.99984
α	77.1724(7) °	2.4(4)	600(27)	-	-	0.97351
β	88.1453(6) °	11(2)	849(31)	-	-	0.97939
γ	75.6207(12) °	-0.675(16)	149(2)	-	-	0.99907
Volume	401.2126(8) Å^3	11.19(2)	100(1)	62(3)	545(13)	0.99998

Table 3.8 Results from the Einstein function data-fitting for DMF.

The instantaneous thermal expansion is related to the unit cell parameter X, where $\alpha_X = (1/X_o)(\delta X/\delta T)$. The resultant general expressions for single and double Einstein expressions are given in Equations 3.1 and 3.2, respectively. The values for $K_1\theta_1 / X_o$ and $K_2\theta_2 / X_o$, as appropriate, for each of the cell parameters are given in Table 3.9. The corresponding parameters for the simplified equations (3.3 and 3.4) used in mineralogical studies are listed in Table 3.10.

.	$K_1\theta_1 / X_o$	$K_2\theta_2 / X_o$
a	1.397	-
b	1.515	85.662
c	0.881	-
α	18.659	-
β	105.950	-
γ	-1.330	-
Volume	2.789	84.220

Table 3.9 Fitting parameters for thermal expansion coefficients of DMF.

	$K_1 / X_o\theta_1$	$K_2 / X_o\theta_2$
a	1.003×10^{-4}	-
b	1.485×10^{-4}	2.478×10^{-4}
c	6.546×10^{-5}	-
α	5.183×10^{-5}	
β	1.470×10^{-5}	-
γ	-5.991×10^{-5}	
Volume	2.789×10^{-4}	2.835×10^{-4}

Table 3.10 Fitting parameters for thermal expansion coefficients of DMF using high temperature simplification.

The thermal expansion coefficient for the *b* axis is much greater than for the *a* and *c* axes highlighting that changes in temperature primarily effect the interlayer separation of the hydrogen bonded ribbons. There are no significant changes in the C-H…O interaction lengths under the conditions of this study.

3.3.5 Differential scanning calorimetry

Differential scanning calorimetry (DSC) traces were recorded for N-methylformamide–d_5 and N, N-dimethylformamide-d_7 and are shown in Figure 3.7. On cooling N-methyl formamide-d_5 a sharp transition was observed at 211 K due to the sample freezing. The only feature of the heating cycle was the sample melting which appears as a broad peak at 268 K. There is no evidence of the trough observed by Dawson (2003) at 168 K.

The only feature on cooling N,N-dimethylformamide-d_7 is a small trough due to crystallisation at 179 K, however the heating cycle contains more features. On heating a small peak is observed at 136 K followed by a trough at 164 K. The sample melting occurs as a broad peak at 207 K.

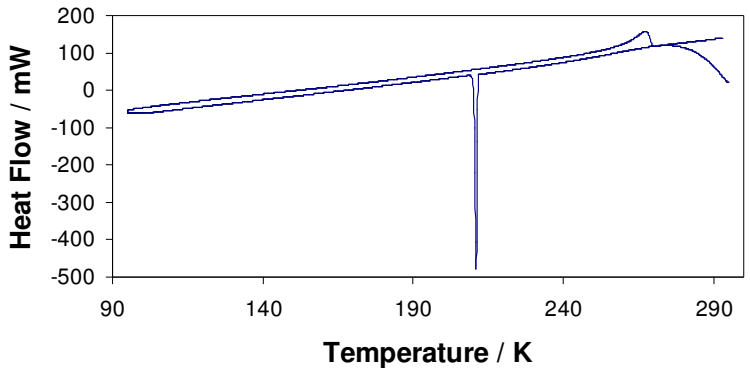

(a) NMF

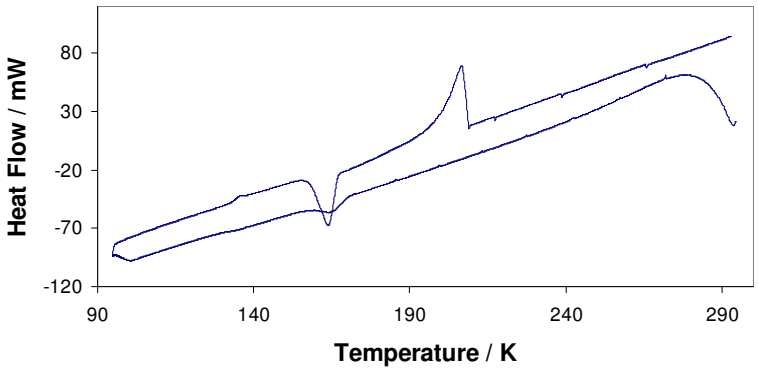

(b) DMF

Figure 3.7 Differential scanning calorimetry traces for NMF and DMF.

3.4 Discussion

3.4.1 Effect of temperature on methyl group motion in NMF

As X-ray single crystal diffraction studies by Dawson (2003) confirmed that NMF does not undergo a structural transition, the discontinuity in the temperature dependence of the lattice parameters must be related to subtle changes in the structure, in particular changes in the thermal motion.

At 2 K the thermal motion of the molecules is adequately modelled using isotropic displacement parameters. The methyl groups have more freedom of motion than the main CNO skeleton of the molecules; however each methyl group adopts a single orientation.

Anisotropic displacement parameters were modelled using the TLS formalism at 170 K. This temperature is just above the discontinuity in the temperature dependence of the lattice parameters. Unsurprisingly, analysis of the anisotropic displacement parameters revealed that the amplitude of motion of the methyl groups was greater than the CNO skeleton of the molecules and a more complicated model was required. Additional libration, L, and correlation, S, parameters were included allow the methyl groups to rotate separately to the main body of the molecule. Additional translation, T, parameters were not required as the methyl group cannot translate independently of the rest of the molecule. Whilst this modelled the motion of molecule 2 (based on C12), the methyl group of molecule 1 (based on C11) exhibited more complex behaviour. The methyl group of molecule 1 was modelled isotropically in two orientations and the occupancy refined. The occupancy of the alternative orientation refined to 0.307(13) indicating that the methyl group is rotating and is no longer fixed in a single orientation. The discontinuity in the temperature dependence of the lattice parameters is due to the onset of the rotation of this methyl group. At 228 K the occupancy of the alternative orientation has increased to 0.383(19). While the amplitude of motion of the methyl group on molecule 2 has increased, the inclusion of a second orientation is not necessary.

It is interesting to note that the methyl group on one of molecules in the asymmetric unit is rotating more than the other. The crystal structure consists of layers of interleaved helices. The closest contacts between the layers are methyl-methyl contacts (C…C 3.825 Å at 170 K) and it is these methyl groups, circled in Figure 3.8, which are rotating at 170 K.

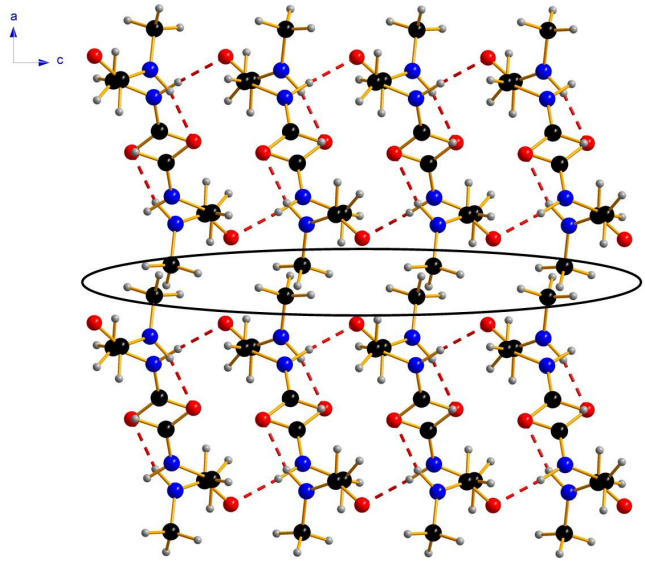

Figure 3.8 Methyl-methyl contacts between layers of interleaved helices in NMF.

There was no evidence of this transition in the DSC trace of NMF-d_5, though Dawson (2003) observed an exothermic event at 168 K in the DSC trace of NMF-h_5. The difference between the two DSC traces may be due to effects of deuteration or differing experimental conditions. The discrepancy between the temperature observed in the DSC trace and that determined from analysis of the lattice parameters may be a result of the temperature equilibrating between data collections in the neutron powder diffraction study compared to the situation in DSC where the temperature is increased at a constant rate. Thus the temperature of the transition may appear higher in the DSC trace.

3.4.2 Effect of temperature on methyl group motion in DMF

At 2 K the thermal motion of the molecules is adequately modelled using isotropic displacement parameters. All of the methyl groups adopt a single orientation, though they exhibit more thermal motion than the main CNO skeleton of the molecules.

At 185 K, the onset of the discontinuity in the temperature dependence of the lattice parameters, anisotropic displacement parameters were modelled using the TLS formalism. While all the methyl groups exhibit a larger amplitude of motion than the main CNO skeleton, the anisotropic displacement parameters for the methyl group of C21 were significantly elongated indicating that it is rotating. Additional libration, L, and correlation, S, parameters were included to allow this methyl group to rotate separately to the main body of the molecule. Additional translation, T, parameters were not required as the methyl group cannot translate independently of the rest of the molecule. The discontinuity in the temperature dependence of the lattice parameters corresponds to the onset of rotation of this methyl group. Even at 208 K, only one of the four independent methyl groups is rotating, with the other three fixed in a single orientation.

Two of the four independent methyl groups (groups C21 and C32) are not involved in forming C-H...O interactions to form ribbons, one of which (C21) is the group which is rotating. Considering the space-filling plot, Figure 3.9, the methyl group of C32, circled in green, are closely packed whereas the methyl group of C21, circled in red, has much more space around it and will therefore have a lower barrier to rotation.

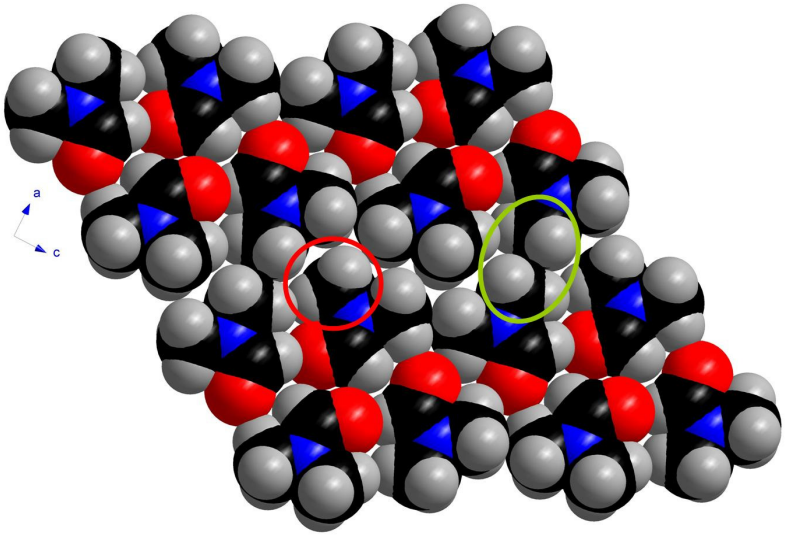

Figure 3.9 Space-filling plot of DMF. Methyl group of C21 circled in red and C32 circled in green.

When a liquid sample is cooled, a sharp exothermic transition associated with the sample crystallising is observed in the DSC trace. However, in the case of DMF, Figure 3.7, only a small trough is observed thus the sample was most likely amorphous. The exothermic transition observed at 164 K on heating is therefore likely to be the sample recrystallising, induced by the onset of the methyl group rotation.

3.5 Conclusions

The effect of temperature on the crystal structure of N-methylformamide (NMF) has been investigated using neutron powder diffraction. The structure previously determined by Dawson (2003) exists from 2 K right up to the melting point. There is little difference in the hydrogen bond lengths under the conditions of the study, with the most significant change observed relating to the expansion of the hydrogen bonded helix.

A discontinuity is observed in the temperature dependence of the lattice parameters at 155 K which corresponds to the onset of rotation of one of the methyl group of one of the independent molecules. The methyl group which is rotating above this temperature forms methyl-methyl contacts between the layers of interleaved helices. The thermal motion of the molecules was modelled using the TLS model with additional parameters required to model the behaviour of the methyl groups.

Neutron powder diffraction has also been used to investigate the effect of temperature on the crystal structure of N,N-dimethylformamide (DMF). The structure previously determined by Borrmann *et al.* (2000) exists across the entire temperature range studied, from 2 K right up to the melting point. There are no significant changes within the C-H…O bonded ribbons with changes in temperature primarily affecting the interlayer separation of the ribbons.

Above 186 K a discontinuity is observed in the temperature dependence of the lattice parameters. Analysis of the anisotropic displacement parameters *via* the TLS method shows this corresponds to the onset of rotation of one of the methyl groups. The

methyl group does not form C-H…O interactions within the ribbons and lies between the hydrogen bonded ribbons.

3.6 References

Borrmann, H., Persson, I., Sandstrom, M. & Stalhandske, C. M. V. (2000). *Journal of the Chemical Society Perkin Transactions 2* **2**, 383-402.

Bour, P., Tam, C. N., Sopkova, J. & Trouw, F. R. (1998). *J. Chem. Phys.* **108**, 351-358.

Coelho, A. (2007). *TOPAS-A: General Profile and Structure Analysis Software for Powder Diffraction Data.*

Dawson, A. (2003). PhD thesis, The University of Edinburgh.

Ibberson, R. M. (1996). *J. Appl. Crystallogr.* **29**, 498-500.

Ludwig, R., Weinhold, F. & Farrar, T. C. (1997). *J. Chem. Phys.* **107**, 499-507.

Nasr, S., Hammami, F. & Bellissent-Funal, M.-C. (2005). *J. Chem. Phys.* **122**.

Pawley, G. S. (1981). *J. Appl. Crystallogr.* **14**, 357-361.

Schofield, P. F., Knight, K. S. & Stretton, I. C. (1996). *Am. Mineral.* **81**, 847-851.

Chapter 4
High-pressure polymorphism in formamide

4.1 Introduction

Formamide is the simplest molecule containing the CONH moiety of the peptide bond and as such has been the subject of a number of structural and theoretical studies. The crystal structure of formamide was first determined by Ladell & Post (1954) at 223 K using X-ray single crystal diffraction. An electron density study at 90 K (Stevens, 1977) and neutron powder diffraction at 20 K (Torrie & Brown, 1994) all found the same monoclinic $P2_1/n$ structure, consisting of N-H...O hydrogen bonded chains of molecules with further hydrogen bonds linking the chains into layers. There are no hydrogen bonding interactions between the layers. Raman spectroscopy has been used to study the behaviour of formamide at low temperatures (Torrie & Brown, 1994) and separately at high pressure (Shimizu *et al.*, 1988). The high pressure study indicated a phase transition at 5.0 GPa, identified by a change in the pressure dependence of the intramolecular and intermolecular vibrational modes.

A number of studies have been performed on the structure of liquid formamide, though the results are contradictory with debate over whether the molecules form chains or rings in the liquid phase (Ohtaki *et al.*, 1983; Miyake *et al.*, 1985). Formamide clusters have also been the subject of a number of theoretical studies, with formamide used as a simple model for examining the N-H...O=C interactions present in biological systems. *Ab initio* calculations show the lowest energy configuration for two formamide molecules to be a cyclic dimer, similar to that seen in the crystal structure (Cabaleiro-Lago & Otero, 2002).

This chapter describes the effect of pressure on the crystal structure of formamide. Formamide has been shown to exhibit remarkable polymorphism at ambient temperature and pressures between 0.1 GPa and 3.6 GPa, forming four new polymorphs. This is in stark contrast to the one structure known under conditions of varying temperature from 2 K right up to the melting point.

4.2 Experimental

4.2.1 X-ray Single Crystal

The X-ray single crystal experiments described in this section were carried out by Alice Dawson. A description of the work is included here for completeness.

A sample of formamide (Aldrich, used as received) was loaded into a Merrill-Bassett diamond anvil cell equipped with 600 μm diamonds and a tungsten gasket. A small ruby chip was also loaded into the cell as a pressure calibrant and the ruby fluorescence method utilised to measure the pressure (Piermarini *et al.*, 1975). Application of pressure caused the sample to crystallise into a polycrystalline mass. This was then heated until the crystallites had been melted back to one seed crystallite.

Several crystals were grown using this method at various pressures. Experiments showed that the low temperature phase (Formamide-I) could be grown at 0.2 GPa while two different previously unknown phases could be grown at 0.3 GPa and 0.4 GPa, which we have designated phases II and IV respectively.

Diffraction data were collected using a Bruker SMART Apex diffractometer equipped with Mo-K_α radiation. Data collection and processing were as described by Dawson *et al.* (2004). Integrations were carried out using the program SAINT (Bruker-Nonius, 2006) and absorption corrections with Absorb5.3, Shade (Parsons, 2004) and Sortav (Blessing, 1995).

Refinement of phase I at 0.2 GPa used the previously determined coordinates (Stevens, 1977, CSD refcode FORMAM02) as a starting point. The structure was refined against $|F|^2$ using SHELXL (Sheldrick, 1997). The two new high pressure structures were solved using direct methods (SHELXS (Sheldrick, 1997)) and refined against $|F|^2$ using SHELXL. All hydrogen atoms were placed geometrically after each cycle of refinement. Crystal and refinement data are given in Table 1.1.

Phase	**Formamide-I**	**Formamide-II**	**Formamide-IV**
Pressure (GPa)	**0.2**	**0.36**	**0.43**
Crystal Data			
Chemical formula	$CHONH_2$	$CHONH_2$	$CHONH_2$
M_r	45.04	45.04	45.04
Cell setting, space group	Monoclinic, $P2_1/n$	Othorhombic, $Pna2_1$	Monoclinic, $P2_1/n$
a, b, c (Å)	3.6812(4), 9.2666(9), 6.7968(16)	9.4564(11), 3.6639(7), 6.4268(18)	3.5851(2), 18.815(2), 6.2739(7)
α, β, γ (°)	90, 99.448(17), 90	90, 90, 90	90, 93.646(7), 90
V (Å^3)	228.71(6)	222.67(8)	422.35(7)
Z	4	4	8
D_{calc} (g cm^{-3})	1.308	1.343	1.402
Radiation type	Mo Kα	Mo Kα	Mo Kα
Temperature (K)	293	293	293
μ (mm^{-1})	0.12	0.12	0.12
Crystal form, colour	Block, colourless	Block, colourless	Block, colourless
Crystal Size (mm)	0.40 x 0.40 x 0.17	0.20 x 0.20 x 0.10	0.40 x 0.40 x 0.17
Data Collection			
Diffractometer	Bruker SMART	Bruker SMART	Bruker SMART
Data collection method	ω	ω	ω
Absorption correction	Empirical (SHADE) and multiscan (SADABS)	Empirical (using intensity measurements) and multiscan (based on symmetry-related measurements)	Multiscan (based on symmetry-related measurements)
T_{min} / T_{max}	0.546, 1.000	0.375, 1.000	0.95, 0.98
Number of measured, independent and observed reflections	720, 165, 119	460, 113, 88	3427, 445, 327
Criterion for observed reflections	$I > 2.0\sigma(I)$	$I > 2.0\sigma(I)$	$I > 2.0\sigma(I)$
R_{int}	0.025	0.046	0.061
θ_{max} (°)	26.5	23.2	26.3
Refinement			
$R[F^2 > 2\sigma(F^2)]$, $wR(F^2)$, S	0.052, 0.150, 1.10	0.135, 0.329, 1.10	0.066, 0.132, 1.17
Number of reflections	158	112	439
Number of parameters	28	11	56
H-atom treatment	Not refined	Not refined	Not refined
Weighting scheme P(i)*	0.0828, 0.0675, 0.00, 0.00, 0.00, 0.333	0.127, 1.88, 0.00, 0.00, 0.00, 0.333	0.0166, 0.745, 0.00, 0.00, 0.00, 0.333
$\Delta\rho_{max}$, $\Delta\rho_{min}$ (e Å^{-3})	0.08, -0.12	0.38, -0.33	0.18, -0.21
Extinction coefficient	-	-	81(17)†

* where p=P(6)*max(F_o^2,0) + (1-P(6))F_c^2
W = 1. / [σ^2 (F*) + (P(1)p)^2 + P(2)p + P(4) + P(5)Sinθ] SHELXL97 (Sheldrick, 1997)
† Extinction method: (Larson, 1970)

Table 4.1 Crystal and refinement data for X-ray single crystal structures.

4.2.2 Neutron powder diffraction

High pressure neutron powder diffraction data were collected *via* the time-of-flight technique using the PEARL beamline high pressure facility (HiPr) at ISIS. Formamide-d_3 (CDN isotopes, used as received) was contained in a null-scattering Ti-Zr alloy capsule gasket (Marshall & Francis, 2002) and loaded into a Paris-Edinburgh cell. The sample was loaded with powdered silica wool as previous work has shown it to aid formation of a good powder when crystallising liquids *in situ*. A small pellet of lead was also loaded as a pressure marker. The pressure was calculated from the refined lead cell parameter using a Birch-Murnaghan equation of state (Birch, 1947) with V_o = 30.3128 Å^3, B_o = 41.92 GPa, B' = 5.72. These parameters were derived by Fortes (2004) as averages of the values determined in three earlier studies (Kuznetsov *et al.*, 2002; Miller & Schuele, 1969; Waldorf & Alers, 1962).

Initial loading

Upon application of pressure formamide crystallised at 0.54 GPa in phase IV, which is one of the phases identified in the single crystal study. The pressure was increased in small steps from 0.54 GPa to a final pressure of 3.6 GPa. On increasing the pressure from 1.3 GPa to 1.83 GPa the sample underwent a phase transition to a previously unobserved phase, which we have designated phase V. No further phase transitions were observed on increasing the pressure. By 3.6 GPa strain induced peak broadening was quite pronounced and the sample was decompressed. During the decompression the sample transformed back to phase IV at 1.15 GPa and then to phase II at 0.13 GPa. Further decompression resulted in the sample melting.

Recompressing the sample from 0.08 GPa to 0.32 GPa resulted in a transition from phase II to another previously uncharacterised phase which we have designated phase III. Further increasing the pressure resulted in transitions to phase IV at 0.66 GPa and then to phase V at 1.72 GPa. The order in which the phase transitions were observed is summarised in Figure 4.1.

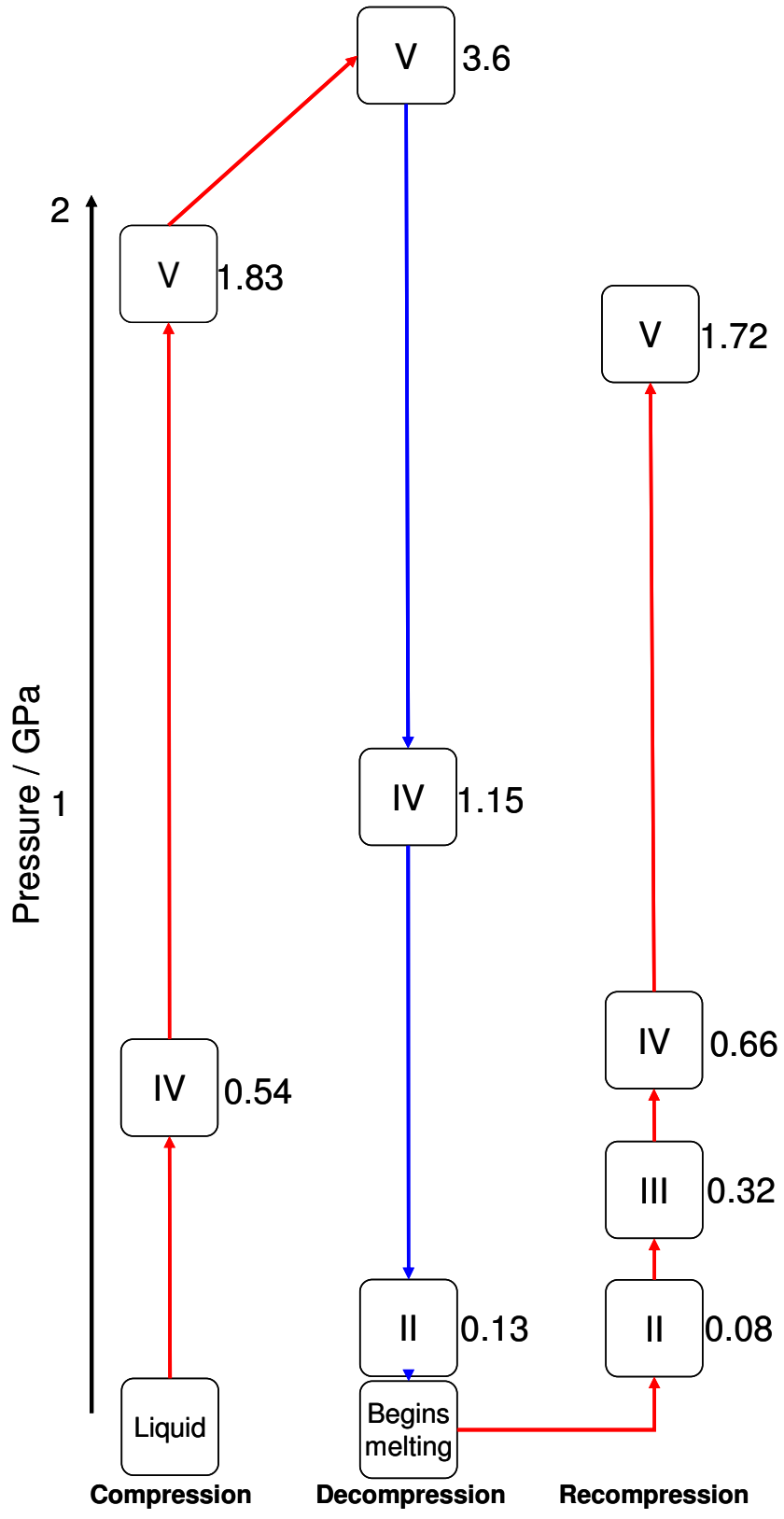

Figure 4.1 Sequence of phase transitions observed in initial neutron powder diffraction loading.

Pure loading

In order to obtain high quality diffraction patterns of the new phases uncontaminated by lead peaks for indexing and structure solution and to achieve controlled formation of each of the phases in turn a second sample was loaded into the Paris-Edinburgh cell without the lead pressure marker. The load on the pressure cell is measured in tns and converted to GPa on the basis of the cell volume of the formamide (see below).

The sample initially crystallised in phase IV at a load of 16 tns (0.78 GPa) before transforming to phase V on increasing the load to 23 tns (1.35 GPa). While decompressing from 29 tns (2.26 GPa) the sample transformed down through all the high pressure phases; V→IV at a load of 3 tns, IV→III at 1.2 tns, III→II at 0.6 tns. Formamide-I was not observed in any of the neutron powder investigations.

In order to obtain the pressures quoted for the final structures in the absence of a pressure calibrant, the data collected earlier in the experiment with the lead calibrant present were used to plot the unit cell volume as a function of the pressure for each phase. For phases IV and V, a second order polynomial fit was calculated which was then used to obtain the pressure from the unit cell volume. As phases II and III only exist over a very narrow pressure range there were insufficient data to perform a polynomial fit and so the pressures can only be estimated. For phase III a straight line fit was calculated for 3 data points as the unit cell volume was within the range previously collected with a pressure calibrant. The pressure has been estimated based on this fit. For phase II the unit cell volume was outside the range previously collected with a pressure calibrant, thus it is only possible to estimate a pressure range.

Structure solution and refinement

Indexing of the two new phases was carried out using a combination of DICVOL91 (Boultif & Louer, 1994) and TOPAS-Academic (Coelho, 2007). The structures were solved using simulated annealing within TOPAS-Academic, with Rietveld refinements also performed using TOPAS-Academic. During refinement the

formamide molecules were treated as planar rigid groups. Bond lengths and angles were taken from X-ray single crystal data, with deuterium distances set to those obtained from an MP2/631G** geometry optimisation in the gas phase (N-H 1.009 Å, C-H 1.050 Å). Bond lengths, angles and torsion angles were not refined. All non-hydrogen atoms were refined with a common isotropic displacement parameter, as were all deuterium atoms. As the sample was crystallised *in situ* a second order spherical harmonic preferred orientation correction was included. Ni and WC phases were also included in the refinement. The presence of these is due to the anvils of the Paris-Edinburgh cell. Rietveld refinement profiles are shown in Figure 4.2 with crystal and refinement data given in Table 4.2.

4.2.3 PIXEL calculations

The final crystal structures obtained from the neutron data were used to calculate the molecular electron density for each phase. The 0.2 GPa single crystal structure was used for the Formamide-I calculation. Standard quantum mechanical methods using GAUSSIAN03 (Frisch *et al.*, 2004) at the MP2/6-31G** level of theory were used. H-atom distances for phase I were set to those used in the neutron refinements. Lattice energy calculations were performed using PIXEL (Gavezzotti, 2005b; Gavezzotti, 2005a), part of the OPiX package (Gavezzotti, 2003), using a cluster of molecules of radius 12 Å. These calculations yielded a total lattice energy and a breakdown into the electrostatic, polarization, dispersion and repulsion components.

4.2.4 Hirshfeld Surface Calculations

Hirshfeld surfaces were calculated and analysed using the program CrystalExplorer (Wolff *et al.*, 2005). All the Hirshfeld surfaces were generated using a standard (high) surface resolution and mapped with d_e using a fixed colour scale of 0.79 (red) to 2.1 Å (blue). The fingerprint plots generated from the Hirshfeld surfaces use a standard 0.4-2.6 Å view.

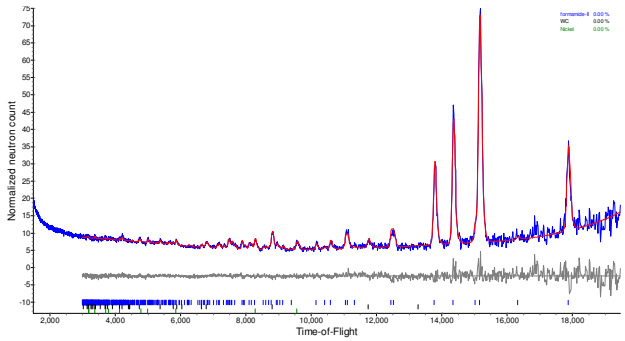

(a) Formamide-II

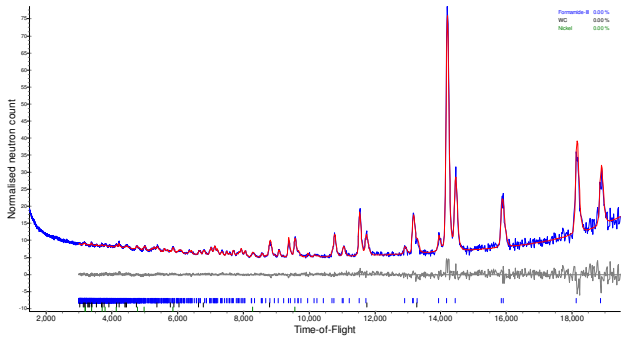

(b) Formamide-III

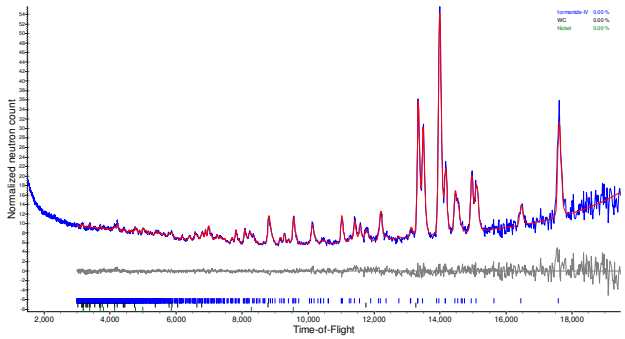

(c) Formamide-IV

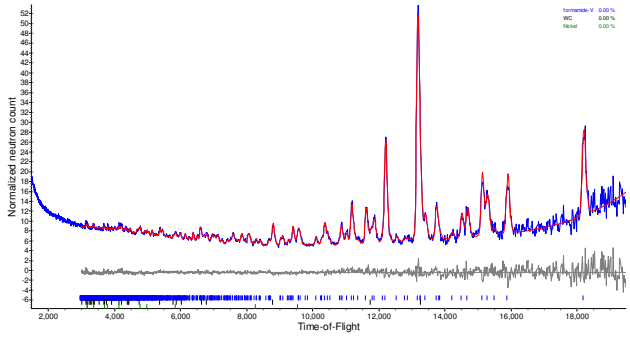

(d) Formamide-V

Figure 4.2 Rietveld refinement plots for high pressure studies of formamide. Blue and red lines correspond to observed and calculated data respectively. The difference is shown in grey.

Phase	**Formamide-II**	**Formamide-III**	**Formamide-IV**	**Formamide-V**
Pressure (GPa)	0.2	0.35	0.78	1.81
Crystal Data				
Chemical formula	$CDOND_2$	$CDOND_2$	$CDOND_2$	$CDOND_2$
M_r	48.05	48.05	48.05	48.05
Cell setting, space group	Othorhombic, $Pna2_1$	Monoclinic, $P2_1/a$	Monoclinic, $P2_1/n$	Monoclinic, $P2_1/a$
a, b, c (Å)	9.498(2), 3.7506(3), 6.419(1)	6.9393(4), 6.7991(7), 5.3019(4)	3.5851(2), 18.815(2), 6.2739(7)	12.665(1), 3.4694(2), 10.1898(9)
α, β, γ (°)	90, 90, 90	90, 117.146(6), 90	90, 93.646(7), 90	90, 119.742(7), 90
V ($Å^3$)	228.68(7)	222.59(3)	422.35(7)	388.75(7)
Z	4	4	8	8
D_{calc} (g cm^{-3})	1.396	1.434	1.511	1.642
Radiation type	Neutron	Neutron	Neutron	Neutron
Temperature (K)	298	298	298	298
Specimen form	Powder	Powder	Powder	Powder
Data Collection				
Diffractometer	PEARL, ISIS	PEARL, ISIS	PEARL, ISIS	PEARL, ISIS
Collection method	Time of flight	Time of flight	Time of flight	Time of flight
Range of *d* (Å)	0.64 – 4.14	0.64 – 4.14	0.64 – 4.14	0.64 – 4.14
Refinement				
Method	Rietveld	Rietveld	Rietveld	Rietveld
R_p	5.892	4.117	3.912	3.986
R_{wp}	4.965	3.377	3.126	3.181
S	1.215	1.269	1.245	1.272
Background	6 term Chebychev polynomial	6 term Chebychev polynomial	6 term Chebychev polynomial	6 term Chebychev polynomial
Profile function	Back-to-back exponential convoluted with Voigt function	Back-to-back exponential convoluted with Voigt function	Back-to-back exponential convoluted with Voigt function	Back-to-back exponential convoluted with Voigt function
Number of parameters	28	31	37	37
Weighting scheme	$1/\sigma^2$	$1/\sigma^2$	$1/\sigma^2$	$1/\sigma^2$

Table 4.2 Crystal data and refinement parameters for neutron powder structures.

4.3 Results

High pressure neutron powder diffraction experiments have shown formamide forms four high pressure phases which we have designated phases II to V in order of increasing pressure. Formamide-I has previously been reported at low temperature (Ladell & Post, 1954) and was not observed in the neutron powder study. Transformation through all the phases in sequence from phase V down to phase II was observed when decompressing a pure sample from 2.26 GPa. Decreasing the pressure further resulted in the sample melting.

Complementary to the neutron study, single crystals of phases II and IV were obtained when crystallised in a diamond anvil cell at 0.3 and 0.4 GPa respectively. A single crystal of phase I was also obtained when crystallised at 0.2 GPa in a diamond-anvil cell.

4.3.1 Formamide-I

The structure of formamide-I at low temperatures has previously been characterised by X-ray single crystal (Ladell & Post, 1954) and neutron powder diffraction (Torrie & Brown, 1994). A single crystal of Formamide-I was obtained when crystallised in a diamond-anvil cell at 0.2 GPa. The structure consists of N1-H2...O1 hydrogen bonded chains (N...O 2.901(6) Å), Figure 4.3a, of formamide molecules parallel to the *b* axis. The molecules alternate in orientation within the chain with successive molecules being related by the 2_1 screw axis. N1-H3...O1 hydrogen bonds (N...O 2.949(11) Å) link the chains to form layers parallel to the (101) plane, Figure 1.4. This creates dimer units across inversion centres forming $R_2^2(8)$ rings. There are no N-H…O interactions between the layers. The lengths of the hydrogen bonds are not significantly different under these conditions to those at low temperature as shown in Table 4.3.

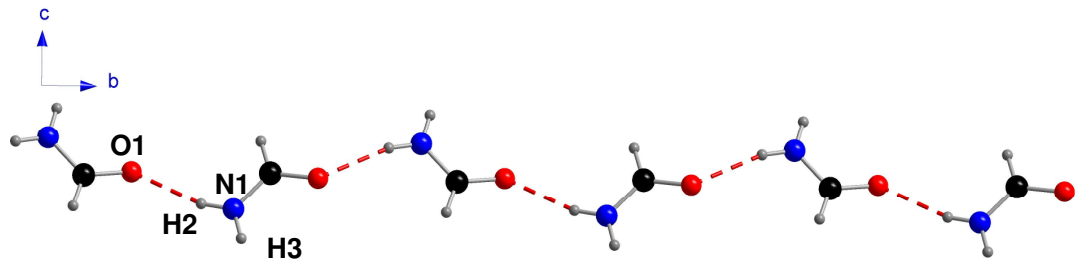

(a) Formamide-I

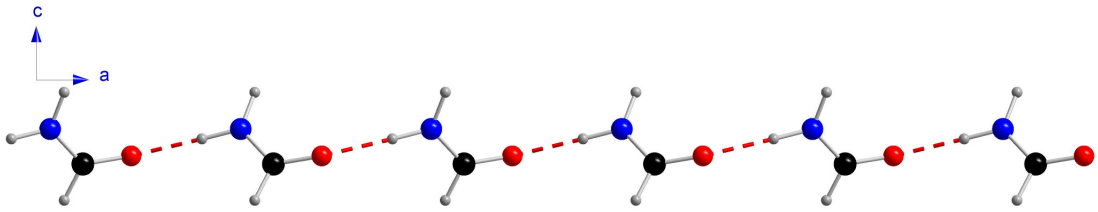

(b) Formamide-II

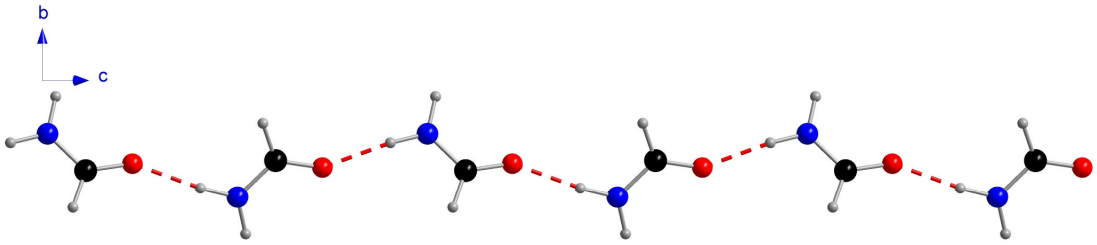

(c) Formamide-III

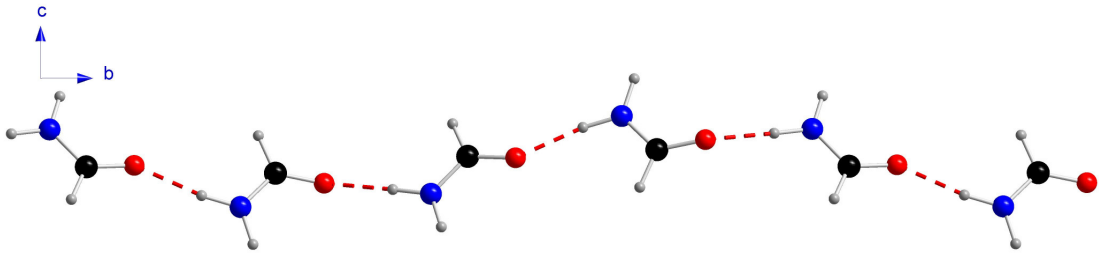

(d) Formamide-IV

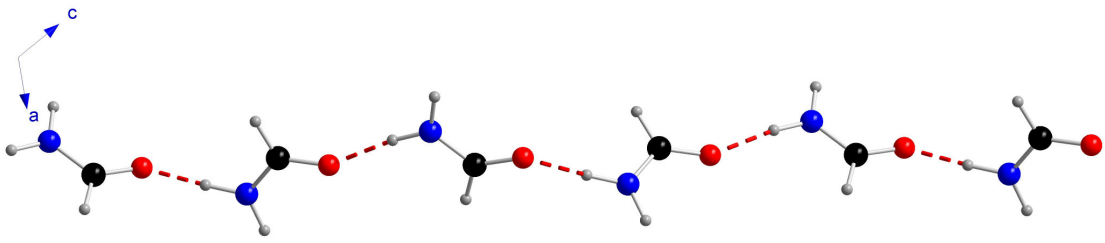

(e) Formamide-V

Figure 4.3 N1-H2…O1 hydrogen bonded chains.

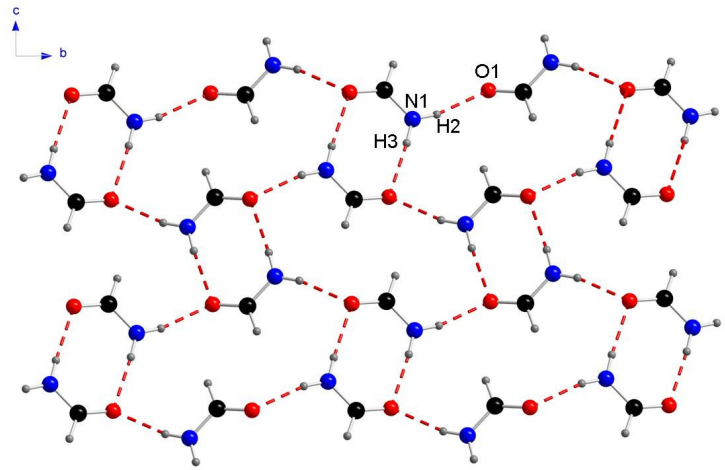

(a) N1-H2…O1 hydrogen bonded chains linked into layers by N1-H3…O1 hydrogen bonds.

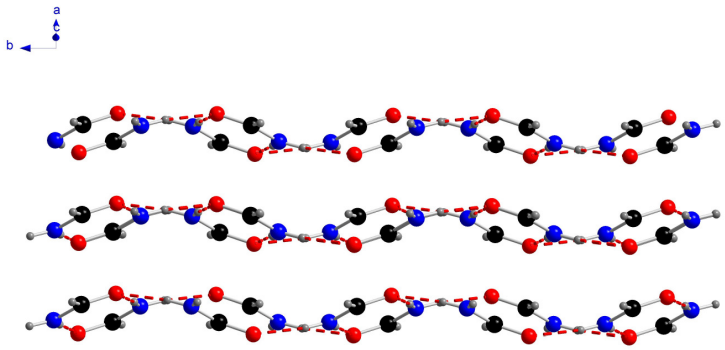

(b) No N-H…O hydrogen bonds between layers

Figure 4.4 Crystal structure of Formamide-I.

Phase	I (90 K)	I	II	III	IV	V
Along chain N1-H2…O1 N…O	*2.883*	*2.901(6)*	2.900(17)	2.818(3)	2.821(10) 2.91(2) *2.859(5)* *2.913(5)*	2.837(12) 2.893(8)
Between chains N1-H3…O1 N…O	*2.948**	*2.949(11)* *	2.886(16)	3.019(12) *	2.965(12) 2.98(3)* *2.948(6)* *2.959(6)**	2.933(18) * 2.947(18) *

* dimer interactions

Table 4.3 Hydrogen bond lengths for each phase of formamide. All distances are in Å. Data in *italics* are from X-ray single crystal data.

PIXEL calculations show the strongest interaction is the hydrogen bonded $R_2^2(8)$ dimer unit (-31.6 kJ mol^{-1}). This energy corresponds to an interaction involving two N-H...O hydrogen bonds and it is therefore twice the other hydrogen bond energies quoted here. The largest contribution to the energy is the Coulombic term as expected for hydrogen bonds. The second strongest interactions are the N1-H2...O1 hydrogen bonds to neighbouring molecules along the chain (-15.2 kJ mol^{-1} per interaction). There are two more interactions with energy values over 5 kJ mol^{-1}. These are Coulombic interactions between the reference molecule and molecules related by inversion and translation, in the layers above and below. The centroid-centroid distances between the layers are different (4.604 Å & 3.843 Å), resulting in different interaction energies (-8.7 & -6.5 kJ mol^{-1} respectively). The shorter centroid-centroid distance is less favourable due to less favourable polarisation and dispersion contributions; the differences in the Coulombic and repulsion terms cancel each other out. There are no N-H...O interactions between the layers. The shortest centroid-centroid distance that occurs, 3.681 Å, is repulsive. These repulsive interactions are between the reference molecule and molecules in the neighbouring layers related by translation along the *a*-axis only. The largest contribution to the energy is a repulsive Coulombic term due to like charge regions being placed above each other.

4.3.2 Formamide-II

Formamide-II is orthorhombic, space group $Pna2_1$ with one molecule in the asymmetric unit. As in formamide-I, the structure consists of N1-H2...O1 (N...O 2.900(17) Å) hydrogen bonded chains, Figure 4.3b, however the orientation of the molecules is different. In Formamide-I the molecules are rotated by 180° along the chain as they are related by the 2_1 screw axis, however in Formamide-II the molecules are related by the *a*-glide and in projection the chain appears to be formed by simple translation. This change in conformation within the chain results in the remaining hydrogen bond donor and acceptor functions (N-H & O lone pair) being on opposite sides of the chain. This differs from phase I, where the remaining donor and acceptor were on the same side of the chain in an arrangement suitable for $R_2^2(8)$ dimer formation. Consequently, in phase II dimer units cannot be formed; this is the

only phase without dimer interactions. The orientation of the molecules within the chain means the repeating unit along the chain is able to form N1-H3...O1 hydrogen bonds (N...O 2.886(16) Å) to four other chains forming a network structure rather than discrete layers, Figure 4.5b.

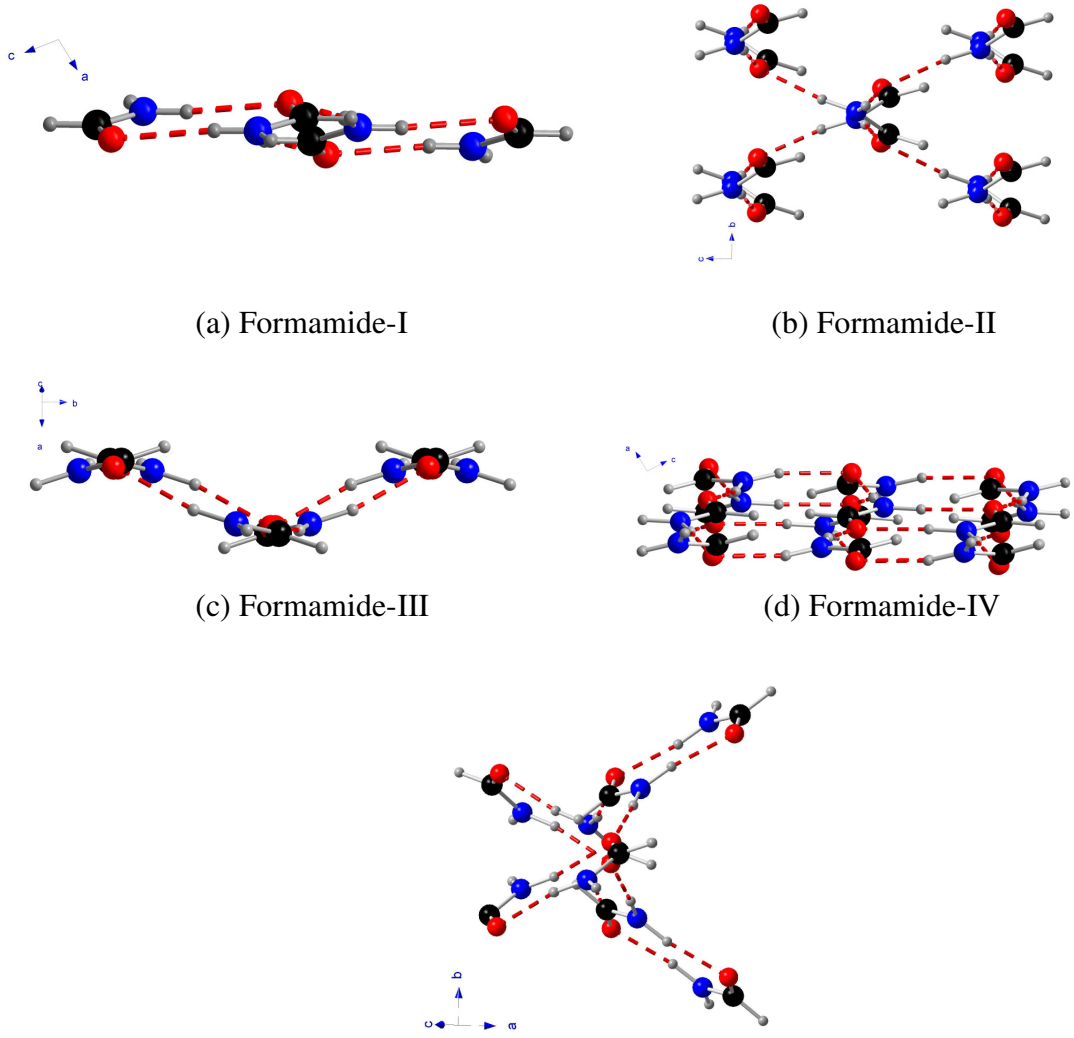

(a) Formamide-I (b) Formamide-II

(c) Formamide-III (d) Formamide-IV

(e) Formamide-V

Figure 4.5 Hydrogen bonding interactions linking chains viewed along the central chain.

PIXEL calculations show the hydrogen bonding interactions between the chains (-17.1 kJ mol^{-1}) are stronger than those along the chains (-13.4 kJ mol^{-1}). The only other interactions over 5 kJ mol^{-1} are Coulombic interactions with molecules related by the *n* glide plane. The largest overall repulsive interactions (2.7 kJ mol^{-1}) occur between the reference molecule and molecules simply translated along the *b*-axis as seen in Formamide-I, though the centroid-centroid distance is slightly shorter in Formamide-I (Formamide-I 3.681 Å, Formamide-II 3.751 Å). This closer contact results in the Coulombic term being more repulsive (+4.8 vs +4.2 kJ mol^{-1}), hence interaction is overall more repulsive.

4.3.3 Formamide-III

The structure of formamide-III is monoclinic, space group $P2_1/a$. The structure consists of N1-H2...O1 hydrogen bonded chains (N...O 2.818(3) Å) very similar to those in formamide-I, Figure 1.3. The way the chains are connected to form a layer is also very similar to formamide-I and the difference between the two structures is the CONC torsions angle along the chain. There is a difference of 17° in the torsion angle between the two phases and as a result the layers in formamide-III are more sinusoidal than those in formamide-I as shown in Figure 4.6.

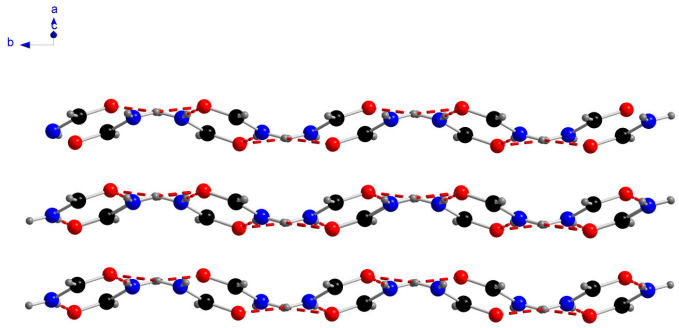

(a) Formamide-I

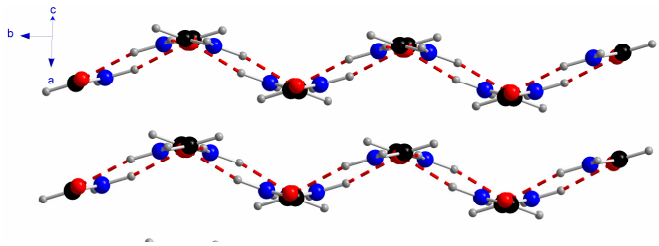

(b) Formamide-III

Figure 4.6 Sinusoidal hydrogen bonded layers.

PIXEL calculations show the dimer interactions are the strongest interactions in the structure (-29 kJ mol^{-1}). The hydrogen bonding interactions along the chains are the next strongest interactions at -15.3 kJ mol^{-1}. There are three other interactions each over 5 kJ mol^{-1}. Two of these involve molecules related by the 2_1 screw axis and translation in a neighbouring layer (-8 kJ mol^{-1} each). The third (-6.9 kJ mol^{-1}) is to a molecule in the same layer as the reference molecule being related by inversion and then translated along the *b*-axis relative to the molecule involved in the dimer interaction. The largest overall repulsive interactions (+2.9 kJ mol^{-1}) are with molecules translated along the *c*-axis from those hydrogen bonded along the chain to the reference molecule.

4.3.4 Formamide-IV

The structure of formamide-IV is closely related to the low temperature structure, formamide-I, as can been seen from the unit cell dimensions, Table 4.1. Both the *a* and *c* axes are very similar in the two phases, however in the higher pressure phase the *b* axis is approximately doubled. This doubling of the *b*-axis can be explained by examination of the hydrogen bonded chain. The structure of formamide-IV contains two molecules in the asymmetric unit and as such has a repeat unit of four molecules along the chain compared to only two in formamide-I. The two independent molecules alternate along the chain with the pairs related by the 2_1 screw axis. Comparing the new chain to the chains in phase I, Figure 4.3, it can be seen that the first two molecules have similar orientations, but the next two are rotated by 180° about the *b*-axis. Moving along, the next two molecules are the same in both chains, thus the repeat unit is twice the length. This change in orientation results in two unique hydrogen bonds along the chain (N...O 2.821(10) & 2.91(2) Å) and a different hydrogen bonding pattern within the layer, Figure 4.7. In phase I the chains are hydrogen bonded together such that all the molecules form dimer interactions producing two hydrogen bonding motifs within the layer. The orientation of the molecules in formamide-IV means that only one of the symmetry independent molecules forms dimer units across inversion centres, resulting in three distinct hydrogen bonding motifs (labelled $R_2^2(8)$, $R_4^3(12)$ & $R_6^4(16)$ in Figure 4.7) within the

layers and two unique hydrogen bonds between chains (N...O 2.98(3) (dimer) & 2.965(12) Å).

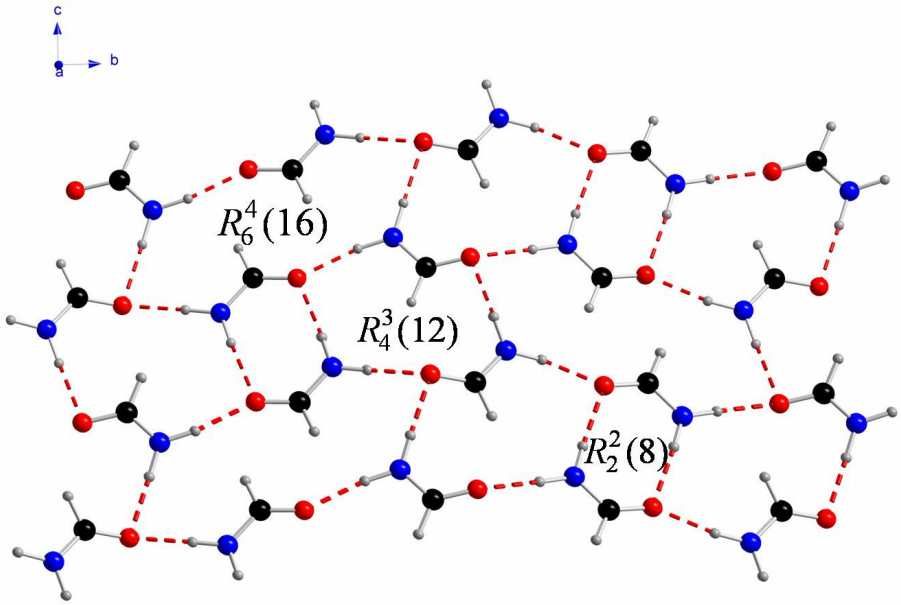

Figure 4.7 Hydrogen bonded layer formed in Formamide-IV.

As anticipated, PIXEL calculations show the hydrogen bonded dimer interactions between chains to be the strongest interaction (-29 kJ mol^{-1}). The next strongest interactions (-17.2 kJ mol^{-1}) are the non-dimer hydrogen bonds between chains. The longer hydrogen bonds along the chains are weaker (-13.7 & -12.9 kJ mol^{-1}). The repulsion term is smaller for the longer hydrogen bond, however the Coulombic, dispersion and polarisation terms all becomes less favourable and together outweigh the improvement in the repulsion. In all these interactions the Coulombic term is largest as expected for hydrogen bonds, indeed all of the interactions greater than 5 kJ mol^{-1} are dominated by the Coulombic term. The remainder of the interactions over 5 kJ mol^{-1} are between the reference molecule and molecules in neighbouring layers. The molecules concerned are those related by translation along the *a*-axis to the molecules hydrogen bonding to the reference molecules in neighbouring chains.

4.3.5 Formamide-V

The structure of Formamide-V is monoclinic, space group $P2_1/a$, with two independent molecules in the asymmetric unit. The two independent molecules alternate along N1-H2...O1 hydrogen bonded chains (N...O 2.837(12) & 2.893(8) Å) parallel to (101), with the pairs related by the glide plane. Each molecule forms two N1-H3...O1 hydrogen bonds (N...O molecule one 2.933(18) & molecule two 2.947(18) Å) to a single molecule in a neighbouring chain, producing dimer units across inversion centres. The orientation of the molecules along the chains means that the repeating unit along the chain is able to form these interactions with four neighbouring chains to produce a hydrogen bonded network, Figure 4.5.

The strongest interactions, according to PIXEL calculations, are the dimer interactions across inversion centres (-28.6 & -28.1 kJ mol^{-1}). The next strongest interactions are the hydrogen bonds along the chain (-14.2 & -11.8 kJ mol^{-1}). In all of these cases the Coulombic term is largest.

4.4 Discussion

4.4.1 H-bonding

The structural feature common to all five structures is the N-H...O hydrogen bonded chain. Further N-H...O hydrogen bonds link the chains to form either layered or network structures depending on the orientation of the molecules in the chain.

In order to compare the various chains exhibited we need to classify the hydrogen bonding patterns along the chains. All of the chains consist of N1-H2…O hydrogen bonds however there are two possible hydrogen bonding combinations along the chain; one involving each of the oxygen lone pairs, Figure 4.8. Figure 4.8a on the left is described as having a *cis* arrangement of hydrogen bonds along the chain as the two hydrogen bonds along the chain are on the same side of the molecule and the remaining hydrogen bond donor and acceptors are on the other side of the molecule. It is this *cis* arrangement which results in the formation of $R_2^2(8)$ dimer interactions. Figure 4.8b on the right shows a *trans* arrangement along the chain. The remaining

hydrogen bond donor and acceptor are on opposite sides of the molecule, thus dimer interactions cannot be formed.

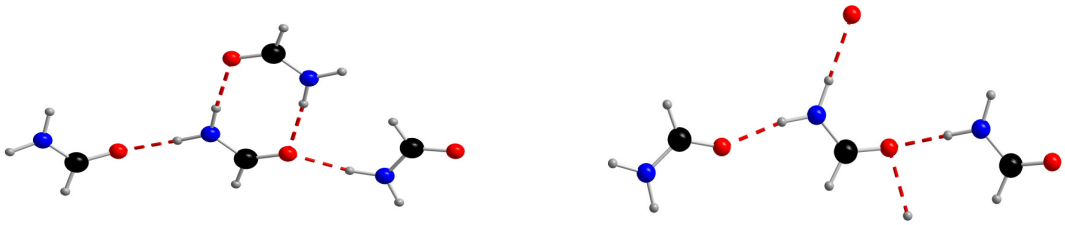

(a) *cis* (b) *trans*

Figure 4.8. Classification of hydrogen bonding patterns along the chains.

Using this *cis*/*trans* classification we see that there are three different chain patterns exhibited; all *cis*, all *trans*, alternating *cis*/*trans*.

The only chain which is observed in multiple structures is the all *cis* chain. Formamide-I,-III & -V all contain this chain, though in formamide-V the chain consists of two independent molecules. The result of hydrogen bonding between these chains is a structure in which all the molecules are involved in dimer interactions. The difference between the chains in the three structures is in the angle formed between the molecules along the chain, highlighted by viewing the chains end–on, Figure 4.5. This can be considered in terms of the CONC torsion angle along the hydrogen bonds, Table 4.4. Formamide-I & III are both layered structures with sinusoidal topology. The difference between them is in the CONC torsion angle which produces more sinusoidal layers in formamide-III. In contrast, formamide-V is a network structure. In this case, the chain consists of two independent molecules which alternate along the chain resulting in two different torsion angles along the chain. The pair of independent molecules forms an almost planar pair, rotated by 180° relative to each other. This results in hydrogen bonding interactions with two other chains in a layer type arrangement. The relationship between the pairs of independent molecules along the chain results in a torsion angle of approximately 90°, thus the next two molecules are able to hydrogen bond to a further two different

chains. Overall, the four molecule repeat unit is thus able to interact with four surrounding chains producing a hydrogen bonded network structure instead of layers.

Phase	I	II	III	IV	V
CONC	142.8(7)°	81.3(3)°	159.1(2)°	108.9(3)° 167.2(3)°	93.4(1)° 179.8(2)°

Table 4.4. CONC torsion angles formed along the hydrogen bonded chains.

Formamide-II consists of an all *trans* chain which is unique to that structure. As discussed above, a *trans* arrangement of hydrogen bonds along the chain prevents the formation of dimers as the remaining hydrogen bonding functions are on opposite sides of the molecule. This is the only structure which does not contain any dimer interactions. The CONC torsion angle along the chain is approximately 80°, consequently the two molecule repeating unit along the chain is able to hydrogen bond to four surrounding chains producing a network structure.

The third type of chain formed is seen in Formamide-IV. There are two independent molecules in the asymmetric unit, which alternate along the chain. In this case we have a combination of the above two chains with alternating *cis*/*trans* hydrogen bonding interactions along the chain. Consequently only half of the molecules form dimers. Looking along the chains, Figure 4.5, at the orientation of the remaining hydrogen bonds we can understand the formation of a layered structure. The two independent molecules give rise to two different CONC torsion angles along the chain. The molecules form almost planar pairs (166°) with a 108° torsion angle between them. This gives rise to sinusoidal layers similar to those seen in formamide-I & III.

Table 4.3 shows the lengths of the hydrogen bonds in the various structures. The hydrogen bonded dimer interactions between the chains are slightly longer than non-dimer interactions between chains. The largest variation between the longest and shortest hydrogen bonds within one structure is in phase III (0.201 Å) which also exhibits the longest N...O hydrogen bonding distance (3.019(12) Å). The smallest variation is in phase II, which is the only structure with no dimer interactions.

4.4.2 PIXEL Analysis

PIXEL calculations, Table 4.5, show that in general the total lattice energy, U, becomes more positive as the pressure is increased due to increased repulsion between molecules, however phase II is less stable than both phase I and phase III.

Formamide-I and III are comparable in energy which is to be expected as they are structurally very similar. The formation of phase II between them is something of a mystery. Phase I and phase II were both obtained at 0.2 GPa and have the same unit cell volume at this pressure, within error, and therefore the formation of phase II cannot be ascribed to the PV term contributing to the lattice enthalpy, $H = U + PV$. This leaves kinetic and entropic factors to be considered as the driving force for the formation of this phase. Phase II has been formed both from the liquid and from phase III by reducing the pressure when phase I would be expected as it is structurally very similar to phase III. This indicates that kinetic factors are not responsible and the formation of phase II is likely to be entropically driven.

	Coulombic	Dispersion	Repulsion	Polarisation	U
Formamide-I	-80.6	-34.5	68.2	-26.3	-73.4
Formamide-II	-79.3	-35.4	78.8	-28.6	-64.4
Formamide-III	-79.5	-37.5	74.5	-29.8	-72.3
Formamide-IV	-79.1	-40.8	80.2	-27.2	-66.9
Formamide-V	-86.6	-48.1	99.9	-29.9	-64.7

Table 4.5. Components of the lattice energy and the total lattice energy, U, for each phase of formamide. Energies are per molecule in kJ mol^{-1}.

The $R_2^2(8)$ dimer interactions, Table 4.6, are the strongest molecule-molecule interactions as they involve two identical hydrogen bonds. Dividing these energies by two gives an indication of the energy for each hydrogen bond. Taking this into account, the non dimer hydrogen bonds linking chains are stronger than those involved in the dimers though overall there is little variation in the hydrogen bond energies.

Phase	I	II	III	IV	V
Along chain	-15.2	-13.3	-15.3	-13.7 -12.9	-14.2 -11.8
Between Chains					
Dimer	-31.6	-	-29	-29	-28.6 -28.1
Non-dimer	-	-17.1	-	-17.2	-

Table 4.6. Total intermolecular energies for the hydrogen bonding interactions in each phase of formamide. All energies are in kJ mol^{-1}.

As discussed in the previous section, we observe both *cis* and *trans* hydrogen bonding arrangements along the chain and variations in the CONC torsion angle along the chains gives rise to a mixture of layered and network structures. Calculating the energy for the various possible N1H2…O1 hydrogen bonding combinations for a pair of formamide molecules highlights this flexibility.

Figure 4.9a shows the interaction energy for a planar N1H2…O1 hydrogen bonded pair as a function of COH angle. This corresponds to moving from a *cis* (120°) to a *trans* (240°) hydrogen bonding arrangement. This interaction is extremely flexible with orientations between 100° and 240° within only 4 kJ mol^{-1} of each other, except for a linear (180°) orientation. A linear arrangement is expected to be highest in energy within this range as it corresponds to an interaction directly between the two lone pairs. Changing from a *cis* to a *trans* hydrogen bonding arrangement would be necessary in some of the phase transitions, for example transforming to and from phase IV, however these calculations reveal that the barrier is low and so there would be no significant energy penalty associated with the rearrangement.

Similar calculations were performed to investigate the effect of the torsion angle for both *cis* and *trans* arrangements, Figure 4.9b. The *cis* arrangement is extremely flexible with all orientations within only 1.7 kJ mol^{-1}, thus there is no significant energy penalty associated with the molecules rotating within the chain and we observe a *cis* arrangement most frequently. This means that it is relatively easy to move from a layered to a network structure by varying the torsion angle. The *trans* arrangement shows a larger variation in energy and would therefore be less flexible.

We only observe this arrangement in two phases and as expected the torsion angles observed are close to the bottom of the well (Figure 4.9b).

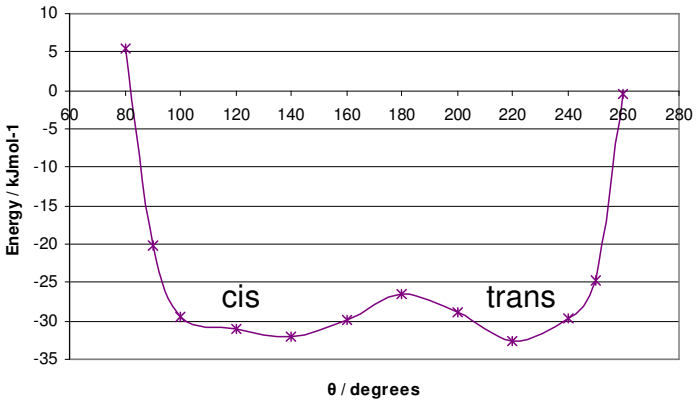

(a) Interaction energy as a function of COH angle

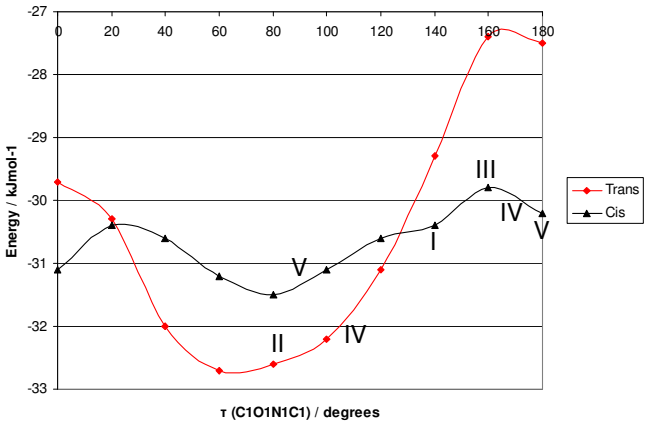

(b) Interaction energy as a function of CONC torsion angle

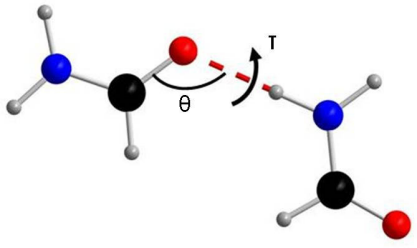

Figure 4.9 Interaction energy for N1-H2…O hydrogen bonded dimers.

These calculations highlight the flexibility exhibited by the hydrogen bonded chains in formamide. Within the five phases, we see a combination of *cis* and *trans* hydrogen bonding arrangements along the chains however Figure 4.9a highlights that there is a very small barrier to switching to between *cis* and *trans* which is necessary to transform between phases. The torsion angle calculations show that the *cis* chain is more flexible with almost no barrier to rotation of the molecules within the chains to switch between layered and network structures.

The energies for the dimer units obtained from PIXEL calculations are comparable to the energy obtained for a cyclic formamide dimer by *ab initio* and density functional theory calculations (Cabaleiro-Lago & Otero, 2002). Formamide dimers have been the subject of much theoretical study. The most stable formamide dimer is a cyclic structure of C_{2h} symmetry involving two equivalent N-H...O hydrogen bonds similar to those observed in the crystal structures. Optimisation of the dimer using the DFT/B3LYP and MP2 computational methods gave interaction energies of -60.10 and -60.34 kJ mol^{-1} respectively. These values are per mole of dimers and as such need to be divided by two to be compared to our PIXEL values which are per mole of molecules. Taking this into account, our values are in good agreement, especially considering the PIXEL calculations are for actual dimer units observed in the crystal structures rather than optimised interactions.

4.4.3 Hirshfeld surfaces

Whilst the Hirshfeld surface allows all intermolecular contacts in a structure to be analysed simultaneously it can be difficult to compare structures as the surface is 3-D. The fingerprint plot condenses the distance information in the surface plot into a 2-D graph allowing easy comparison of structures. Analysis of the fingerprint plot gives a quick overview of all the intermolecular interactions without focussing on any one specific interaction. As such, they can be useful in assessing the validity of crystal structures, particularly those solved from powder data.

Figure 1.10 shows the fingerprint plots for all five phases of formamide. It is immediately evident that they are all very similar with no striking differences

between the plots. The same features are present in all the plots with interaction distances covering approximately the same range in all the structures. As such, the structures solved from powder data make sense in relation to those solved from single crystal studies.

The main feature of the plots is the hydrogen bonding interactions which occur as a pair of spikes either side if the $d_i = d_e$ diagonal. It is of interest to note that there is no significant shortening of these interactions upon increasing the pressure.

Although the hydrogen bonding interactions do not compress significantly, the main body of the plots do compress and move closer to the origin as the pressure increases. In particular, the longer contacts compress as the pressure increases, reducing the spread of intermolecular contact distances observed at high pressure.

The area in between the hydrogen bonding spikes is associated with H…H contacts. The skirt region is due to H…H contacts within dimer units. As the pressure increases we see these contacts compress and the characteristic H…H interaction 'nose' becoming prominent.

As is typical, the plots for the structures with one molecule in the asymmetric unit are more symmetric than those for the $Z' > 1$ structures.

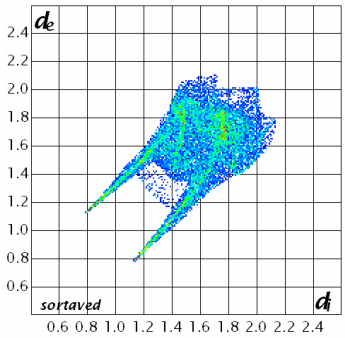

(a) Formamide-I

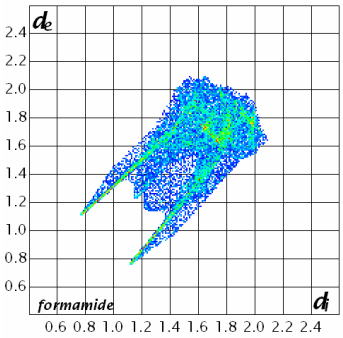

(b) Formamide-II

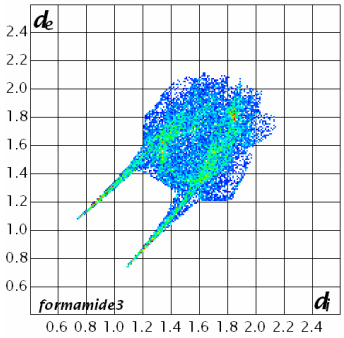

(c) Formamide-III

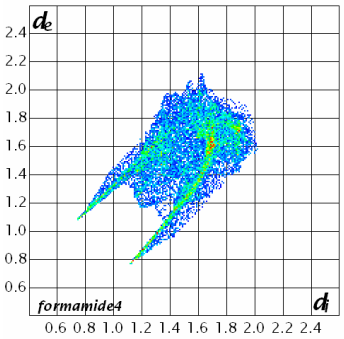

(d) Formamide-IV molecule 1

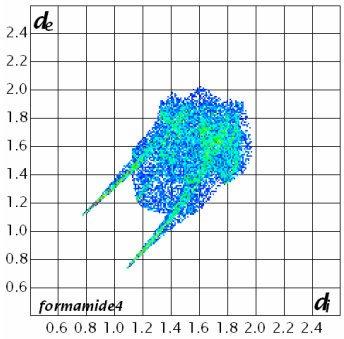

molecule 2

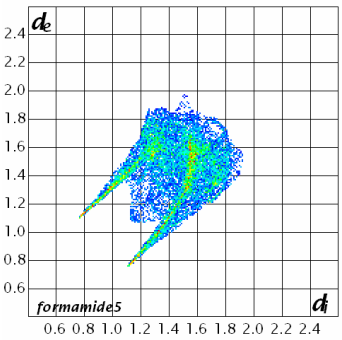

(e) Formamide-V molecule 1

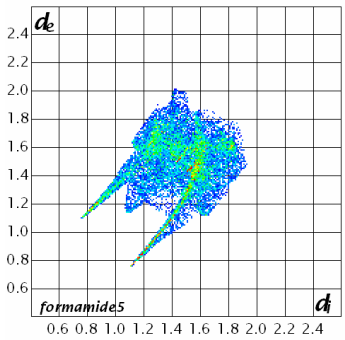

molecule 2

Figure 4.10 Fingerprint plots for all phases of formamide.

4.5 Conclusions

The effect of pressure on the crystal structure of formamide has been studied by a combination of X-ray single crystal and neutron powder diffraction. In contrast to its behaviour under conditions of varying temperature, formamide forms four new polymorphs when subjected to pressure of 0.3-3 GPa.

All of the structures are characterised by the formation of N1-H2…O1 hydrogen bonded chains with three different hydrogen bonding patterns along the chains exhibited. These hydrogen bonding patterns have been classified using a *cis*/*trans* notation. N1-H3…O1 hydrogen bonds form between the chains resulting in the formation of both layered and network structures. The orientation of the molecules within the chain determines whether the resultant structure is layered or a hydrogen bonded network.

PIXEL analysis shows that the total lattice energy becomes more positive as the pressure is increased due to the increase in repulsion between molecules. Formamide-II is unstable compared to phases I and III even when considering the lattice enthalpy, thus the formation of phase II must be entropically driven. The dominant interactions between the molecules are the hydrogen bonds though there is little variation in the hydrogen bond energies across the phases even comparing the hydrogen bonds along the chains and between the chains. The strongest interactions are the dimer interactions as they consist of two identical hydrogen bonds. The dimer energies obtained from the PIXEL calculations are comparable to those for optimised cyclic formamide dimers from *ab initio* and DFT calculations.

Analysis of the fingerprint plots calculated from Hirshfeld surfaces shows that there are no striking differences between the various structures and that the same features are present in all the plots, thus the structures make sense as a series. It is notable that there is no significant compression of the hydrogen bonds as the pressure increases though the main body of the plots do compress.

4.6 References

Birch, F. (1947). *Physical Review* **71**, 809-824.

Blessing, R. H. (1995). *Acta Crystallographica, Section A* **51**, 33-38.

Boultif, A. & Louer, D. (1994). *J. Appl. Crystallogr.* **24**, 987-993.

Bruker-Nonius (2006). *SAINT version 7.*

Cabaleiro-Lago, E. M. & Otero, J. R. (2002). *J. Chem. Phys.* **117**, 1621-1632.

Coelho, A. (2007). *TOPAS-A: General Profile and Structure Analysis Software for Powder Diffraction Data.*

Dawson, A., Allan, D. R., Parsons, S. & Ruf, M. (2004). *J. Appl. Crystallogr.* **37**, 410-416.

Fortes, A. D. (2004). PhD thesis, University of London.

Frisch, M. J., Trucks, G. W., Schlegel, H. B., Scuseria, G. E., Robb, M. A., Cheeseman, J. R., J. A. Montgomery, J., Vreven, T., Kudin, K. N., Burant, J. C., Millam, J. M., Iyengar, S. S., Tomasi, J., Barone, V., Mennucci, B., Cossi, M., Scalmani, G., Rega, N., Petersson, G. A., Nakatsuji, H., Hada, M., Ehara, M., Toyota, K., Fukuda, R., Hasegawa, J., Ishida, M., Nakajima, T., Honda, Y., Kitao, O., Nakai, H., Klene, M., Li, X., Knox, J. E., Hratchian, H. P., Cross, J. B., Bakken, V., Adamo, C., Jaramillo, J., Gomperts, R., Stratmann, R. E., Yazyev, O., Austin, A. J., Cammi, R., Pomelli, C., Ochterski, J. W., Ayala, P. Y., Morokuma, K., Voth, G. A., Salvador, P., Dannenberg, J. J., Zakrzewski, V. G., Dapprich, S., Daniels, A. D., Strain, M. C., Farkas, O., Malick, D. K., Rabuck, A. D., Raghavachari, K., Foresman, J. B., Ortiz, J. V., Cui, Q., Baboul, A. G., Clifford, S., Cioslowski, J., Stefanov, B. B., Liu, G., Liashenko, A., Piskorz, P., Komaromi, I., Martin, R. L., Fox, D. J., Keith, T., Al-Laham, M. A., Peng, C. Y., Nanayakkara, A., Challacombe, M., Gill, P. M. W., Johnson, B., Chen, W., Wong, M. W., Gonzalez, C. & Pople, J. A. (2004). *Gaussian03.* Version Revision E.01. Wallingford CT.

Gavezzotti, A. (2003). *OPiX: A computer program package for the calculation of intermolecular interactions and crystal energies.* University of Milan, Italy.

Gavezzotti, A. (2005a). *Struct. Chem.* **220**, 499-510.

Gavezzotti, A. (2005b). *Z. Kristallogr.* **220**, 499-510.

Kuznetsov, A. Z., Dmitriev, V., Dubrovinsky, L., Prakapenka, V. & Weber, H. P. (2002). *Solid State Commun.* **122**.

Ladell, J. & Post, B. (1954). *Acta. Cryst.* **7**, 559-564.

Larson, A. C. (1970). *Crystallographic Computing, International Summer School* 291-294.

Marshall, W. G. & Francis, D. J. (2002). *J. Appl. Crystallogr.* **35**, 122-125.

Miller, R. A. & Schuele, D. E. (1969). *J. Phys. Chem. Solids* **30**, 589-600.

Miyake, M., Kaji, O., Nakagawa, N. & Suzuki, T. (1985). *Journal of the Chemical Society Faraday Transactions* **81**, 277-281.

Ohtaki, H., Funari, A., Rode, B. M. & Reibnegger, G. J. (1983). *Bull. Chem. Soc. Jpn.* **56**, 2116-2121.

Parsons, S. (2004). *SHADE.* The University of Edinburgh.

Piermarini, G. J., Block, S., Barnett, J. D. & Forman, R. A. (1975). *J. Appl. Phys.* **46**, 2774-2780.

Sheldrick, G. M. (1997). *SHELX97. Programs for Crystal Structure Analysis.* University of Gottingen.

Shimizu, H., Nagata, K. & Sasaki, S. (1988). *J. Chem. Phys.* **89**, 2743-2747.

Stevens, E. D. (1977). *Acta. Cryst.* **B34**, 544-551.

Torrie, B. H. & Brown, B. A. (1994). *J. Raman Spectrosc.* **25**, 183-187.

Waldorf, D. L. & Alers, G. A. (1962). *J. Appl. Phys.* **33**, 3266-3269.

Wolff, S. K., Grimwood, D. J., McKinnon, J. J., Jayatilaka, D. & Spackman, M. A. (2005). *CrystalExplorer 1.5.*

Chapter 5
Phase behaviour of pyrazine

5.1 Introduction

Pyrazine, 1,4-diazabenzene, is a relatively simple molecular compound containing only one type of functional group yet it is known to show interesting phase diversity. There are three known phases; phase I is stable < 302 K, phase II between 302 K & 310 K and phase III between 310 K & 324 K (Bougeard *et al.*, 1978). The compound is liquid above 324 K. The nature of the phase transitions in pyrazine has been the subject of several investigations employing a wide range of techniques. Despite this, phase I is the only phase to be fully characterised. The crystal structure was initially determined at room temperature (Wheatley, 1957) and later at 184 K (DeWith *et al.*, 1976), however temperatures below this have not been studied. Phase I is orthorhombic, space group *Pmnn* with $Z' = 0.25$. No structural data are available for phases II & III, however a unit cell and space group have been proposed for phase III (Bougeard *et al.*, 1978).

Calorimetric measurements (Bougeard *et al.*, 1978; Boyd *et al.*, 1979) have shown that the entropy change associated with the transition from phase I to II is much greater than that associated with the transition from II to III. The enthalpy of the transition from phase II to III is very low and the transition is not always observed in calorimetric studies (Schettino *et al.*, 1972). This has been interpreted that the structure of phase II is more similar to phase III than phase I. Several studies have focused on the infrared and Raman spectra of pyrazine and have been interpreted to show that the crystal structure of phase II should have a similar molecular arrangement to phase III.

The effect of pressure on the crystal structure of pyrazine up to 5 GPa has been investigated using Raman spectroscopy with spectral changes indicating a phase transition at approximately 1 GPa (Maehara *et al.*, 1995). No other studies on the effect of pressure have been performed.

In this work, the effect of temperature on the crystal structure of pyrazine is investigated between 8 K and 315 K using neutron powder diffraction, including the formation of a fourth previously unobserved phase at low temperatures. The effect of

pressure to 9.36 GPa has also been investigated and the structure of the high pressure phase formed just below 1 GPa determined.

5.2 Experimental

Pyrazine-d_4 was purchased from Aldrich. A crystal was taken from the sample bottle and shown to be phase I by X-ray single crystal diffraction.

5.2.1 High-pressure neutron powder diffraction

Ambient temperature, high pressure neutron powder diffraction data were collected *via* the time-of-flight technique using the PEARL beamline high pressure facility (HiPr) at ISIS. A lightly ground sample of pyrazine-d_4 was contained in a null-scattering Ti-Zr alloy capsule gasket (Marshall & Francis, 2002) along with a 4:1 mixture of deuterated methanol and ethanol as hydrostatic medium and loaded into a Paris-Edinburgh cell. As pyrazine readily sublimes at ambient temperature, the sample and all equipment used in the loading of the gasket were chilled in advance and the loading carried out in a plastic hood with a container of liquid nitrogen inside to keep the temperature below ambient. A small pellet of lead was also included in the loading as a pressure marker. The pressure was calculated from the refined lead unit cell parameter using a Birch-Murnaghan equation of state (Birch, 1947) with V_o = 30.3128 Å^3, B_o = 41.92 GPa, B' = 5.72. These parameters were derived by Fortes (2004) as averages of the values determined in three earlier studies (Kuznetsov *et al.*, 2002; Miller & Schuele, 1969; Waldorf & Alers, 1962).

The pressure was increased in small steps to a final pressure of 9.36 GPa. On increasing the pressure from 0.65 GPa to 0.94 GPa a phase transition was observed. We have designated this phase IV. Above 6.10 GPa there is a subtle change in the pattern with two new peaks growing in progressively up to 9.36 GPa.

5.2.2 Variable temperature neutron powder diffraction

Variable temperature time-of-flight neutron powder diffraction data were recorded using the HRPD instrument at ISIS. The sample was initially ground in a liquid nitrogen chilled stainless steel mortar (Ibberson, 1996) before being loaded into a

rectangular aluminium sample can held over a container of liquid nitrogen to prevent sublimation of the sample. The sample was loaded into a closed cycle refrigerator (CCR) and initially cooled to 180 K. A short data collection confirmed the sample was in phase I, and so the sample was cooled to 8 K. On cooling, a phase transition was observed at approximately 90 K to phase IV, the same phase as observed at 0.94 GPa in the high pressure study. Data were collected at 8 K followed by rapid data collections every 5 K while warming the sample to 290 K. The transition from phase IV to phase I was observed at 90 K. Above 290 K the sample began to sublime and escape the sample can.

A second sample was loaded, as above, with the aim of collecting data on phases II and III. Particular care was taken to ensure the sample can was completely sealed. After confirming the sample was in phase I, it was warmed to 308 K and data collected on phase II. The sample was then warmed to 315 K and data collected on phase III.

5.2.3 Structure solution and refinement

High pressure

All Rietveld refinements were performed using TOPAS-Academic (Coelho, 2007). Phase IV was indexed using DICVOL91 (Boultif & Louer, 1994), indicating a monoclinic cell closely related to that of phase I. Suitable coordinates for the monoclinic structure were generated *via* CRYSCON (Shape Software) on the basis of the phase I structure.

During refinement of the high-pressure data the molecules were treated as rigid groups in TOPAS, modelled such that the molecules had D_{2h} symmetry. Bond lengths and angles were taken from the previously determined structure (Wheatley, 1957, CSD refcode PYRAZI) with deuterium distances set to standard neutron distances (C-H 1.083 Å). Bond lengths and angles were not refined. All non-hydrogen atoms were refined with a common isotropic displacement parameter, as were all deuterium atoms. A fourth order spherical harmonic preferred orientation correction was included. Ni and WC phases were also included in the refinement.

The presence of these is due to the anvils of the Paris-Edinburgh cell. Above 6.10 GPa the two new peaks which grew in progressively up to 9.36 GPa were fitted separately as individual peaks. A selection of Rietveld refinement profiles up to 9.36 GPa are shown in Figures 5.1 and 5.2 for phase I and IV respectively, with crystal and refinement data given in Tables 5.1 and 5.2.

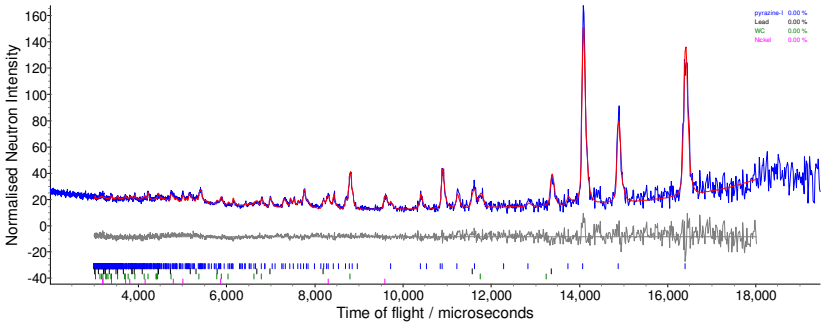

(a) 0.11 GPa

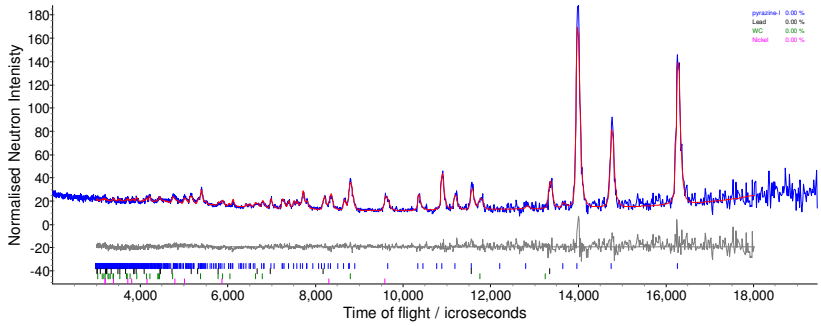

(b) 0.26 GPa

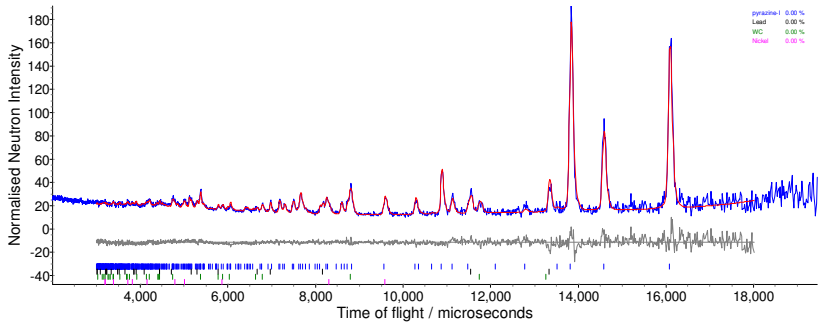

(c) 0.41 GPa

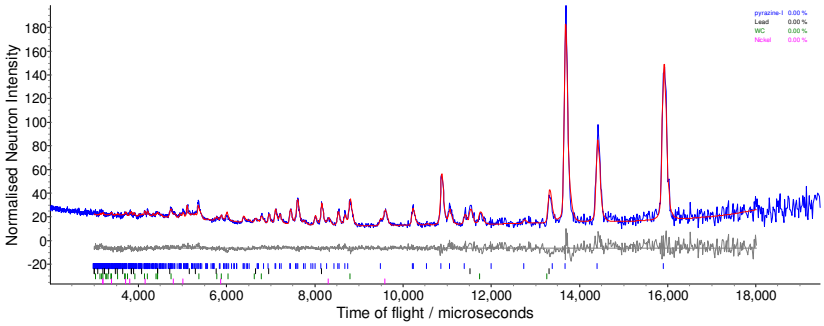

(d) 0.65 GPa

Figure 5.1 Rietveld refinement profiles for the high pressure study of pyrazine-I. Blue and red lines correspond to observed and calculated data respectively. The difference is shown in grey.

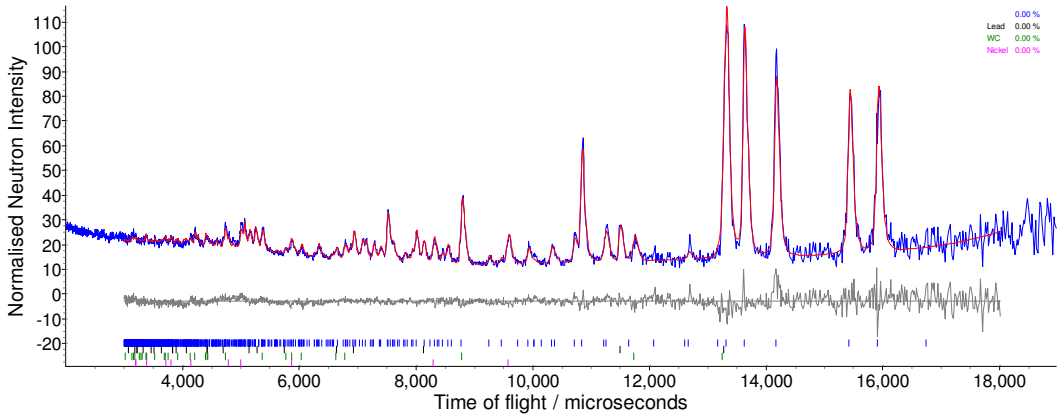

(a) 0.94 Gpa

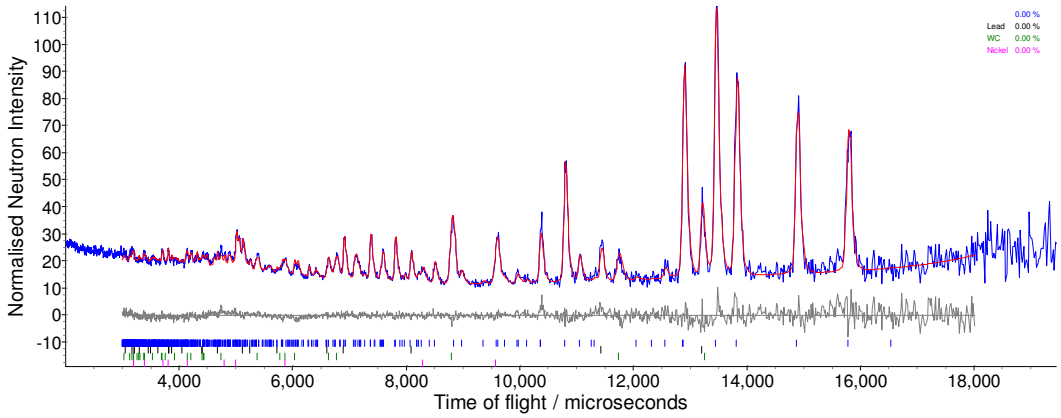

(b) 1.82 GPa

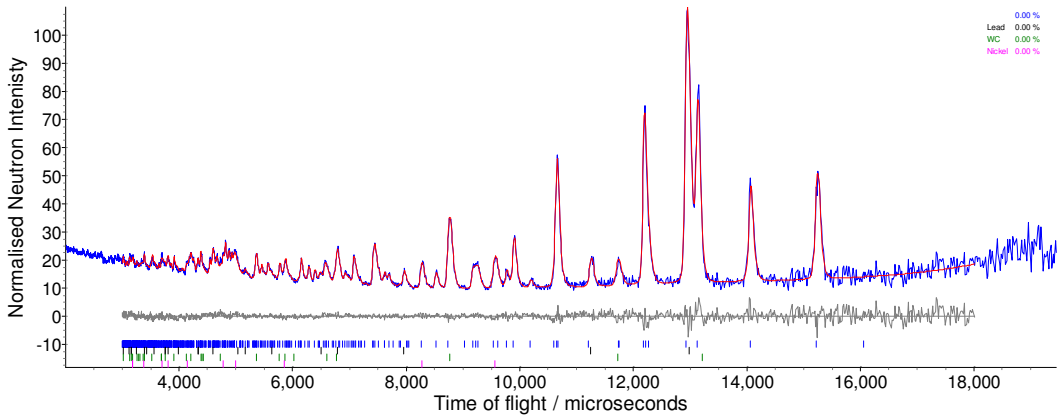

(c) 4.71 GPa

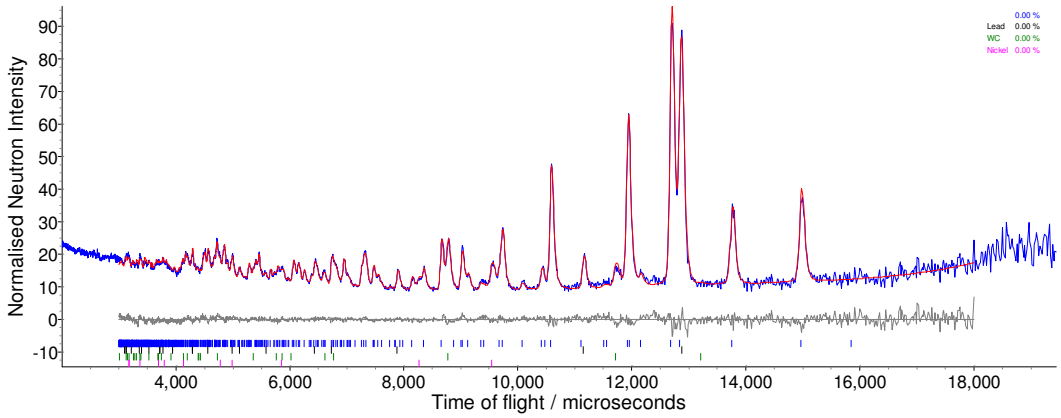

(d) 6.10 GPa

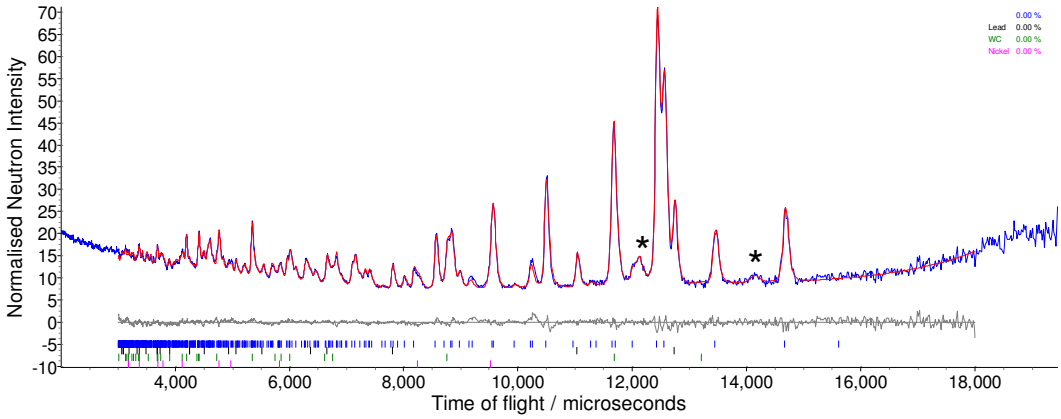

(e) 9.36 GPa

Figure 5.2 Rietveld refinement profiles for the high pressure study of pyrazine-IV. Blue and red lines correspond to observed and calculated data respectively. The difference is shown in grey.

Pyrazine-*d*$_4$ I				
Pressure (GPa)	0.11	0.26	0.41	0.65
Temperature (K)	298	298	298	298
Crystal Data				
Chemical formula	$C_4D_4N_2$	$C_4D_4N_2$	$C_4D_4N_2$	$C_4D_4N_2$
M_r	84.10	84.10	84.10	84.10
Cell setting, space group	Orthorhombic, *Pmnn*	Orthorhombic, *Pmnn*	Orthorhombic, *Pmnn*	Orthorhombic, *Pmnn*
a, b, c (Å)	9.3023(14), 3.7796(5), 5.8702(13)	9.2965(13), 3.7457(4), 5.8307(12)	9.2930(9), 3.6973(3), 5.7749(10)	9.2837(9), 3.6506(3), 5.7177(10)
α, β, γ (°)	90, 90, 90	90, 90, 90	90, 90, 90	90, 90, 90
V (Å^3)	206.39(6)	203.04(5)	198.42(4)	193.78(4)
Z	2	2	2	2
D_{calc} (g cm^{-3})	1.353	1.376	1.408	1.441
Radiation type	Neutron	Neutron	Neutron	Neutron
Specimen form	Powder	Powder	Powder	Powder
Data Collection				
Diffractometer	PEARL, ISIS	PEARL, ISIS	PEARL, ISIS	PEARL, ISIS
Collection method	Time of flight	Time of flight	Time of flight	Time of flight
Range of *d* (Å)	0.64-3.8	0.64-3.8	0.64-3.8	0.64-3.8
Refinement				
Method	Rietveld	Rietveld	Rietveld	Rietveld
R_p	8.227	8.003	6.975	7.083
R_{wp}	7.344	7.482	6.433	6.650
S	1.233	1.220	1.282	1.336
Background	6 term Chebychev polynomial	6 term Chebychev polynomial	6 term Chebychev polynomial	6 term Chebychev polynomial
Profile function	Back-to-back exponential convoluted with Voigt function	Back-to-back exponential convoluted with Voigt function	Back-to-back exponential convoluted with Voigt function	Back-to-back exponential convoluted with Voigt function
Number of parameters	30	30	30	30
Weighting scheme	$1/\sigma^2$	$1/\sigma^2$	$1/\sigma^2$	$1/\sigma^2$

Table 5.1 Crystal and refinement data for pyrazine-I.

Pyrazine-d_4 IV					
Pressure (GPa)	0.94	1.82	4.71	6.10	9.36
Temperature (K)	298	298	298	298	298
Crystal Data					
Chemical formula	$C_4D_4N_2$	$C_4D_4N_2$	$C_4D_4N_2$	$C_4D_4N_2$	$C_4D_4N_2$
M_r	84.10	84.10	84.10	84.10	84.10
Cell setting, space group	Monoclinic, $P11_21/n$	Monoclinic, $P11_21/n$	Monoclinic, $P11_21/n$	Monoclinic, $P11_21/n$	Monoclinic, $P11_21/n$
a, b, c (Å)	9.2747(8), 3.6026(3), 5.6488(8)	9.2588(7), 3.5132(2), 5.4962(7)	9.1716(6), 3.34866(19), 5.2228(5)	9.1326(5), 3.29787(18), 5.1406(4)	9.0466(5), 3.20845(19), 5.0007(4)
α, β, γ (°)	90, 90, 92.075(9)	90, 90, 95.076(8)	90, 90, 97.153(6)	90, 90, 97.511(5)	90, 90, 97.941(6)
V (Å^3)	188.62(3)	178.08(3)	159.16(2)	153.499(18)	143.758(17)
Z	2	2	2	2	2
D_{calc} (g cm^{-3})	1.481	1.568	1.755	1.820	1.943
Radiation type	Neutron	Neutron	Neutron	Neutron	Neutron
Specimen form	Powder	Powder	Powder	Powder	Powder
Data Collection					
Diffractometer	PEARL, ISIS	PEARL, ISIS	PEARL, ISIS	PEARL, ISIS	PEARL, ISIS
Collection method	Time of flight	Time of flight	Time of flight	Time of flight	Time of flight
Range of *d* (Å)	0.64-3.8	0.64-3.8	0.64-3.8	0.64-3.8	0.64-3.8
Refinement					
Method	Rietveld	Rietveld	Rietveld	Rietveld	Rietveld
R_p	5.220	5.494	4.487	3.842	2.898
R_{wp}	4.964	5.121	4.118	3.812	3.081
S	1.412	1.284	1.271	1.388	1.886
Background	6 term Chebychev polynomial	6 term Chebychev polynomial	6 term Chebychev polynomial	6 term Chebychev polynomial	6 term Chebychev polynomial
Profile function	Back-to-back exponential convoluted with Voigt function	Back-to-back exponential convoluted with Voigt function	Back-to-back exponential convoluted with Voigt function	Back-to-back exponential convoluted with Voigt function	Back-to-back exponential convoluted with Voigt function
Number of parameters	38	38	38	38	38
Weighting scheme	$1/\sigma^2$	$1/\sigma^2$	$1/\sigma^2$	$1/\sigma^2$	$1/\sigma^2$

Table 5.2 Crystal and refinement data for pyrazine-IV.

Variable temperature measurements

All Rietveld refinements were performed using TOPAS-Academic (Coelho, 2007). Initial coordinates for phase I were taken from the previously published structure (Wheatley, 1957, CSD refcode PYRAZI). Atomic coordinates and anisotropic displacement parameters were refined freely for the C and D atoms and the appropriate parameters refined for the N atom taking into account the special position.

Phase III was indexed using TOPAS-Academic with two possible space groups; *Pc* and $P2_1/c$. The structure was initially solved in space group *Pc*, however, X-ray single crystal studies by Byrne & Parsons (2009) indicated the true space group was $P2_1/c$. Based on this information, the structure of phase III was subsequently solved from the neutron powder diffraction data in $P2_1/c$ using TOPAS-Academic. During refinement the molecules were treated as rigid groups modelled such that they had D_{2h} symmetry. Anisotropic displacement parameters were modelled using the TLS formalism. A fourth order spherical harmonic preferred orientation correction was also included. During refinement it became evident that the pattern was mixed phase and an intensity only fit for phase II was added to the refinement.

Initial coordinates for phase IV were taken from the high pressure data. During refinement the molecules were treated as rigid groups with D_{2h} symmetry. Appropriate bond lengths and angles were refined and anisotropic displacement parameters refined freely. In order to obtain a good fit to the data it was necessary to refine the absorption correction which refined to give a value of the absorption coefficient of 0.721(7) cm^{-1}. The value is rather high as it is correcting for absorption due to both the sample and the sample can.

Rietveld refinement profiles for phases I, III & IV are shown in Figure 5.3, with crystal and refinement data given in Table 5.3.

Pawley (1981) fits were performed on the rapid scan data in the range 10 – 245 K to obtain the lattice parameters.

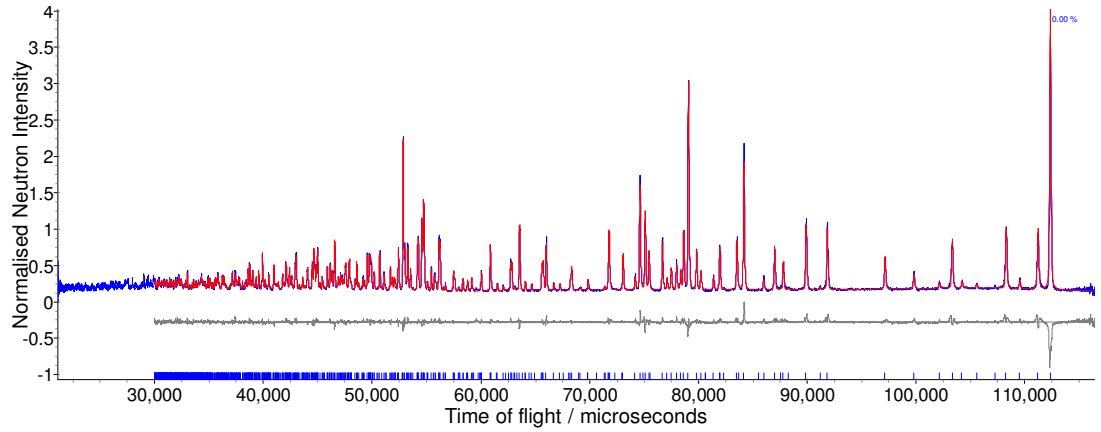

(a) 8 K Pyrazine-IV

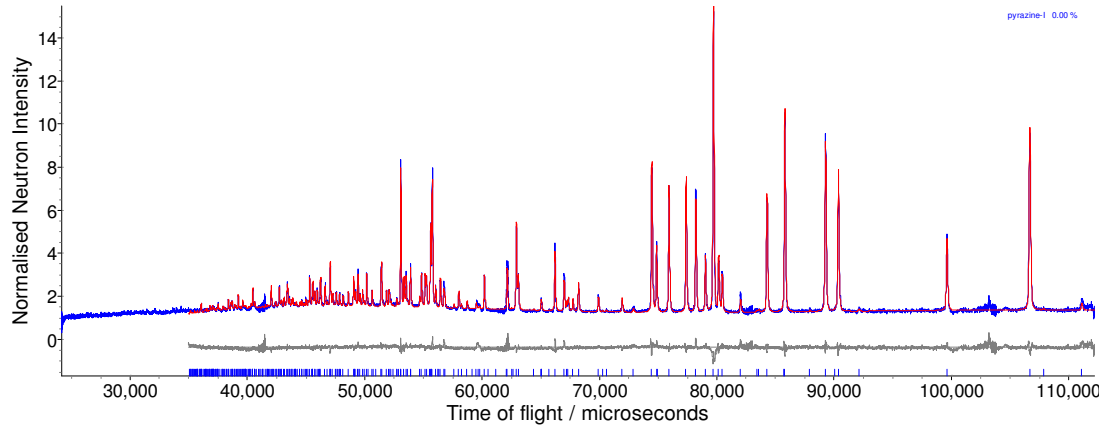

(b) 180 K Pyrazine-I

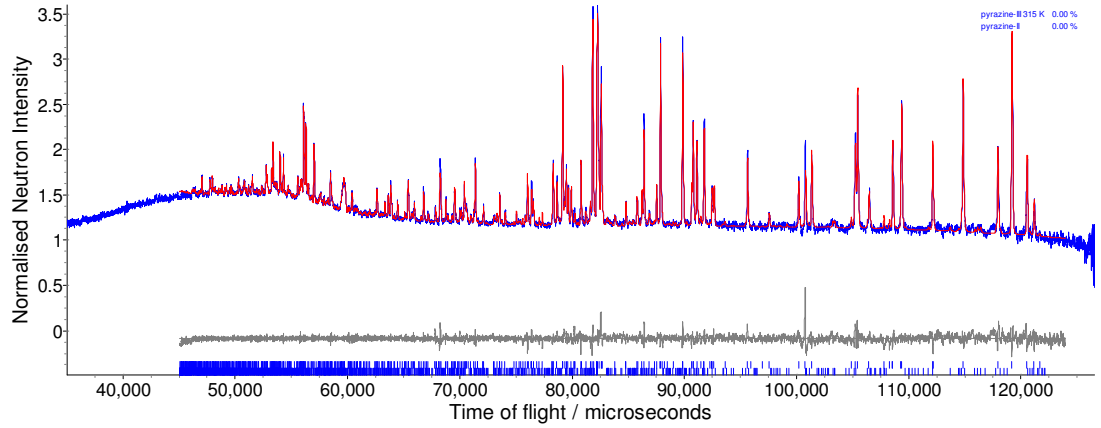

(c) 315 K Pyrazine-III

Figure 5.3 Rietveld refinement profiles for pyrazine-IV. Blue and red lines correspond to observed and calculated data respectively. The difference is shown in grey.

	Pyrazine-d_4		
Phase	**IV**	**I**	**III**
Temperature (K)	8	180	315
Crystal Data			
Chemical formula	$C_4D_4N_2$	$C_4D_4N_2$	$C_4D_4N_2$
M_r	84.10	84.10	84.10
Cell setting, space group	Monoclinic, $P11_21/n$	Orthorhombic, *Pmnn*	Monoclinic, $P2_1/c$
a, b, c (Å)	9.32887(2), 3.665170(9), 5.789727(15)	9.32070(3), 3.733194(11), 5.85253(2)	11.26799(10), 3.834114(17), 11.08440(8)
α, β, γ (°)	90, 90, 93.1758(2)	90, 90, 90	90, 116.9045(6) , 90
V (Å^3)	197.66(1)	203.65(1)	427.04(1)
Z	2	2	4
D_{calc} (g cm^{-3})	1.413	1.372	1.308
Radiation type	Neutron	Neutron	Neutron
Specimen form	Powder	Powder	Powder
Data Collection			
Diffractometer	HRPD, ISIS	HRPD, ISIS	HRPD, ISIS
Collection method	Time of flight	Time of flight	Time of flight
Range of *d* (Å)	0.62 - 2.49	0.72 - 2.49	0.93 - 2.57
Refinement			
Method	Rietveld	Rietveld	Rietveld
R_p	4.275	3.434	1.582
R_{wp}	5.019	4.125	1.859
S	2.413	1.808	1.494
Background	6 term Chebychev polynomial	6 term Chebychev polynomial	6 term Chebychev polynomial
Profile function	Back-to-back exponential	Back-to-back exponential	Back-to-back exponential
Number of parameters	55	35	54
Weighting scheme	$1/\sigma^2$	$1/\sigma^2$	$1/\sigma^2$

Table 5.3 Crystal and refinement data for pyrazine in the range 8 – 315 K.

5.2.4 Differential Scanning Calorimetry

A differential scanning calorimetry (DSC) trace was recorded on pyrazine-h_4 using a Perkin Elmer Pyris 1 DSC instrument with the sample contained in a closed aluminium pan. The sample was loaded at room temperature and initially cooled to 95 K and then heated to 340 K at a rate of 10 K/min.

5.3 Results

Variable temperature neutron powder diffraction studies have shown pyrazine forms four phases in the temperature range 8 – 324 K. Phase I was the only phase fully characterised previously. The crystal structures of phases III & IV have now been determined.

Ambient temperature, high-pressure studies show that on increasing the pressure to 0.94 GPa a phase transition is observed. The high-pressure phase corresponds to the same structure observed at temperatures below 90 K, phase IV.

The crystal structures of phases I, III & IV of pyrazine are discussed below.

5.3.1 Phase I

The structure of pyrazine-I has previously been characterised by X-ray single crystal diffraction at room temperature (Bougeard *et al.*, 1978) and 184 K (DeWith *et al.*, 1976). Pyrazine-I is orthorhombic, space group *Pmnn*, with $Z' = 0.25$. Each molecule forms C-H…N interactions (C-H…N 2.4948(10) Å at 180 K) with eight others forming a three dimensional network, Figure 5.4. All the C-H groups are involved in C-H…N bridges and each N atom is bifurcated between two hydrogen atoms. The molecules are stacked *via* cell translations along the *b* axis to form π-stacking interactions (centroid-centroid distance 3.733 Å).

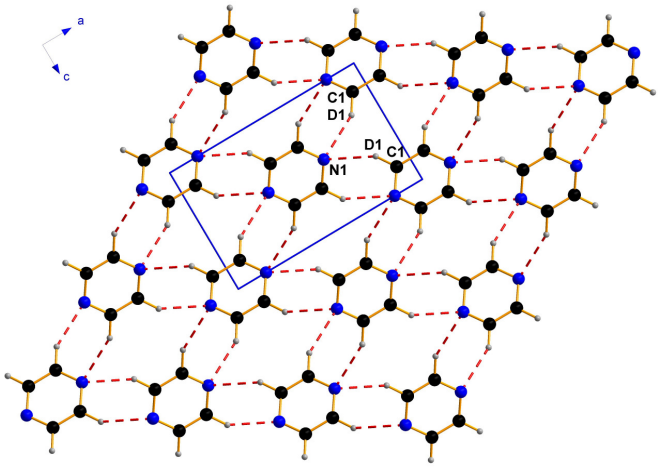

(a) C-H…N interactions

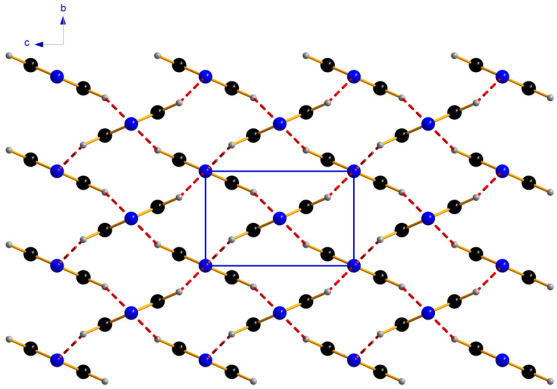

(b) 3-dimensional network

Figure 5.4 Crystal structure of pyrazine-I.

5.3.2 Phase III

The structure of phase III is monoclinic, space group $P2_1/c$. The molecules are positioned across inversion centres with two half molecules in the asymmetric unit. As in phase I, each molecule forms eight C-H…N interactions to form a three dimensional network however the pattern of the interactions is different. In projection, the structure appears to consist of chains of molecules linked *via* C-H…N interactions parallel to the *c* axis with alternate chains orientated differently, Figure 5.5. Further C-H…N interactions link the chains together. There are four symmetry independent C-H groups resulting in four different C-H…N interaction lengths, listed in Table 5.4.

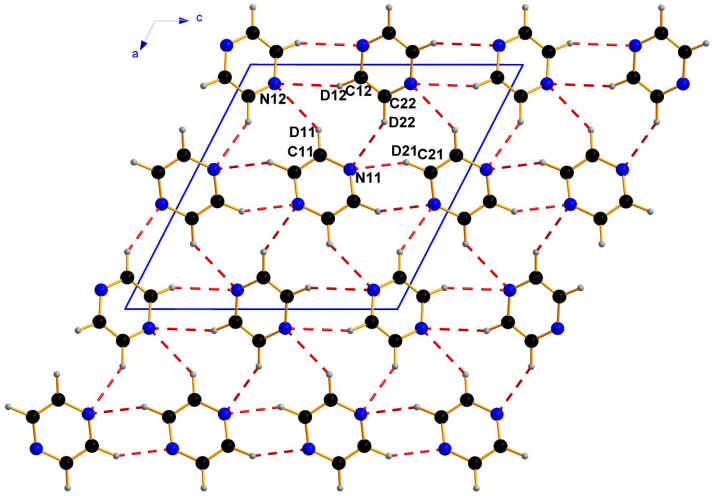

Figure 5.5 C-H…N interactions in pyrazine-III

Interaction	D…N / Å
C11-D11…N12^{i}	2.767(16)
C12-D12…N12^{ii}	2.552(4)
C21-D21…N11^{iii}	2.529(10)
C22-D22…N11^{iv}	2.659(10)

(i) 1-*x*, ½ +*y*, ½-*z*. (ii) -*x*, ½ +*y*, ½-*z*. (iii) 1-*x*, -½ +*y*, -½-*z*. (iv) 1-*x*, -*y*, -*z*.

Table 5.4 C-H..N interactions in pyrazine-III.

5.3.3 Phase IV

Phase IV is monoclinic, space group $P112_1/n$, with $Z' = 0.5$. A non-standard setting of the monoclinic cell with *c* as the unique axis was chosen to maintain the axes relative to phase I. Each molecule forms eight C-H…N interactions with surrounding molecules forming a three dimensional network with the same pattern of C-H…N interactions as in phase I. In phase IV the molecules are rotated relative to those in phase I, reducing the symmetry. This results in two symmetry independent C-H groups and therefore two different C-H…N interaction lengths (C1-D1…N1 2.443(2) & C2-D2…N1 2.459(2) Å at 8 K). Molecules related by translation along the *b* axis form π-stacking interactions (centroid-centroid distance 3.665 Å).

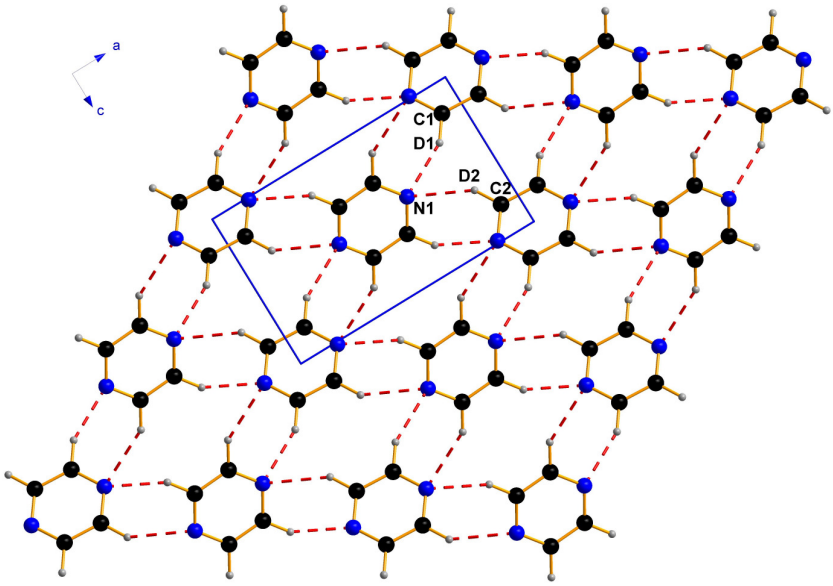

Figure 5.6 C-H…N interactions in pyrazine-IV.

5.3.4 Differential Scanning Calorimetry

A differential scanning calorimetry (DSC) trace was recorded for pyrazine with a heating/cooling rate of 10 K/min, Figure 5.7. The sample was loaded at room temperature before cooling to 95 K. No thermal events were observed in this region. The transition to phase IV occurs at 90 K and therefore could not be observed.

On heating the sample to 340 K an endothermic event occurs at 304 K followed by the onset of the sample melting at 325 K. The peak at 304 K corresponds to the transition from phase I to phase II, however the second transition to phase III is not observed. The absence of the second transition is consistent with the DSC results of Schettino *et al.* (1972). Bougeard *et al.* (1978) commented that the enthalpy change for the transition to phase III is very low and that it was not surprising that it was not observed by Schettino *et al.* (1972).

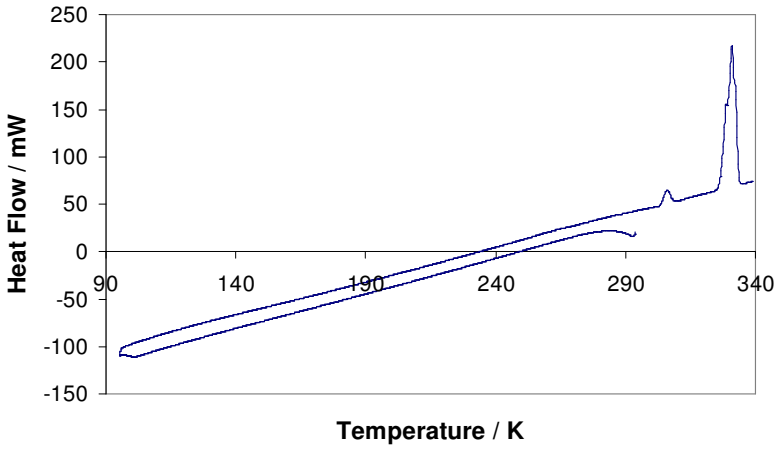

Figure 5.7 DSC trace for pyrazine.

5.4 Discussion

5.4.1 Effect of temperature

At 2 K pyrazine exists in phase IV. On increasing the temperature the *b*- and *c*-axes exhibit a smooth expansion up to 90 K at which point the transition to phase I occurs. Unusually, the *a*-axis decreases in length with increasing temperature. On going through the transition there is no visible discontinuity in the unit cell volume, however the transition is evident in the behaviour of the *a*- and *c*-axes as a function of temperature, Figure 5.8.

The crystal structures of phases I and IV are closely related and the setting of the monoclinic cell of phase IV was chosen to preserve the axes in relation to phase I. In both phases, each molecule forms C-H…N interactions with eight neighbouring molecules forming the same pattern of interactions, Figures 5.4 and 5.6. The difference between the structures is that the molecules are rotated round in phase IV relative to phase I, resulting in two symmetry independent C-H groups and therefore two different C-H…N interaction distances. The negative thermal expansion of the *a*-axis is likely to be related to this change in orientation of the molecules relative to the *a*-axis.

On increasing the temperature to 302 K the structure transforms to phase II followed closely by the transition to phase III at 310 K. Structure solution of phase II based on

the pattern obtained in the present neutron study has so far been unsuccessful and is discussed in more detail in Section 5.4.3. As in phases I and IV, each molecule in phase III forms eight C-H…N interactions forming a three dimensional network, however the pattern of interaction is different. In projection, the structures appear to consist of chains of molecules linked *via* C-H…N interactions with further C-H…N interactions between the chains, Figures 5.4 and 5.5. The difference between the structures is in the orientation of the chains. In phase I all the chains are oriented in the same direction whereas in phase III alternate chains are orientated differently.

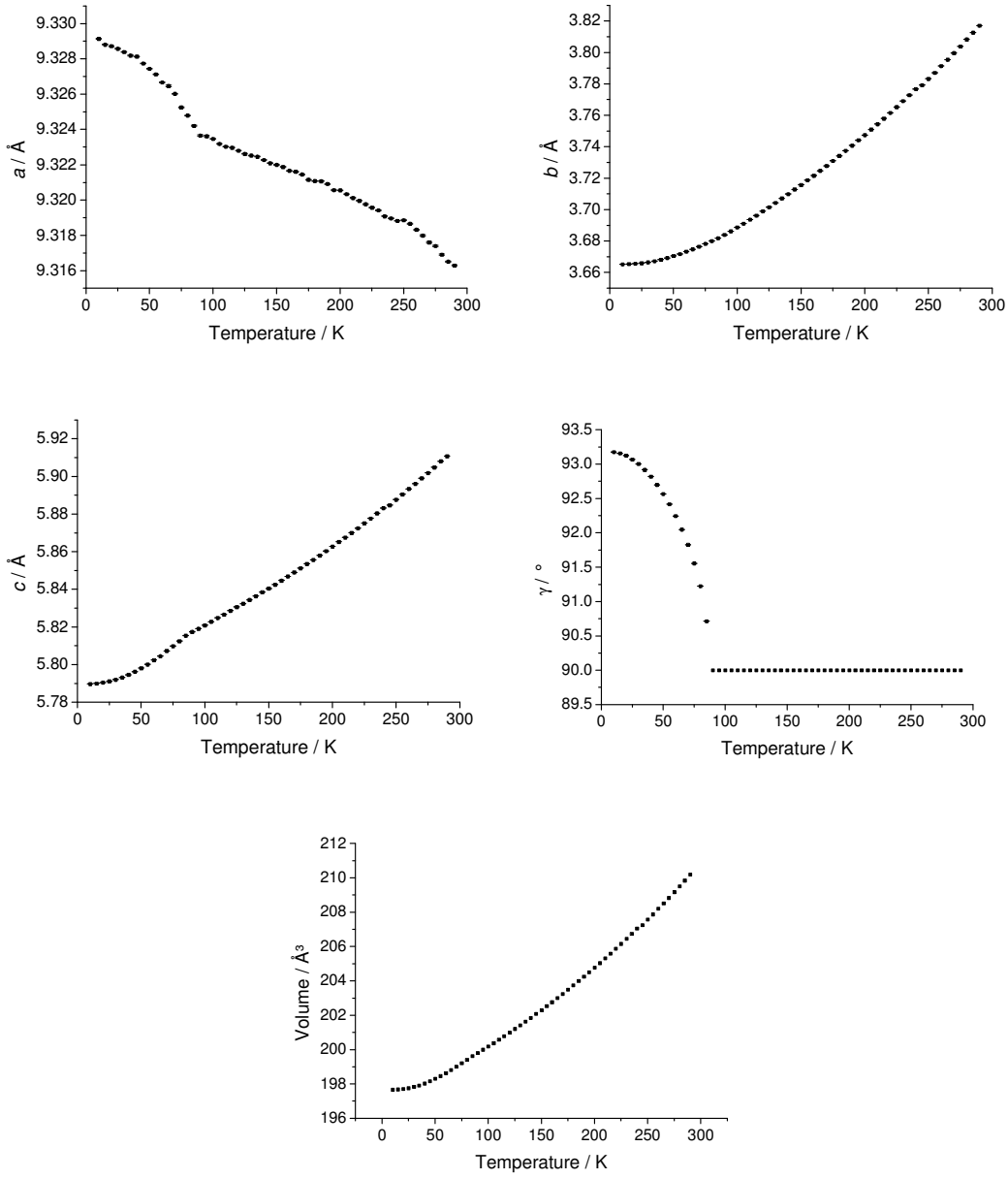

Figure 5.8 Unit cell parameters for pyrazine in the range 10 - 290 K.

5.4.2 Effect of pressure

At ambient pressure pyrazine exists in phase I. On increasing the pressure to 0.94 GPa a transition to phase IV is observed. This is consistent with the finding of Maehara *et al.* (1995) who observed a transition in Raman spectra just below 1 GPa. The transition between phase I and IV is also observed at low temperature and discussed in Section 5.4.1. The cell parameters exhibits a smooth variation as the pressure is increased, Figure 5.9.

The unit cell parameters exhibit an anisotropic response to increasing pressure. The *a*-axis is the least sensitive to pressure and only decreases by 0.26 Å on increasing the pressure from 0.11 GPa to 9.36 GPa, corresponding to 2.7 % of the 0.11 GPa value. The *b*- and *c*-axes are much more responsive to pressure exhibiting a 15.1 % and 14.8 % reduction, respectively, on increasing the pressure from 0.11 GPa to 9.36 GPa. The monoclinic unit cell angle γ increases rapidly to 97 ° before beginning to plateau. Overall, the unit cell volume reduces by 30 % of the 0.11 GPa value on increasing the pressure to 9.36 GPa.

The significant compression of the *b*- and *c*-axes corresponds to the closing up of voids between molecules related by translation. Figure 5.10 shows the closing up of voids between molecules related by translation along the *c*-axis. The resultant effect on the C-H…N interaction distance is shown in Table 5.5.

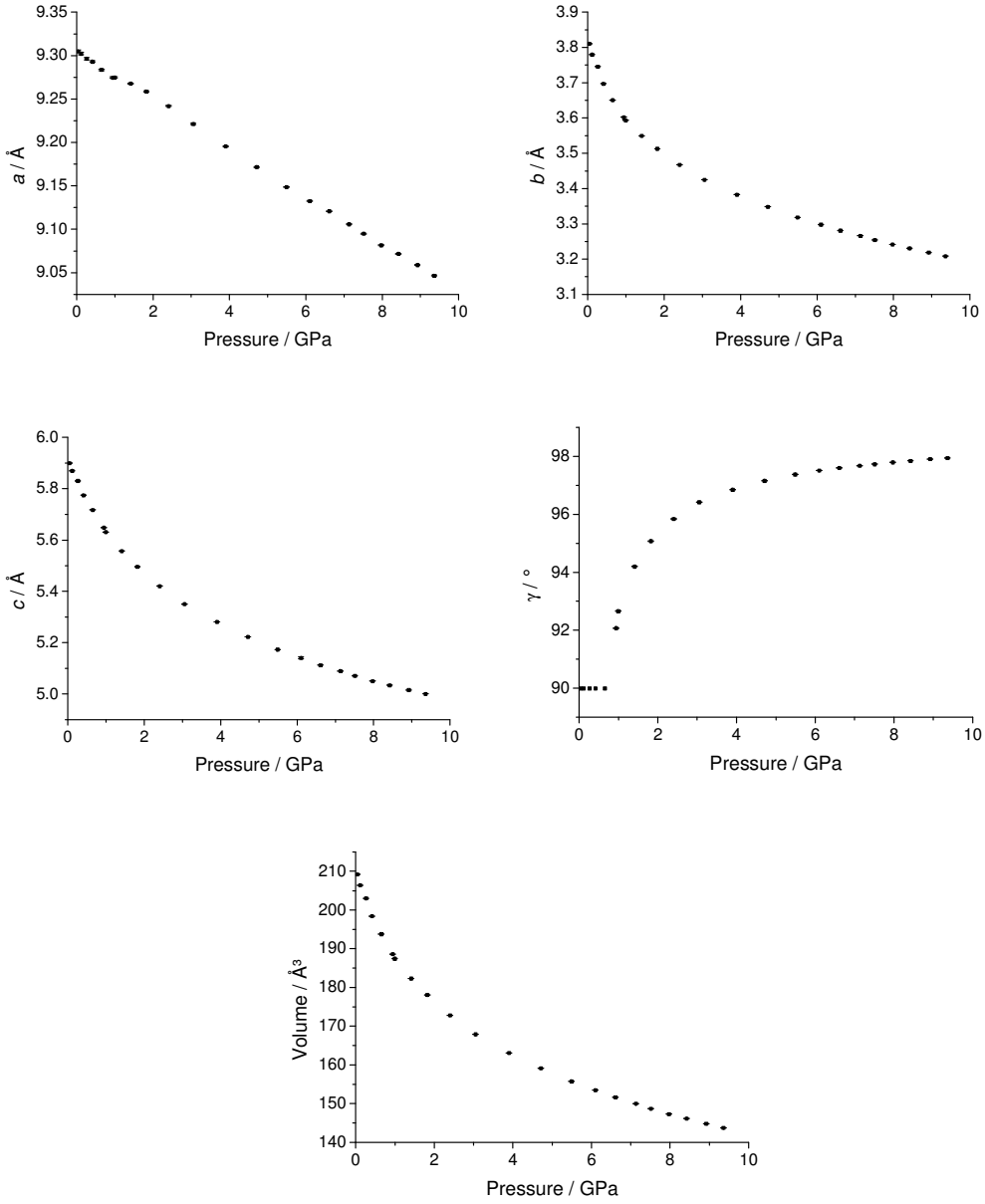

Figure 5.9 Unit cell parameters for pyrazine as a function of pressure.

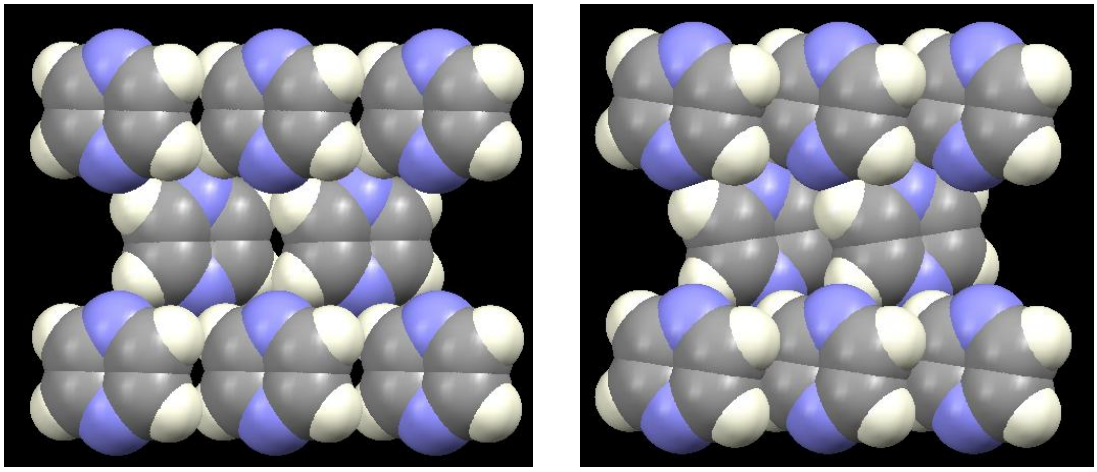

(a) 0.94 GPa (b) 9.36 GPa

Figure 5.10 Voids in pyrazine-IV.

Pressure / GPa	C1-D1…N1 / Å	C2-D2…N1 / Å
0.11	2.535(2)	-
0.65	2.468(2)	-
0.94	2.45(1)	2.421(9)
1.82	2.378(7)	2.422(5)
4.71	2.284(4)	2.348(2)
6.10	2.248(4)	2.322(2)
9.36	2.200(4)	2.263(2)

Table 5.5 C-H…N interaction lengths as a function of pressure.

Above 6.10 GPa a subtle change in the neutron powder pattern was observed with two new peaks growing in over a range of 2-3 GPa. Such small changes are likely to be due to loss of some translational symmetry and may be due to one or more of the cell axes doubling.

5.4.3 Phase II

Indexing and structure solution of the neutron powder diffraction pattern of phase II have so far been unsuccessful. Byrne & Parsons (2009) recently determined the structure of phase II *via* X-ray single crystal diffraction, with selected crystal data given in Table 5.6. The same structure was obtained for single crystals of pyrazine-h_4 and -d_4 however the neutron powder diffraction pattern of pyrazine-d_4 does not correspond to this structure, nor does it correspond to a mixture of phases I, II or III. Figure 5.11 shows the Pawley fits for the various mixed phase possibilities.

Doubling the cell parameters *a*, *b* & *c* determined by Byrne & Parsons (2009) and reducing the symmetry to $P\bar{1}$ is necessary in order to obtain a satisfactory fit to the pyrazine-d_4 powder pattern, Figure 5.12, thus there appears to be some discrepancy between the behaviour in powder and single crystal form. Selected crystal data are given in Table 5.7.

Cell setting	Monoclinic
Space group	$P2_1/c$
a (Å)	30.49
b (Å)	3.81
c (Å)	11.04
β (°)	100.26
V (Å³)	1263.14246(3)
Z	12
D_x (Mg m^{-3})	1.263
Temperature (K)	305

Table 5.6 Selected crystal data for pyrazine-h_4 phase II.

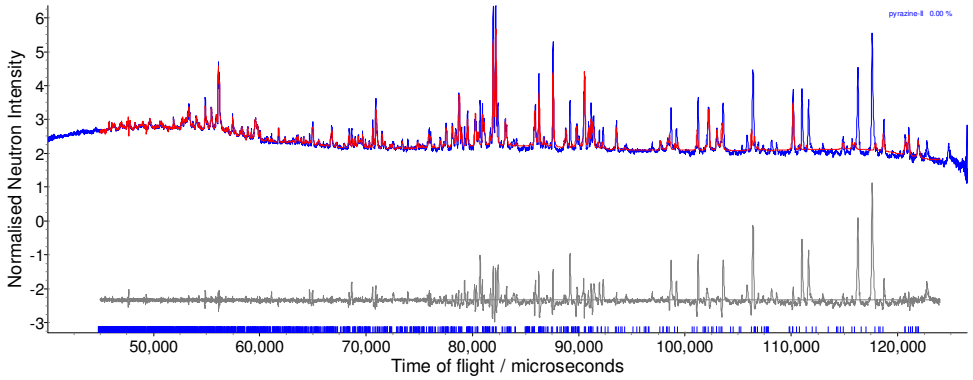

(a) Phase II

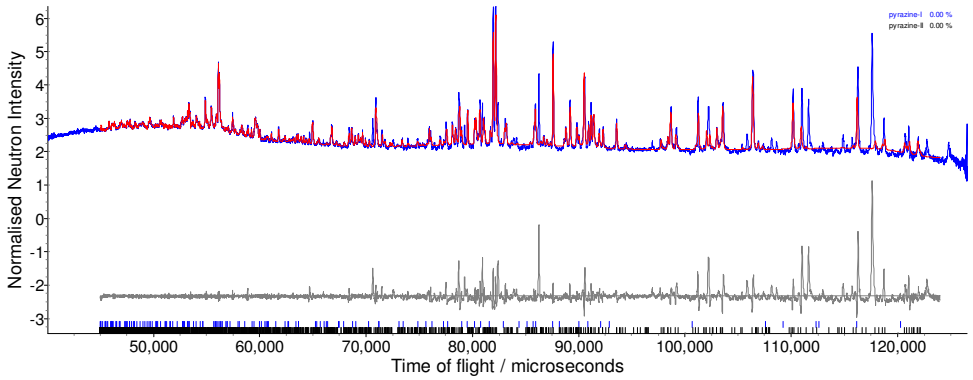

(b) Phases I & II

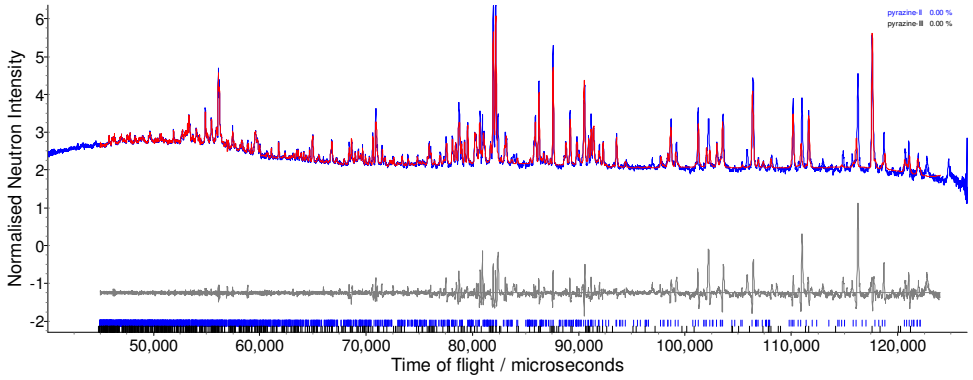

(c) Phases II & III

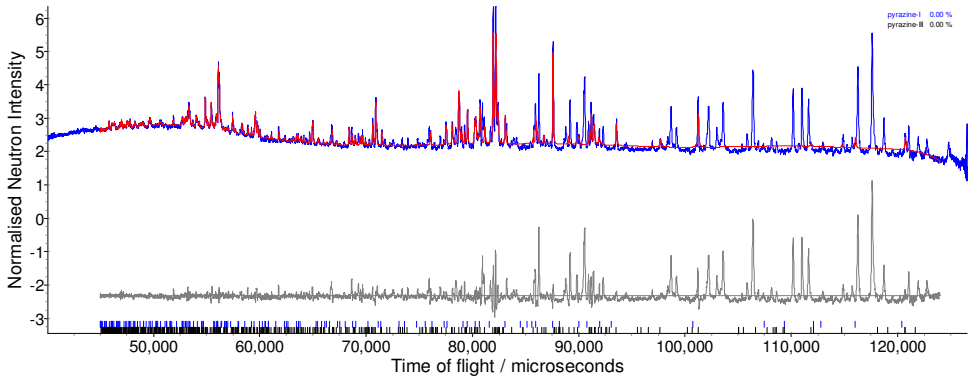

(d) Phases I & III

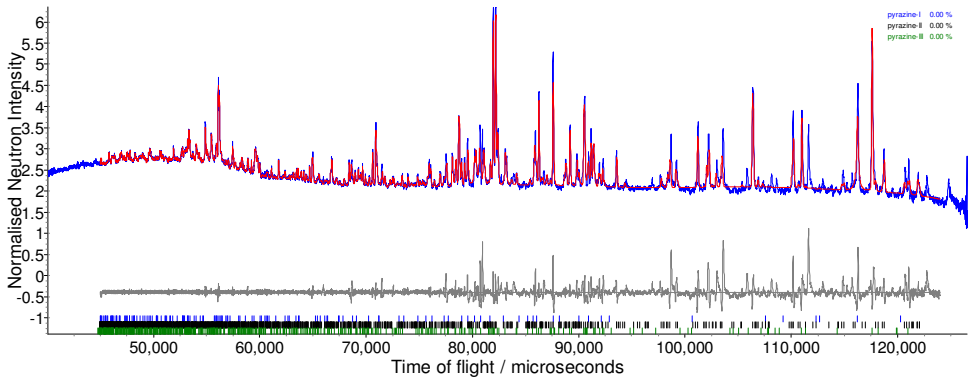

(e) Phases I, II & III

Figure 5.11 Pawley refinement profiles for pyrazine-d_4 at 308 K for various phases. Blue and red lines correspond to observed and calculated data respectively. The difference is shown in grey.

Cell setting	Triclinic
Space group	$P\bar{1}$
a (Å)	60.49134
b (Å)	7.59949
c (Å)	22.08286
α (°)	89.93403
β (°)	100.24933
γ (°)	89.90656
V (Å^3)	9989.55215
Z	96

Table 5.7 Selected crystal data for pyrazine-d_4 at 308 K.

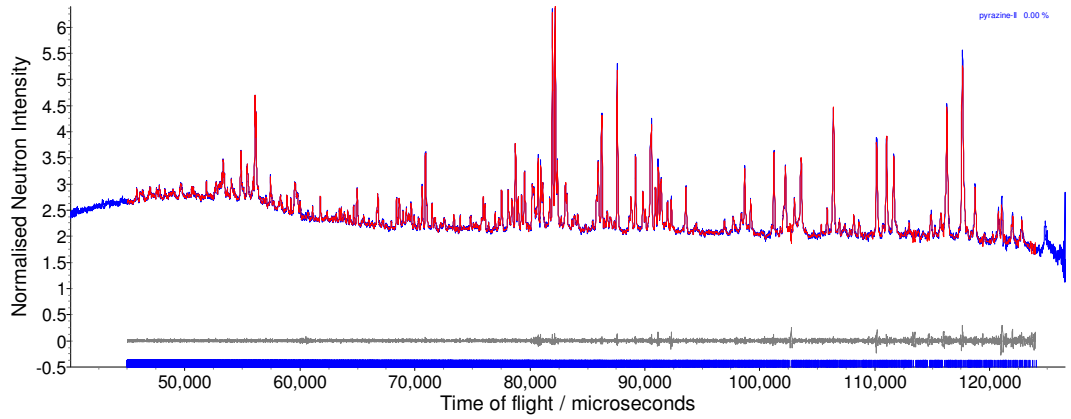

Figure 5.12 Pawley refinement profile for pyrazine-d_4 at 308 K. Blue and red lines correspond to observed and calculated data respectively. The difference is shown in grey.

On the basis of similarities in the infrared and Raman spectra, along with the weak phase II to III transition in calorimetric data, Bougeard *et al.* (1978) concluded that phase II was likely to be more similar to phase III than phase I. The structure of phase II determined by Byrne & Parsons (2009) is consistent with this; the pattern of C-H…N interactions, Figure 5.13, is similar to that observed in phase III.

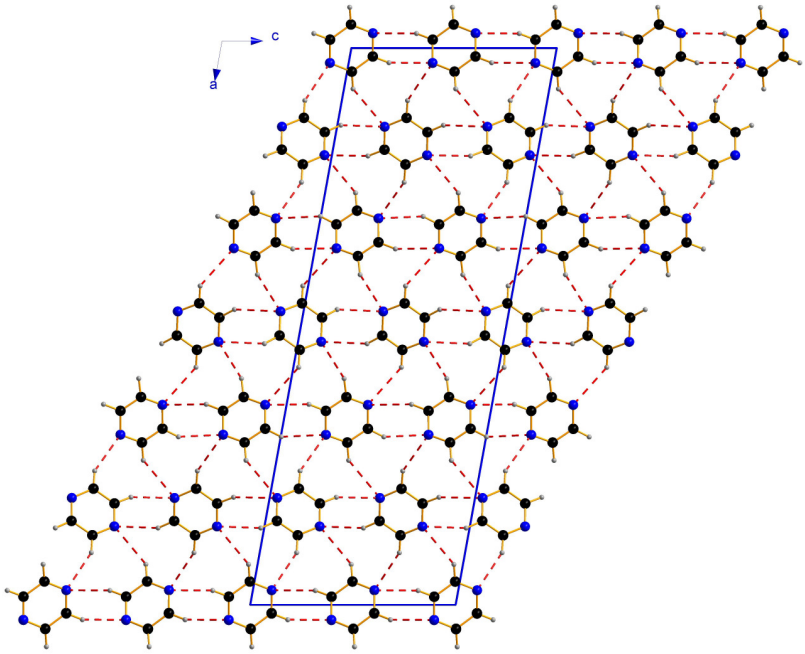

Figure 5.13 Molecular packing in pyrazine phase II.

5.4.4 Relationship between phases

The unit cells of all four phases of pyrazine are related, as shown in Table 1.8. The transition between phases I and IV is observed at low temperature and high pressure. A non-standard setting of the monoclinic cell of phase IV was chosen to allow simpler comparison of the two phases. On transforming from phase I to phase IV there is no change in the unit cell axes and no discontinuity in the unit cell volume. The symmetry is reduced from orthorhombic, space group *Pmnn,* to monoclinic, space group $P112_1/n$; a subgroup of *Pmnn*. The symmetry along the *c* axis is retained, however the mirror plane and *n*-glide perpendicular to the *a* and *b* axes respectively are lost.

The relationship between phases I and II is more complex. Based on the structure of phase II determined by Byrne & Parsons (2009), the symmetry reduces from orthorhombic to monoclinic. The *b* axis remains the same through the transition, however the *c* axis doubles and the *a* axis more than triples in length indicating a loss of order along these two axes. The number of molecules in the unit cell increases from two in phase I, to twelve in phase II.

Phases II and III are both monoclinic, space group $P2_1/c$. The unit cell volume of phase III is approximately one third of the volume of phase II, with only four molecules in the unit cell. The *b* and *c* axes remain the same, while the *a* axis shortens considerably suggesting ordering along this axis. The β angle increases on transforming from phase II to III.

Phase	*a* / Å	*b* / Å	*c* / Å	Unique angle / °	Volume
I	9.32070(3)	3.733194(11)	5.85253(2)	[$\beta = \gamma = 90$]	203.65(1)
II	30.49	3.81	11.04	β =100.26	1263.14
III	11.26799(10)	3.834114(17)	11.08440(8)	β = 116.9045(6)	427.04(1)
IV	9.32887(2)	3.665170(9)	5.789727(15)	γ = 93.1758(2)	197.66(1)

Table 1.8 Comparison of unit cell parameters for all four phases of pyrazine.

5.5 Conclusions

Pyrazine has been the subject of a variety of studies and has been shown to exhibit three phases in the temperature range 184 – 324 K, however lower temperatures have not previously been studied. Despite the interest in the nature of the phase transitions in pyrazine, structural data are only available for phase I.

The effect of temperature on the crystal structure of pyrazine-d_4 has been investigated in the temperature range 8 – 315 K *via* neutron powder diffraction. At temperatures below 90 K a fourth previously unreported phase is formed which has been designated phase IV. The structure is closely related to that of phase I with a reduction in symmetry from orthorhombic to monoclinic. The crystal structure of pyrazine-III has been determined at 315 K. C-H…N interactions between the molecules result in the formation of a three dimensional network, however the resultant pattern of the C-H…N interactions is different to that observed in phases I and IV.

Indexing and structure solution for pyrazine-II have so far been unsuccessful. Byrne & Parsons (2009) recently determined the structure of phase II by X-ray single crystal diffraction for both pyrazine-h_4 and pyrazine-d_4 however this structure does not correspond to the neutron powder pattern obtained for pyrazine-d_4 thus there appears to be some difference in the behaviour of pyrazine in single crystal and powder form.

The effect of pressure on the crystal structure of pyrazine-d_4 has also been investigated *via* neutron powder diffraction and revealed a phase transition at 0.94 GPa. The phase formed at 0.94 GPa is the same as that observed at low temperatures, phase IV.

5.6 References

Birch, F. (1947). *Physical Review* **71**, 809-824.

Bougeard, D., LeCalve, N. & Novak, A. (1978). *Molecular Crystals and Liquid Crystals* **44**, 113-124.

Boultif, A. & Louer, D. (1994). *J. Appl. Crystallogr.* **24**, 987-993.

Boyd, R. K., Comper, J. & Ferguson, G. (1979). *Can. J. Chem.* **57**, 3056-3060.

Byrne, P. & Parsons, S. (2009). Private communication.

Coelho, A. (2007). *TOPAS-A: General Profile and Structure Analysis Software for Powder Diffraction Data.*

DeWith, G., Harkema, S. & Feil, D. (1976). *Acta Crystallographica* **B32**, 3178-3184.

Fortes, A. D. (2004). PhD thesis, University of London.

Ibberson, R. M. (1996). *J. Appl. Crystallogr.* **29**, 498-500.

Kuznetsov, A. Z., Dmitriev, V., Dubrovinsky, L., Prakapenka, V. & Weber, H. P. (2002). *Solid State Commun.* **122**.

Maehara, M., Kawano, H. & Nibu, Y. (1995). *Bull. Chem. Soc. Jpn.* **68**, 506-511.

Marshall, W. G. & Francis, D. J. (2002). *J. Appl. Crystallogr.* **35**, 122-125.

Miller, R. A. & Schuele, D. E. (1969). *J. Phys. Chem. Solids* **30**, 589-600.

Pawley, G. S. (1981). *J. Appl. Crystallogr.* **14**, 357-361.

Schettino, V., Sbrana, G. & Righini, R. (1972). *Chem. Phys. Lett.* **13**, 284-285.

ShapeSoftware *CRYSCON.* Kingsport, TN.

Waldorf, D. L. & Alers, G. A. (1962). *J. Appl. Phys.* **33**, 3266-3269.

Waldorf, D. L. & Alers, G. A. (19625). *Journal of Applied Physics* **33**, 3266-3269.

Wheatley, P. J. (1957). *Acta Crystallographica* **10**, 182-187.

Chapter 6
Low temperature studies of mesitylene

6.1 Introduction

Mesitylene or 1,3,5-trimethylbenzene, is a well known organic solvent with a relatively low melting point (221 – 228 K) and high boiling point (437 K). However, it is only relatively recently that the structure of solid mesitylene has been thoroughly investigated. Mesitylene is of interest as a potential neutron moderator (Utsuro & Sugimoto, 1977; Unlu *et al.*, 1995) due to the high hydrogen content and weakly hindered methyl group rotations. In order to understand its potential moderator properties it is important to characterise fully the structure and dynamics of the material in the solid state, particularly under operating conditions.

Experimental studies on solid mesitylene have been performed employing a variety of methods including neutron powder diffraction (Natkaniec & Holderna-Natkaniec, 2002), inelastic neutron scattering (Natkaniec *et al.*, 2004), differential scanning calorimetry and Raman spectroscopy (Yamazaki *et al.*, 2000). Temperature induced phase transitions were initially identified based on changes in the Raman spectra and differential scanning calorimetry data (Yamazaki *et al.*, 2000). Neutron powder diffraction studies on perdeutero-mesitylene (mesitylene-d_{12}) subsequently confirmed the presence of three solid phases of mesitylene, referred to as phases I, II & III downwards from the melting point. A fourth phase was observed in a neutron powder diffraction study and complementary X-ray single crystal study (Ibberson *et al.*, 2007). The authors designated this phase IIa.

Recently, the crystal structures of phases I and II were determined; however, only the unit cell was reported for phase III (Ibberson *et al.*, 2007). Phase IIa was reported to be monoclinic with a unit cell volume of 2377 $Å^3$ at 200 K and three independent molecules in the asymmetric unit based on X-ray single crystal measurements. No other structural data were reported for this phase. Figure 6.1 summarises the phase sequence observed by Ibberson *et al via* neutron powder diffraction. The method of characterisation of each phase is summarised in Table 6.1.

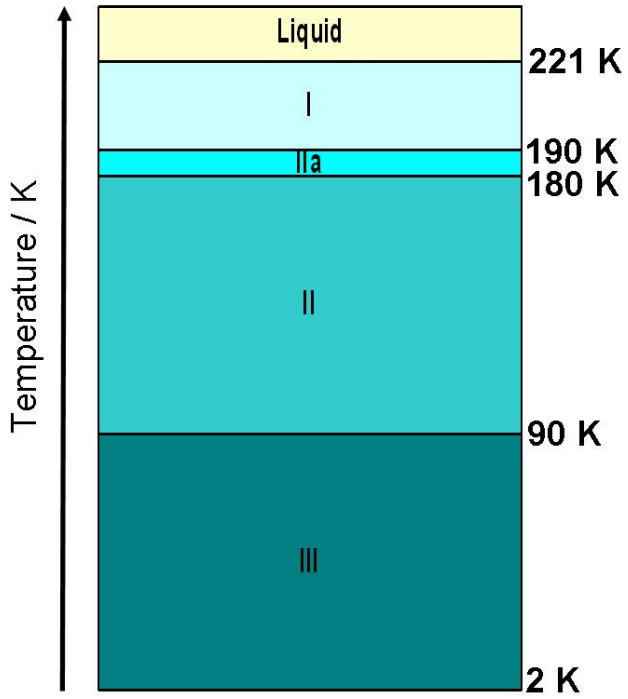

Figure 6.1 Observed phase sequence of mesitylene.

Phase	Method of characterisation	Full structure?
I	Neutron powder diffraction	Yes
II	Neutron powder diffraction	Yes
	X-ray single crystal	Yes
IIa	Neutron powder diffraction	No structural data
	X-ray single crystal	Unit cell volume, crystal system
III	Neutron powder diffraction	Unit cell only

Table 6.1 Characterisation of the phases of mesitylene.

Phase I is cubic with one third of a molecule in the asymmetric unit. The molecules are arranged around a three-fold axis *via* H…H contacts between C(sp^2)-H atoms. Phase II is monoclinic with one molecule in the asymmetric unit. The molecules form layers parallel to the *ab* plane with H…H contacts linking the molecules. The layers are stacked along the *c* axis *via* further H…H contacts. The structure of phase II is discussed in more detail in Section 6.3.1.

One peculiar feature of mesitylene is the effect of cooling rate on the structure obtained; it is possible to stabilise mesitylene in three phases at 2 K depending on the thermal cycle used (Natkaniec & Holderna-Natkaniec, 2002). Samples rapidly quenched in liquid nitrogen crystallise in a mixture of three phases while samples cooled at a rate of 2 K/min tend to crystallise only in phase II. Intermediate cooling rates also produce a mixture of phases.

Phase II can be reversibly transformed to phase III upon cooling. The temperature of the transition depends on the level of deuteration of the sample but is in the region of 90 – 100 K. The transition from phase II to phase I is not reversible - beginning at 190 K - however annealing of the sample at 220 K is required to obtain pure phase I. Once the transition is complete, phase I is stable on cooling down to 2 K. It is also possible to overcool phase II to 2 K in the presence of phase I nucleations.

Differences observed around the melting point in DSC traces recorded at different heating rates have been interpreted as there being three structural modifications of phase I around the melting point (Yamazaki *et al.*, 2000). This is consistent with three melting points, 221, 223 and 228 K, reported in the literature (Dictionary of Organic Compounds, 1996) but not with Raman and powder diffraction experiments which indicate only one structure.

The results of several X-ray single crystal experiments on both perhydro-mesitylene (mesitylene-h_{12}) and perdeutero-mesitlyene (mesitylene-d_{12}) are presented including the crystal structure of phase III. The structure of a previously unknown phase which was obtained under the same crystallisation conditions as phase II is also reported.

6.2 Experimental

Mesitylene-h_{12} and mesitylene-d_{12} were obtained from Aldrich and used as received.

6.2.1 Crystal Growth

Mesitylene was drawn into a capillary and flame sealed. A polycrystalline mass was obtained by flash freezing with liquid nitrogen. Typically there are two methods for growing a single crystal in situ; either through careful control of the temperature or using the laser assisted zone refinement method of Boese & Nussbaumer (1994). Crystals of mesitylene were grown through careful control of the temperature. A single crystal was obtained by raising the temperature to 221 K allowing the sample to melt until only one seed crystallite remained. The sample was then allowed to cool slowly to 215 K. Data were collected at 215 K before cooling the crystal for further data collections. Several single crystals were grown for both mesitylene-h_{12} and mesitylene-d_{12} using this procedure. Two different phases, II and a previously unknown phase which we have designated phase IV, were obtained at 215 K for both compounds under the same crystallisation conditions in different experiments.

Upon cooling a crystal of mesitylene-d_{12} phase II to 95 K the crystal broke into several components. Attempts to index the sample were unsuccessful therefore the experiment was repeated. On the second attempt, a transition to phase III was observed when cooled to 90 K, though the resulting crystal was twinned. No phase transition was observed upon cooling mesitylene-h_{12} to 88 K.

No phase transition was observed upon cooling a crystal of phase IV to 90 K.

Table 6.2 summarises data collection temperatures and structure obtained for each experiment. In all cases, heating the sample above 221 K resulted in the sample melting with no transition to phase I observed.

Phase grown	Data collection temperatures / K	Phase transition?
Mesitylene-h_{12}		
II	215, 150, 88	No
IV	215, 150, 90, 221	No
Mesitylene-d_{12}		
II	215, 150, 95	95 K crystal broke into several components
	215, 90	90 K transition to phase III
IV	215, 150	No

Table 6.2 Summary of data collection temperatures and structures obtained for mesitylene-h_{12} and mesitylene-d_{12}.

6.2.2 Data collection and refinement

Diffraction data were collected on a Bruker SMART APEX diffractometer with graphite-monochromated Mo-Kα radiation. Data were integrated using the program SAINT (Bruker-Nonius, 2006) and absorption corrections carried out with the program SADABS (Sheldrick, 2004). All structures were solved by direct methods using SIR-92 (Altomare *et al.*, 1994) and refined against $|F|^2$ using CRYSTALS (Betteridge *et al.*, 2003). Hydrogen atoms were placed geometrically and initially refined with restraints to determine the orientation of the methyl groups before being constrained to ride on their host atoms with $U_{iso}(H) = 1.2U_{eq}(C_{sp2})$ and $U_{iso}(H) = 1.5U_{eq}(C_{sp3})$. C-H bond lengths used were based on the data collection temperature and are summarised in Table 6.3. Crystal and refinement data are listed in Tables 6.4 - 6.7.

Temperature / K	Aromatic / Å	Methyl / Å
221	0.94	0.97
215	0.94	0.97
150	0.95	0.98
90	0.95	0.98

Table 6.3 C-H distances for aromatic and methyl groups.

A consistent numbering scheme was used for all structures and is given in Scheme 6.1. As two of the structures reported here have more than one molecule in the asymmetric unit, suffixes of 1, 2 and 3 was added to the standard numbering scheme to identify individual molecules in the asymmetric unit.

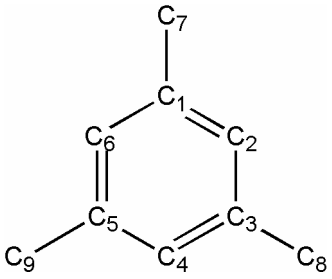

Scheme 6.1 Standard numbering scheme for mesitylene.

Mesitylene-h_{12} II			
Temperature	**215 K**	**150 K**	**88 K**
Crystal data			
Chemical formula	C_9H_{12}	C_9H_{12}	C_9H_{12}
M_r	120.19	120.19	120.19
Cell setting, space group	Monoclinic, $P2_1/c$	Monoclinic, $P2_1/c$	Monoclinic, $P2_1/c$
a, b, c (Å)	8.3424 (15), 13.597 (2), 7.6808 (13)	8.3240 (3), 13.4657 (4), 7.6082 (2)	8.3196 (7), 13.3607 (10), 7.5723 (6)
β (°)	114.860 (12)	114.925 (2)	115.073 (4)
V (Å^3)	790.5 (2)	773.36 (4)	762.39 (11)
Z	4	4	4
D_x (Mg m^{-3})	1.010	1.032	1.047
Radiation type	Mo $K\alpha$	Mo $K\alpha$	Mo $K\alpha$
μ (mm^{-1})	0.06	0.06	0.06
Crystal form, colour	Cylinder, colourless	Cylinder, colourless	Cylinder, colourless
Crystal size (mm)	1.00 × 0.30 × 0.30	1.00 × 0.30 × 0.30	1.00 × 0.30 × 0.30
Data collection			
T_{min}, T_{max}	0.69, 0.98	0.81, 0.98	0.73, 0.98
No. of measured, independent and observed reflections	6395, 1622, 832	8401, 1586, 1533	8350, 1568, 1371
Criterion for observed reflections	$I > 2.0\sigma(I)$	$I > 2.0\sigma(I)$	$I > 2.0\sigma(I)$
R_{int}	0.058	0.033	0.056
θ_{max} (°)	26.4	26.4	26.4
Refinement			
$R[F^2 > 2\sigma(F^2)]$, $wR(F^2)$, S	0.084, 0.255, 1.05	0.092, 0.222, 1.07	0.101, 0.216, 1.07
No. of relections	1622	1585	1567
No. of parameters	82	82	82
Weighting scheme a, b*	0.11, 0.32	0.09, 0.79	0.06, 1.43
$\Delta\rho_{max}$, $\Delta\rho_{min}$ (e Å^{-3})	0.26, –0.45	0.38, –0.31	0.45, –0.40

* where $w = 1/[\sigma^2(F^2) + aP^2 + bP]$, $P = (\max(F_o^2,0) + 2F_c^2)/3$

Table 6.4 Crystal and refinement data for mesitylene-h_{12} phase II.

	Mesitylene-d_{12} II			Mesitylene-d_{12} III
Temperature	**215 K**	**150 K**	**215 K**	**90 K**
Crystal data				
Chemical formula	C_9D_{12}	C_9D_{12}	C_9D_{12}	C_9D_{12}
M_r	132.21	132.21	132.21	132.21
Cell setting, space group	Monoclinic, $P2_1/c$	Monoclinic, $P2_1/c$	Monoclinic, $P2_1/c$	Triclinic, P-1
a, b, c (Å)	8.3426 (7), 13.5874 (11), 7.6866 (6)	8.3211 (3), 13.4550 (4), 7.6136 (2)	8.3423 (10), 13.5619 (16), 7.6743 (10)	8.4775 (14), 12.8653 (19), 7.7219 (13)
α, β, γ (°)	90, 114.928 (5), 90	90, 114.991 (2), 90	90, 115.006 (10), 90	92.732 (11), 116.745 (10), 95.956 (11)
V (Å^3)	790.14 (12)	772.61 (4)	786.86 (18)	743.8 (2)
Z	4	4	4	4
D_x (Mg m^{-3})	1.111	1.137	1.015	1.18
Radiation type	Mo $K\alpha$	Mo $K\alpha$	Mo $K\alpha$	Mo $K\alpha$
μ (mm^{-1})	0.06	0.06	0.06	0.06
Crystal form, colour	Cylinder, colourless	Cylinder, colourless	Cylinder, colourless	Cylinder, colourless
Crystal size (mm)	1.00 × 0.31 × 0.31	1.00 × 0.31 × 0.31	1.00 × 0.30 × 0.30	1.00 × 0.30 × 0.30
Data collection				
T_{min}, T_{max}	0.81, 0.98	0.78, 0.98	0.81, 0.98	0.71, 0.98
No. of measured, independent and observed reflections	9098, 1621, 1087	10744, 1580, 1408	6446, 1617, 837	3011, 3011, 1077
Criterion for observed reflections	$I > 2.0\sigma(I)$	$I > 2.0\sigma(I)$	$I > 2.0\sigma(I)$	$I > 2.0\sigma(I)$
R_{int}	0.053	0.033	0.048	
θ_{max} (°)	26.4	26.4	26.4	25.2
Refinement				
$R[F^2 > 2\sigma(F^2)]$, $wR(F^2)$, S	0.075, 0.246, 1.16	0.072, 0.211, 1.08	0.071, 0.241, 1.13	0.086, 0.293, 1.01
No. of relections	1620	1580	1616	2679
No. of parameters	82	82	82	164
Weighting scheme a, b*	0.09, 0.25	0.09, 0.45	0.08, 0.37	0.15, 0.0
$\Delta\rho_{max}$, $\Delta\rho_{min}$ (e Å^{-3})	0.32, –0.27	0.31, –0.31	0.40, –0.36	0.42, –0.22

* where $w = 1/[\sigma^2(F^2) + aP^2 + bP]$, $P = (\max(F_o^2,0) + 2F_c^2)/3$

Table 6.5 Crystal and refinement data for mesitylene-d_{12} phase II & III.

	Mesitylene-h_{12} IV			
Temperature	**215 K**	**150 K**	**90 K**	**221 K**
Crystal data				
Chemical formula	C_9H_{12}	C_9H_{12}	C_9H_{12}	C_9H_{12}
M_r	120.19	120.19	120.19	120.19
Cell setting, space group	Monoclinic, *P*2/*c*	Monoclinic, *P*2/*c*	Monoclinic, *P*2/*c*	Monoclinic, *P*2/*c*
a, *b*, *c* (Å)	17.2427 (5), 4.97440 (10), 28.3090 (9)	17.1414 (6), 4.9366 (2), 28.0850 (11)	17.0565 (5), 4.91240 (10), 27.9461 (8)	17.2482 (6), 4.9736 (2), 28.3238 (9)
β (°)	100.654 (2)	100.292 (3)	100.056 (2)	100.688 (2)
V (Å^3)	2386.26 (11)	2338.32 (16)	2305.59 (11)	2387.62 (15)
Z	12	12	12	12
D_x (Mg m^{-3})	1.004	1.024	1.039	1.003
Radiation type	Mo *K*α	Mo *K*α	Mo *K*α	Mo *K*α
μ (mm^{-1})	0.06	0.06	0.06	0.06
Crystal form, colour	Cylinder, colourless	Cylinder, colourless	Cylinder, colourless	Cylinder, colourless
Crystal size (mm)	0.80 × 0.30 × 0.30	0.80 × 0.30 × 0.30	0.80 × 0.30 × 0.30	0.80 × 0.30 × 0.30
Data collection				
T_{min}, T_{max}	0.82, 0.98	0.77, 0.98	0.81, 0.98	0.80, 0.98
No. of measured, independent and observed reflections	32545, 4884, 2618	21676, 4775, 2682	21305, 4710, 3326	31645, 4890, 2508
Criterion for observed reflections	$I > 2.0\sigma(I)$	$I > 2.0\sigma(I)$	$I > 2.0\sigma(I)$	$I > 2.0\sigma(I)$
R_{int}	0.055	0.062	0.047	0.058
θ_{max} (°)	26.4	26.4	26.4	26.4
Refinement				
$R[F^2 > 2\sigma(F^2)]$, $wR(F^2)$, S	0.063, 0.194, 0.92	0.060, 0.173, 0.91	0.064, 0.178, 0.96	0.062, 0.198, 0.89
No. of relections	4872	4775	4698	4890
No. of parameters	244	244	244	244
Weighting scheme a, b*	0.11, 0.35	0.08, 1.12	0.09, 1.66	0.11, 0.39
$\Delta\rho_{max}$, $\Delta\rho_{min}$ (e Å^{-3})	0.35, –0.35	0.26, –0.23	0.33, –0.36	0.38, –0.29

* where $w = 1/[\sigma^2(F^2) + aP^2 + bP]$, $P = (\max(F_o^2,0) + 2F_c^2)/3$

Table 6.6 Crystal and refinement data for mesitylene-h_{12} phase IV.

	Mesitylene-d_{12} IV	
Temperature	**215 K**	**150 K**
Crystal data		
Chemical formula	C_9D_{12}	C_9D_{12}
M_r	132.21	132.21
Cell setting, space group	Monoclinic, *P*2/*c*	Monoclinic, *P*2/*c*
a, *b*, *c* (Å)	17.2171 (5), 4.96810 (10), 28.2639 (8)	17.1270 (5), 4.93000 (10), 28.0497 (8)
β (°)	100.654 (2)	100.312 (2)
V (Å^3)	2375.91 (11)	2330.15 (11)
Z	12	12
D_x (Mg m^{-3})	1.109	1.131
Radiation type	Mo $K\alpha$	Mo $K\alpha$
μ (mm^{-1})	0.06	0.06
Crystal form, colour	Cylinder, colourless	Cylinder, colourless
Crystal size (mm)	1.00 × 0.31 × 0.31	1.00 × 0.31 × 0.31
Data collection		
T_{min}, T_{max}	0.79, 0.98	0.79, 0.98
No. of measured, independent and observed reflections	4872, 4872, 2454	4775, 4775, 2977
Criterion for observed reflections	$I > 2.0\sigma(I)$	$I > 2.0\sigma(I)$
R_{int}	0.062	0.053
θ_{max} (°)	26.4	26.4
Refinement		
$R[F^2 > 2\sigma(F^2)]$, $wR(F^2)$, S	0.071, 0.217, 0.87	0.064, 0.195, 0.92
No. of relections	4872	4775
No. of parameters	244	244
Weighting scheme a, b*	0.12, 0.82	0.12, 0.57
$\Delta\rho_{max}$, $\Delta\rho_{min}$ (e Å^{-3})	0.38, –0.39	0.39, –0.34

* where $w = 1/[\sigma^2(F^2) + aP^2 + bP]$, $P = (\max(F_o^2,0) + 2F_c^2)/3$

Table 6.7 Crystal and refinement data for mesitylene-d_{12} phase IV.

6.2.3 Differential Scanning Calorimetry

Differential scanning calorimetry (DSC) traces were recorded using a Perkin Elmer Pyris 1 DSC instrument with the samples contained in closed aluminium pans. All samples were loaded at room temperature and were initially cooled and then heated. Several independent experimental runs were performed under different conditions as the cooling rate is known to affect the phase transitions observed in mesitylene. The temperature ranges and heating/cooling rates used are listed in Table 6.8.

	Scan rate / $Kmin^{-1}$	Cool to / K	Heat to / K
Mesitylene-h_{12}	2	104	296
	5	101	287
	10	102	291
	20	101	286
	100	102	285
Mesitylene-d_{12}	2	104	296
	5	101	287
	10	101	291
	20	101	286
	100	105	281

Table 6.8 DSC temperature ranges collected and scan rate for mesitylene-h_{12} and mesitylene-d_{12}.

6.2.4 PIXEL calculations

The final crystal structures obtained were used to calculate the molecular electron density. Standard quantum mechanical methods using GAUSSIAN03 (Frisch *et al.*, 2004) at the MP2/6-31G** level of theory were used. Lattice energy calculations for phases II and III were performed using PIXEL, part of the OPiX package (Gavezzotti, 2003), using a cluster of molecules of radius 18 Å. These calculations yield the total lattice energy and a breakdown into the Coulombic, polarization, dispersion and repulsion components (Dunitz & Gavezzotti, 2005). Calculations on various dimer interactions of interest in all phases were also performed.

6.3 Results

Previous neutron powder diffraction studies have shown mesitylene to exhibit three phases, referred to as I, II and III downwards from the melting point. The structures of phases I and II are known, however only unit cell dimensions were known for phase III. Complementary X-ray single crystal studies confirmed the presence of a fourth phase, referred to as IIa (Ibberson *et al.*, 2007).

Two phases have been obtained at 215 K from the same crystallisation conditions for both mesitylene-h_{12} and mesitylene-d_{12}; phase II and previously unknown phase which we have designated phase IV. Upon cooling a single crystal of mesitylene-d_{12} in phase II to 90 K, a transition to phase III was observed. The full structure of phase III is reported for the first time.

When heating a crystal of phase II, the sample melted directly from this phase at 221 K without transforming to phase I. Phase IV did not exhibit any phase transitions upon cooling to 90 K and also melted directly from this phase when heated to 221 K. Phase I was not obtained in any of the crystallisations.

6.3.1 Phase II

The structure of phase II has previously been solved from neutron powder diffraction and X-ray single crystal studies (Ibberson *et al.*, 2007) and a description is included here to allow comparison with phase III. The structure is monoclinic, space group $P2_1/c$ with one molecule in the asymmetric unit.

The molecules pack to form layers parallel to the *ab* plane, Figure 6.2a. Within the layers the molecules are linked by H…H contacts of 2.44 and 2.82 Å at 150 K (X-ray hydrogen distances). The layers are slightly sinusoidal (Figure 6.2b) with an angle of 12.65 ° between the planes of the molecules. The layers stack on top of each other along the *c* axis with H…H contacts of 2.34 and 2.51 Å between methyl groups. The layers are offset such that the methyl groups do not lie directly above each other as shown in Figure 6.2c.

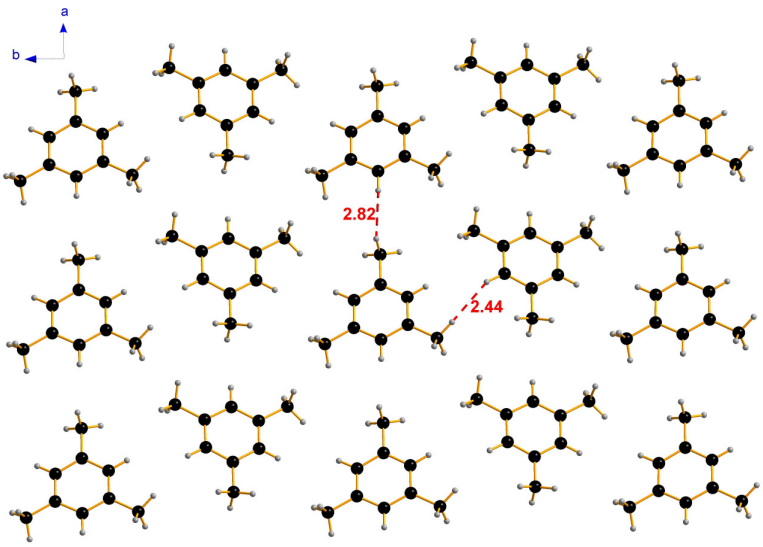

(a) H..H contacts link the molecules to form layers (Distances given in Å)

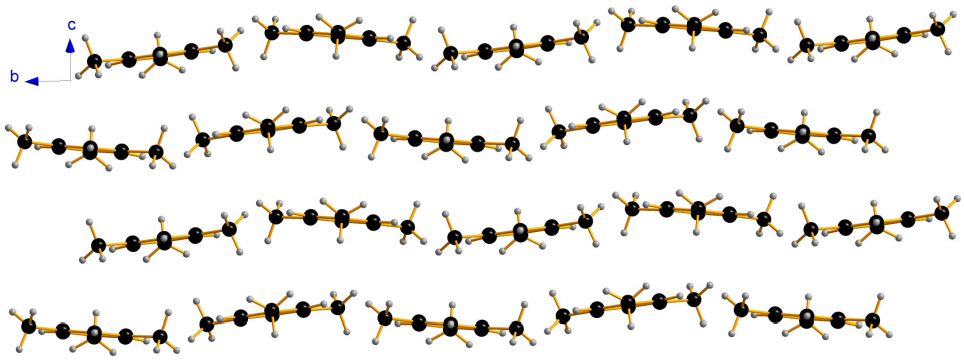

(b) Layers stack along the *c* axis

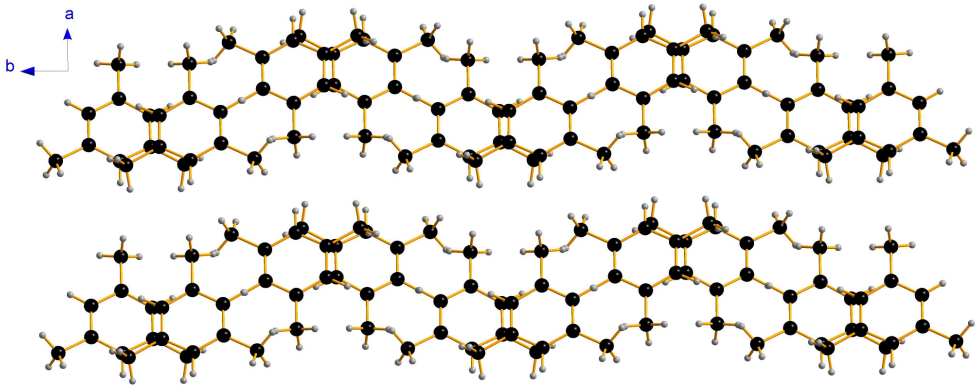

(c) No overlay of methyl groups

Figure 6.2 Packing of molecules in mesitylene phase II.

6.3.2 Phase III

Phase III is triclinic, space group *P*-1, with two molecules in the asymmetric unit. As in phase II, the molecules pack to form layers parallel to the *ab* plane. The two independent molecules alternate along the *b* axis within the layers, with successive pairs of molecules related by simple translation. The molecules are twisted around compared to phase II, resulting in the lengthening of some H…H contacts and shortening of others, Figure 6.3. The shortest H…H contacts linking the layers together are 2.41 and 2.48 Å. The layers are more sinusoidal than in phase II, with an angle of 17.54 ° between the planes of the molecules. As in phase II, the layers are stacked along the *c* axis with H…H contacts between methyl groups of 2.48 and 2.64 Å.

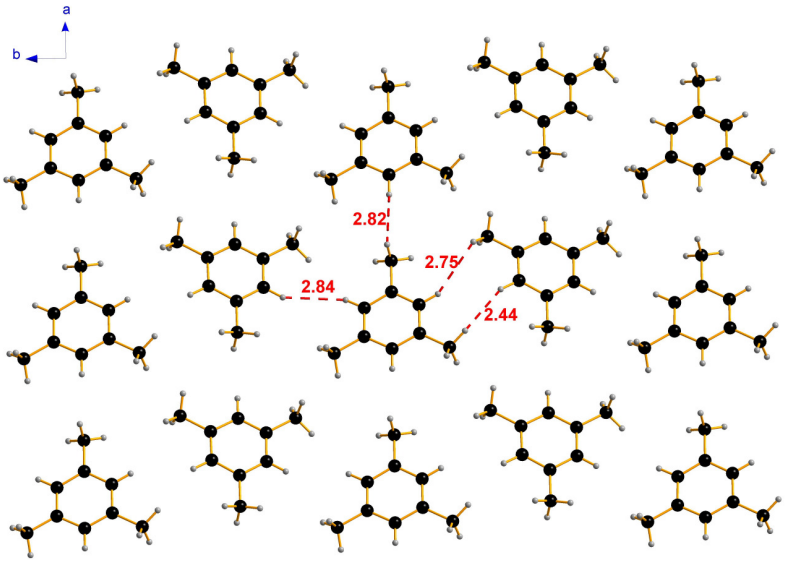

(a) Phase II 150 K (replica of Figure 6.2a but included for ease of comparison with Figure 6.3b)

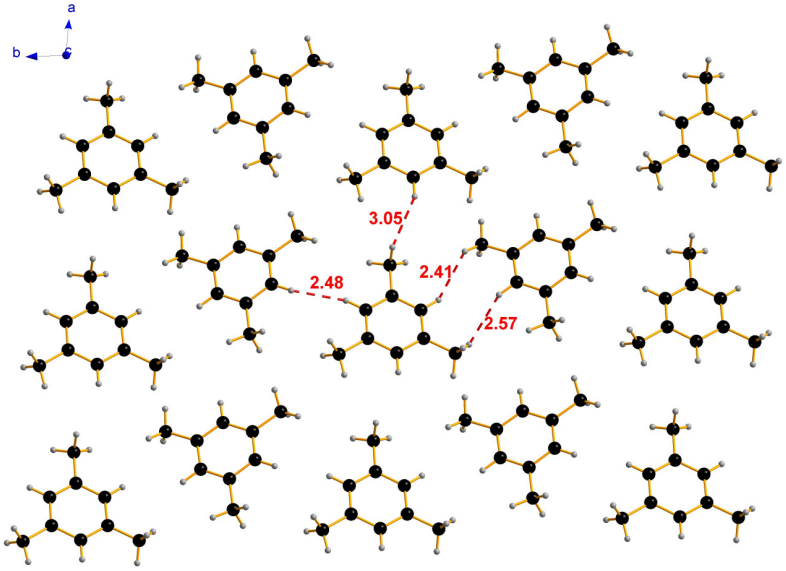

(b) Phase III 90 K

Figure 6.3 Layers in phase II and III. All distances given in Å.

6.3.3 Phase IV

The structure of phase IV is monoclinic, space group *P*2/*c* with three molecules in the asymmetric unit. The main structural feature is a cone arrangement formed by two of the independent molecules as shown in Figure 6.4. Within the cones, the molecules are related by a 2-fold axis.

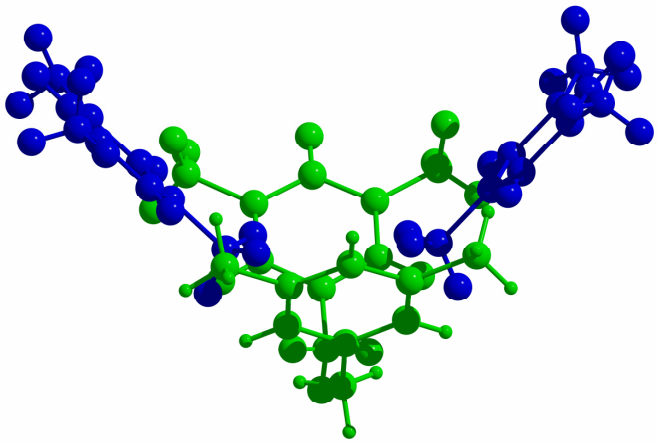

Figure 6.4 Cone arrangement formed by molecules one and two. Coloured by symmetry equivalence (green molecule 1 based on C11, blue molecule 2 based on C12).

Simple translation along the *b* axis forms stacks of cones parallel to the *b* axis. Neighbouring stacks along the *c* axis are related by the glide plane.

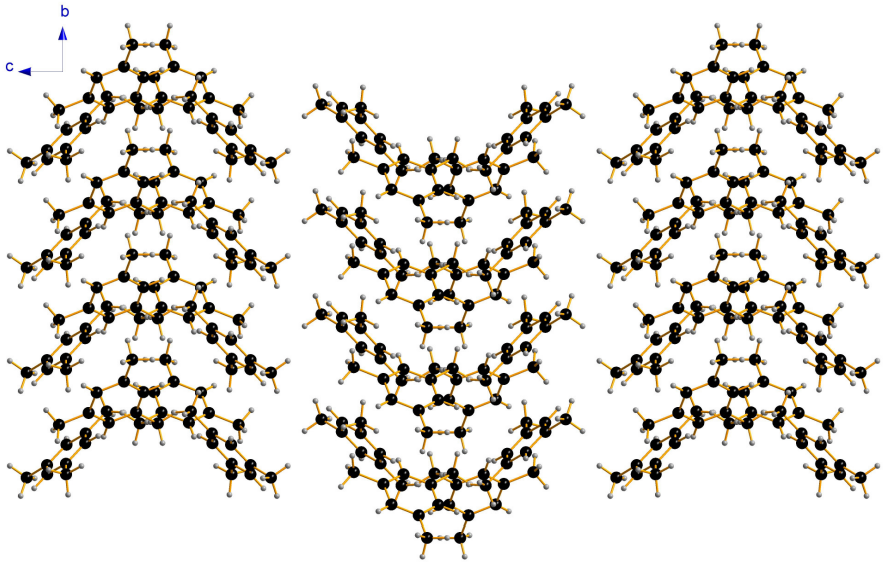

Figure 6.5 Stacks of cones formed by simple translation along the *b* axis. Neighbouring stacks are related by glide plane.

The third independent molecule sits in the spaces between the cones formed by the other two independent molecules, highlighted in red in Figure 6.6.

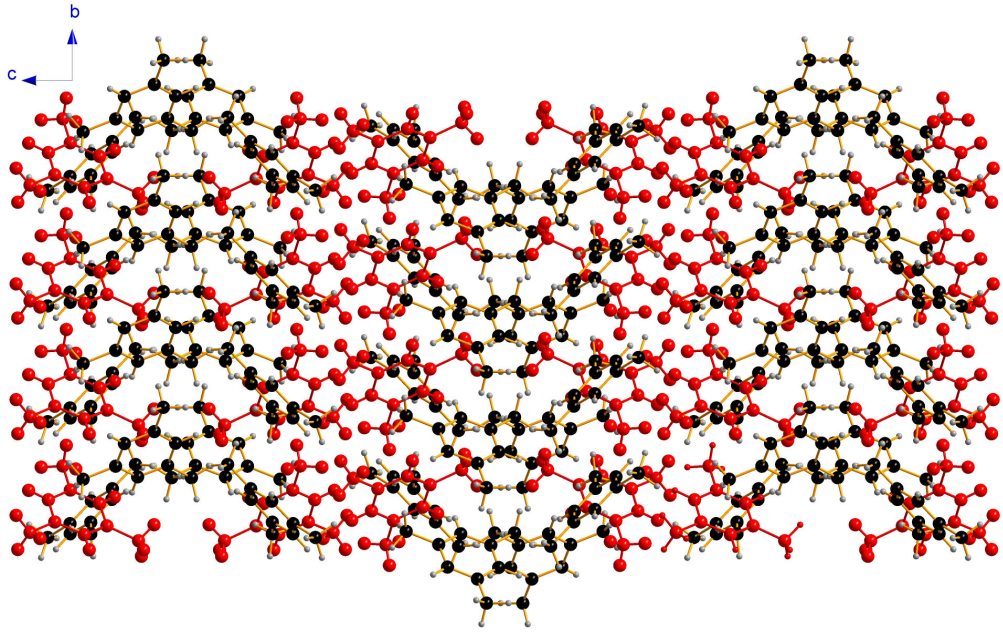

Figure 6.6 The third independent molecule, highlighted in red, sits in the spaces between cones.

The position of these molecules is such that they form zig-zag chains with molecule one as shown in Figure 6.7.

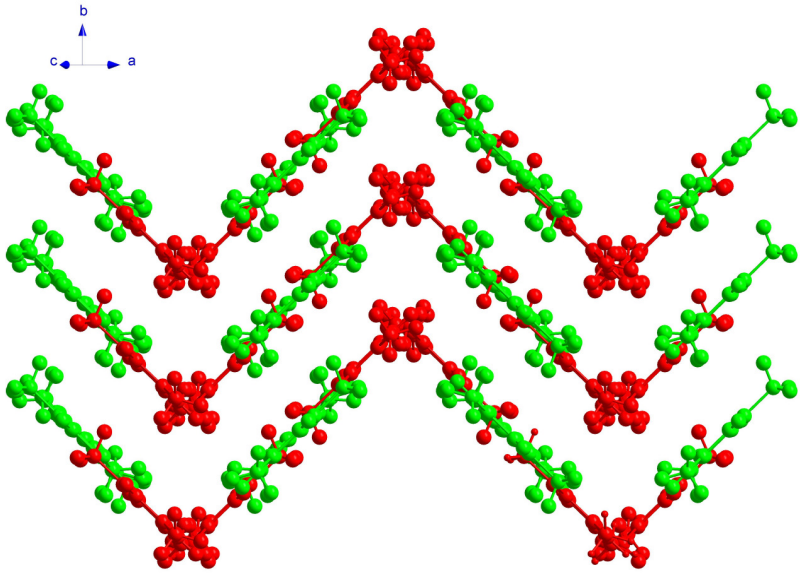

Figure 6.7 Zig-zig chains formed by molecules one and three, viewed along 101 axis. Coloured by symmetry equivalence (green molecule one, red molecule three).

All three independent molecules are stacked along the *b* axis forming C-H…π interactions (Table 6.9), linking the layers together.

Molecule	C…π / Å	H…π / Å	Angle C-H… π / °
1	3.543(2)	2.60	163
2	3.563(2)	2.61	164
3	3.575(3)	2.63	161

Table 6.9 C-H… π interactions in mesitylene phase IV.

6.3.4 Differential Scanning Calorimetry

Differential scanning calorimetry (DSC) traces were recorded for both mesitylene-h_{12} and mesitylene-d_{12} using a variety of heating / cooling rates as this is known to affect the phases obtained. Multiple traces under the same experimental conditions were recorded on the same sample however this did not have any influence on the trace obtained, thus once the sample has melted previous thermal cycles appear to have no influence. Overall, two different types of trace were obtained.

Figure 6.8 is typical of the most common type of trace obtained. Scan rates of 2, 5, 10 and 20 K/min for both mesitylene-h_{12} and mesitylene-d_{12} and 100 K/min for mesitylene-d_{12} produced this type of trace. On cooling a sharp transition is observed in the region 182-191 K due to crystallisation of the sample. The exact temperature of crystallisation depended on the cooling rate, though in general, faster cooling rates resulted in a lower crystallisation temperature. In all cases, the crystallisation temperature is lower than the usual freezing point of mesitylene as supercooling is a common feature of DSC experiments. The only feature of the heating cycle is the sample melting at 221 K. In some of the traces there was a shoulder on the melting peak which is likely to be due to inhomogeneities in the sample caused by the sample being unevenly distributed in the sample pan. This feature has been observed in other compounds including pyridine (Parsons, 2009). There is no evidence of any phase transitions as there are no other peaks or troughs in the DSC trace. The single melting peak suggests that the sample crystallised into a single phase which did not undergo any phase transitions in the temperature range examined, thus on the basis

of the crystallisation experiments above it may have crystallised into either phase II or phase IV. The single crystal experiments cannot help with phase discrimination since samples melted directly from both phase II and IV; a transition to phase I was not observed.

The transition to phase III at 90-100 K would differentiate between the two possibilities; however, the instrument was only able to cool to ~100 K therefore any such transition could not be observed.

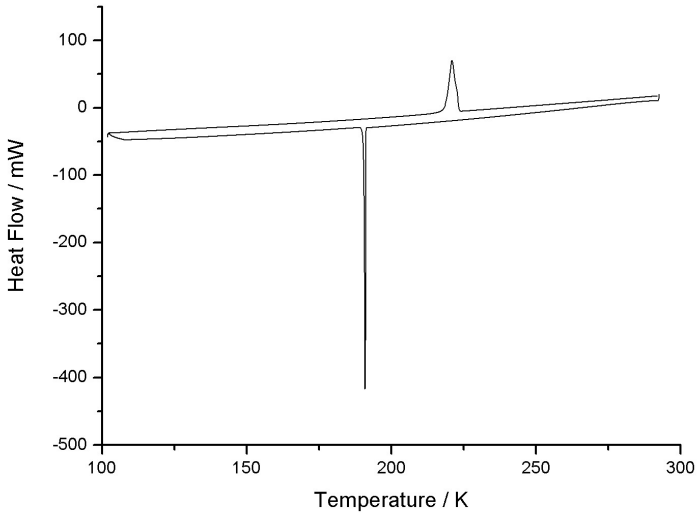

Figure 6.8 Typical DSC trace obtained for slow scan rates of mesitylene-h_{12} and mesitylene-d_{12}.

The second type of DSC trace shown in Figure 6.9 was obtained for mesitylene-h_{12} at 100 K/min. On cooling the sample began to crystallise at 181 K though the transition is much broader than seen in other traces. At 158 K on cooling there is a small trough which could be due to a solid-solid transition. There is also an additional feature in the heating cycle. A small trough occurs at 200 K, prior to the main melting peak at 221 K. The melting peak is quite broad which may indicate several different melting temperatures. Yamazaki *et al.* (2000) observed an exothermic transition at 188 K which they ascribed to the transition II → I and in some traces a pre-melting

exothermic event at ~200 K. Due to the fast heating rate used, the trough at 200 K observed in our trace could correspond to either of these transitions by Yamazaki *et al.* The more complicated nature of this type of DSC trace is consistent with observations that rapidly quenched samples crystallise into a mixture of phases.

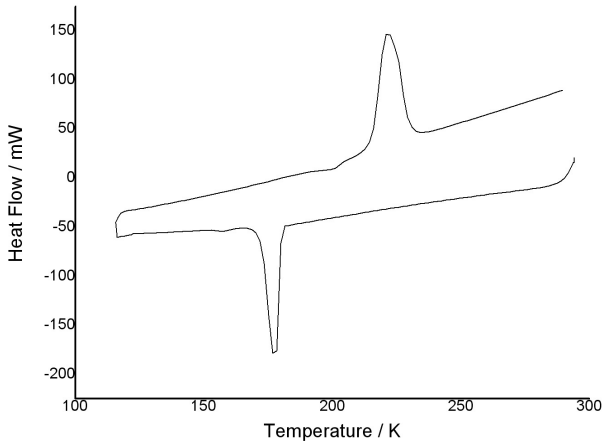

Figure 6.9 DSC trace obtained for mesitylene-h_{12} at 100 K/min.

These DSC experiments show that the heating and cooling rate does affect the temperature induced behaviour of mesitylene. There is some difference between the behaviour of mesitylene-h_{12} and mesitylene-d_{12} under rapid heating and cooling conditions. The most significant difference between the two types of trace obtained is in transitions observed.

Under the conditions of these experiments we would not have been able to observe the transition observed by Yamazaki *et al.* (2000) at 91 K which has been ascribed to transformations between phases II and III. They also observed a second subtle transition at 188 K which we have observed for mesitylene-h_{12} when heated at 100 K/min. Yamazaki *et al* used heating rates in the range 0.5-5 K/min and sample weights greater than ours which will have some influence on the trace obtained.

6.4 Discussion

6.4.1 Comparison of Phases II & III

As mentioned above, the crystal structures of phases II and III are very similar. Both structures consist of layers parallel to the *ab* plane, however the difference between the structures is in the orientation of the molecules within the layers, Figure 6.10. In phase II, the molecules are lined up such that, when translated along the *a* axis, a methyl group C-C bond on one molecule is directly in line with a C(sp2)-H bond on the next molecule. In phase III however, the molecules have twisted round so they do not line up, highlighted in red. This results in the methyl groups on neighbouring molecules moving closer together, circled in blue. This change results in two independent molecules and as such the interactions with the molecules on either side are now different.

In phase III the molecules have twisted further out of the *ab* plane, resulting in the layers being more sinusoidal than those in phase II as shown in Figure 6.11. The angle between the planes of the molecules increases from 12.5° in phase II to 17.5° in phase III.

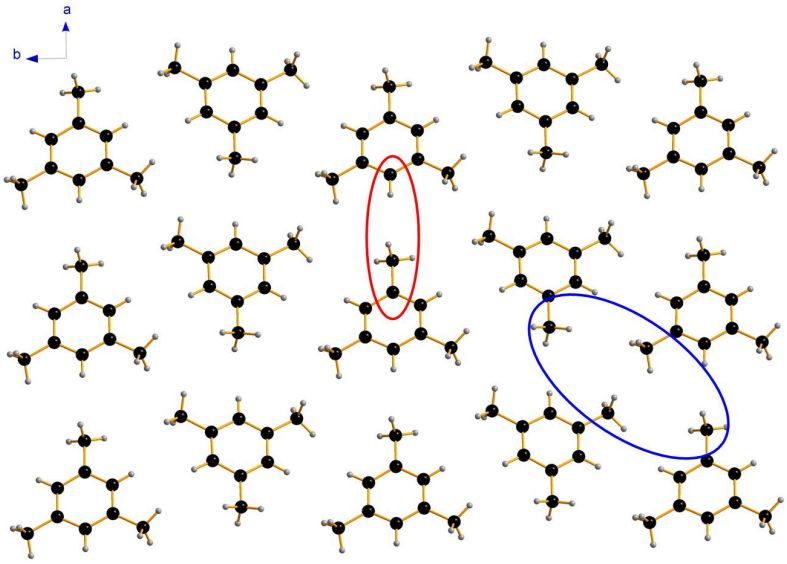

(a) Phase II

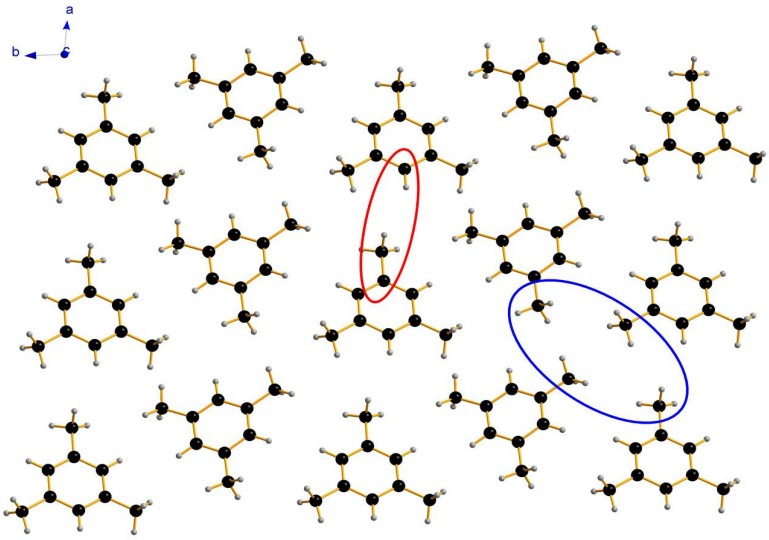

(b) Phase III

Figure 6.10 Layers of mesitylene molecules in phases II & III.

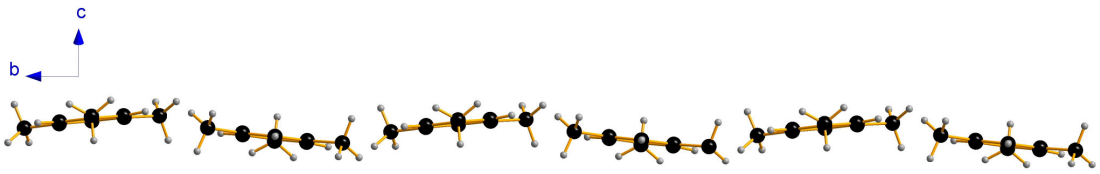

(a) Phase II

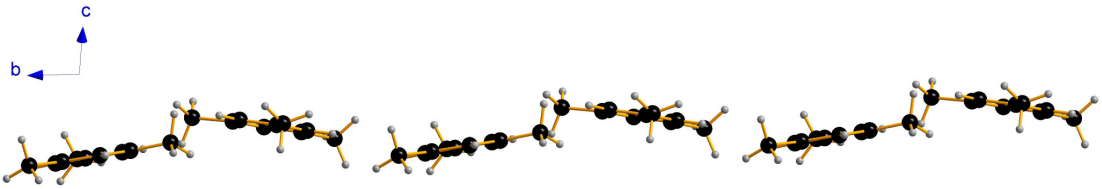

(b) Phase III

Figure 6.11 Sinusoidal layers in phases II & III.

PIXEL calculations on the various dimer interactions present in these structures indicate that this change in orientation of the molecules does not have a significant effect on the energy of the interactions within the layers, Table 6.10. There are small increases and decreases in individual interaction energies, however these calculations indicate that overall the interactions within the layers are likely to be stronger in phase III.

Similar calculations on the interactions between the layers show there are two interactions between the layers (Table 6.11) which are much higher in energy than those within the layers, the strongest being the C-H…π interaction labelled F in Figure 6.12. On transforming to phase III, the C-H… π interaction becomes slightly less favourable (phase II -20.6 kJ mol^{-1}, phase III -19.4 & -19.5 kJ mol^{-1}) however the other interaction becomes more stable (phase II -11.6 kJ mol^{-1}, phase III -15.6 & -13.5 kJ mol^{-1}) thus overall the transition will be favourable.

Indeed, PIXEL calculations of the total lattice energy, Table 6.12, show that phase III (90 K) is more stable than phase II (88 K).

Interaction	Phase	Centroid-Centroid distance	Coulombic	Dispersion	Repulsion	Polarisation	Total
A	II	8.32	-0.3	-5.3	1.3	-0.1	-4.6
	III	8.48	-0.1	-5.2	1.2	-0.1	-4.2
		8.48	-0.1	-5.5	1.4	-0.1	-4.4
B	II	7.04	-0.8	-12.4	4.4	-0.6	-9.5
	III	6.84	-0.7	-13.8	4.4	-0.5	-10.7
		6.84	-0.7	-13.7	4.4	-0.5	-10.5
C	II	7.04	-0.8	-12.4	4.4	-0.6	-9.5
	III	6.86	-1.6	-15.4	6.4	-0.8	-11.4
		6.86	-1.6	-15.1	6.4	-0.8	-11.1
D	II	9.14	-0.5	-5.0	2.5	-0.2	-3.0
	III	9.64	-0.1	-3.1	0.6	0.0	-2.6
		9.64	-0.1	-3.1	0.6	0.0	-2.6
E	II	9.14	-0.5	-5.0	2.5	-0.2	-3.0
	III	8.40	-0.8	-7.1	3.6	-0.4	-4.6
		8.40	-0.8	-7.0	3.6	-0.4	-4.5

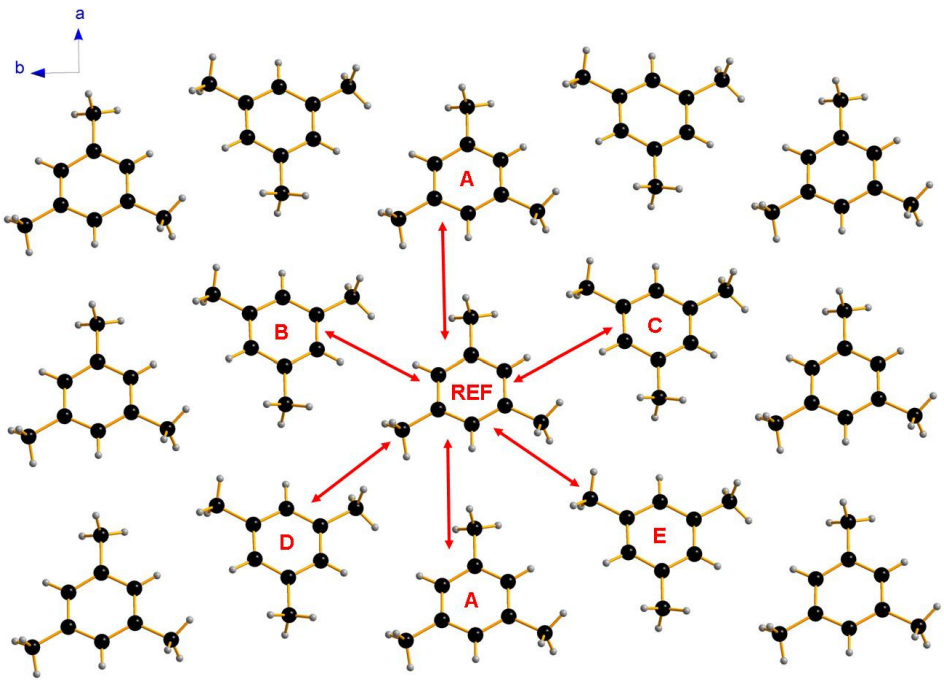

Table 6.10 Components of the interaction energy and total interaction energy for various dimer interactions within the layers. Two sets of values are quoted for phase III as there are two independent molecules. Energies are per dimer in kJ mol^{-1}. Centroid-centroid distance in Å.

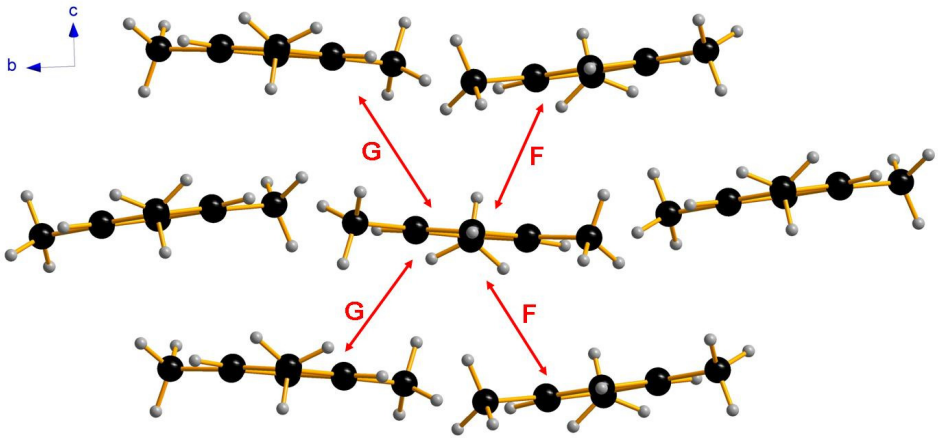

Figure 6.11 Stacking interactions in phases II & III.

Interaction	Phase	Centroid-Centroid distance	Coulombic	Dispersion	Repulsion	Polarisation	Total
F	II	4.61	-6.5	-31.8	21.1	-3.4	-20.6
	III	4.72	-4.6	-26.6	14.3	-2.4	-19.4
		4.61	-6.1	-31.4	21.4	-3.3	-19.5
G	II	5.78	-1.1	-12.7	2.7	-0.4	-11.6
	III	5.89	-3.9	-21.1	10.9	-1.5	-15.6
		5.64	-2.8	-16.2	6.6	-1.0	-13.5

Table 6.11 Components of the interaction energy and total interaction energy for dimer interactions between layers. Two sets of values are quoted for phase III as there are two independent molecules. Energies are per dimer in kJ mol^{-1}. Centroid-centroid distance in Å.

	Coulombic	Dispersion	Repulsion	Polarisation	U
Phase II	-17.5	-90.0	61.6	-9.5	-55.5
Phase III	-18.5	-94.4	59.9	-8.1	-61.0

Table 6.12 Components of the lattice energy and the total lattice energy, U, for phases II and III of mesitylene. Energies are per molecule in kJ mol^{-1}.

6.4.2 Phase IV

The structure of phase IV is rather complicated as there are three independent molecules and does not bear much resemblance to phase II, though it was formed under the same conditions as phase II and has been found to be stable down to 90 K. Given the significant difference between the structure of phase IV and phase II, it would be unlikely for phase IV to transform to phase II or III and indeed this has been confirmed in practice.

Ibberson *et al.* (2007) observed the formation of a fourth phase of mesitylene in both X-ray single crystal and neutron powder diffraction studies which they designated phase IIa. The structure was reported to be monoclinic with a unit cell volume of 2377 $Å^3$ at 200 K and three independent molecules in the asymmetric unit based on X-ray single crystal measurements. No other structural data were reported. This description is consistent with phase IV reported here however the neutron powder pattern obtained at 180 K does not correspond to phase IV. This means that phase IV has never been observed in neutron powder studies. Whilst this unknown pattern has only been observed on one occasion, its presence indicates the existence of a fifth phase of mesitylene.

As full PIXEL calculations of the total lattice energy are not possible with $Z' = 3$ structures, PIXEL calculations on the various dimer interactions in the structure were performed. These show that, as in phases II and III, the strongest interaction is a stacking interaction. In phase IV all three independent molecules form C-H…π interactions by simple translation along the *b* axis. These are similar to those seen in phases II and III between the layers, though the interaction is not quite as strong in phase IV (phase II -20.6 kJ mol^{-1}; phase III -19.4, -19.5 kJ mol^{-1}; phase IV -17.6, -17.5, -16.5 kJ mol^{-1}). The next strongest interactions are the zig-zag interaction between molecules one and three (-13.4 kJ mol^{-1}), Figure 6.7, and the cone interaction between molecules one and two (-11.4 kJ mol^{-1}), Figure 6.4. Both of these interactions are stronger than those within the layers in phase II which will help balance out the weaker C-H…π stacking interactions.

6.4.3 Absence of Phase I

Phase I of mesitylene has not been observed under any conditions in these X-ray single crystal studies. Upon warming a crystal of phase II to 221 K the sample began to melt directly from this phase with no sign of it undergoing a transition to phase I, even after several hours above the transition temperature.

In neutron powder studies on mesitylene-d_{12}, the onset of the transition from phase II to phase I is observed at 190 K, however a pure sample is only obtained after annealing at 220 K, thus the transition does not proceed easily. This may explain why single crystals of phase II are seen to melt directly without undergoing a phase transition as the transition may be kinetically hindered or depend on imperfections.

As discussed above, the neutron powder pattern obtained at 180 K by Ibberson *et al.* (2007) does not correspond to phase IV therefore phase IV has never been observed in neutron powder studies and there are no other data available regarding its behaviour. All samples of phase IV melted directly at 221 K without undergoing a phase transition, though this does not rule out the possibility that it may be possible to transform to phase I as crystals of phase II also melted directly without undergoing a transition.

To our knowledge, phase I has never been observed as a single crystal.

6.5 Conclusions

The potential use of mesitylene as a neutron moderator material has sparked interest in the structure and dynamics of mesitylene in the solid phase. Raman spectroscopy, differential scanning calorimetry and, more recently, neutron powder diffraction have revealed rich phase diversity in mesitylene.

Neutron powder diffraction studies on mesitylene-d_{12} confirmed three phases, referred to as I, II and III downwards from the melting point; however the crystal structure of phase III has not been reported previously. In combination with an X-ray

single crystal study, the presence of a fourth phase, referred to as phase IIa, was revealed though only the unit cell volume was reported.

X-ray single crystal studies have revealed two different phases, phase II and a previously unknown phase which we have designated IV, can be obtained under the same set of crystallisation conditions. This has been observed for both mesitylene-h_{12} and mesitylene-d_{12}.

A single crystal of mesitylene-d_{12} was observed to undergo a phase transition from phase II to phase III at 90 K. The structure of phase III is triclinic with two molecules in the asymmetric unit. Structurally it is very similar to phase II, the difference being the molecules are twisted around in phase III to produce more sinusoidal layers. PIXEL calculations show that this change does not have a significant effect on the interaction energies within the layers though phase III is slightly more stable at 90 K.

Phase IV is monoclinic with three molecules in the asymmetric unit. The structure is very different to that of phase II though it was formed under the same experimental conditions. This phase has been found to be stable to 90 K and crystal melted directly from this phase when heated to 221 K. No data have been collected below 90 K.

Ibberson *et al.* (2007) reported the presence of a monoclinic phase with three molecules in the asymmetric unit and referred to it as phase IIa. Phase IV is consistent with this description and the cell volume reported however the neutron powder pattern observed does not correspond to phase IV therefore this powder pattern indicates the existence of five phases of mesitylene.

Phase I was not observed in any of the single crystal experiments. All crystals of phase II melted directly when heated to 221 K, even after being held above the transition temperature to phase I for several hours.

Complementary differential scanning calorimetry experiments are consistent with previous observations that the heating and cooling rate affects the temperature

induced behaviour of mesitylene (Natkaniec & Holderna-Natkaniec, 2002, ; Yamazaki *et al.*, 2000). Under the operating conditions of the instrument it is not possible to determine which phase is produced under each set of conditions as the instrument does not cool low enough to observe all known phase transitions.

X-ray single crystal studies have been used to determine further structural details for the phases of mesitylene including a new phase not previously observed in neutron powder diffraction studies. This further highlights the rich and unusual phase behaviour of mesitylene.

6.6 References

Altomare, A., Cascarano, G., Giacovazzo, C., Guagliardi, A., C, B. M., Polidori, G. & Camalli, M. (1994). *J. Appl. Crystallogr.* **27**, 435-435.

Betteridge, P. W., Carruthers, J. R., Cooper, R. I., Prout, K. & Watkin, D. J. (2003). *J. Appl. Crystallogr.* **36**, 1487.

Boese, R. & Nussbaumer, M. (1994). *Correlations, Transformations and Interactions in Organic Crystal Chemistry*. Oxford: Oxford University Press.

Bruker-Nonius (2006). *SAINT version 7.*

Dictionary of Organic Compounds, (1996). p. 6284 ed. London: Chapman and Hall, Electronic Publishing Division.

Dunitz, J. D. & Gavezzotti, A. (2005). *Angew. Chem. Int. Ed.* **44**, 1766-1787.

Frisch, M. J., Trucks, G. W., Schlegel, H. B., Scuseria, G. E., Robb, M. A., Cheeseman, J. R., J. A. Montgomery, J., Vreven, T., Kudin, K. N., Burant, J. C., Millam, J. M., Iyengar, S. S., Tomasi, J., Barone, V., Mennucci, B., Cossi, M., Scalmani, G., Rega, N., Petersson, G. A., Nakatsuji, H., Hada, M., Ehara, M., Toyota, K., Fukuda, R., Hasegawa, J., Ishida, M., Nakajima, T., Honda, Y., Kitao, O., Nakai, H., Klene, M., Li, X., Knox, J. E., Hratchian, H. P., Cross, J. B., Bakken, V., Adamo, C., Jaramillo, J., Gomperts, R., Stratmann, R. E., Yazyev, O., Austin, A. J., Cammi, R., Pomelli, C., Ochterski, J. W., Ayala, P. Y., Morokuma, K., Voth, G. A., Salvador, P., Dannenberg, J. J., Zakrzewski, V. G., Dapprich, S., Daniels, A. D., Strain, M. C., Farkas, O., Malick, D. K., Rabuck, A. D., Raghavachari, K., Foresman, J. B., Ortiz, J. V., Cui, Q., Baboul, A. G., Clifford, S., Cioslowski, J.,

Stefanov, B. B., Liu, G., Liashenko, A., Piskorz, P., Komaromi, I., Martin, R. L., Fox, D. J., Keith, T., Al-Laham, M. A., Peng, C. Y., Nanayakkara, A., Challacombe, M., Gill, P. M. W., Johnson, B., Chen, W., Wong, M. W., Gonzalez, C. & Pople, J. A. (2004). *Gaussian03.* Version Revision E.01. Wallingford CT.

Gavezzotti, A. (2003). *OPiX: A computer program package for the calculation of intermolecular interactions and crystal energies.* University of Milan, Italy.

Ibberson, R. M., Parsons, S., Natkaniec, I. & Holderna-Natkaniec, K. (2007). *Zeitschrift für Kristallographie* **Suppl. 26**, 575-580.

Natkaniec, I. & Holderna-Natkaniec, K. *Proceedings of ACoM-6 Workshop Jülich 2002*, edited by H. Conrad, pp. 103-111. Jülich: Matter and Materials.

Natkaniec, I., Holderna-Nathaniec, K. & Kalus, J. (2004). *Physica B* **350**, e651-e653.

Parsons, S. (2009). Private communication.

Sheldrick, G. M. (2004). *SADABS Version 2004-1*.

Unlu, K., Rios-Martinez, C. & Wehring, B. W. (1995). *J. Radioanal. Nucl. Chem.* **193**, 145-154.

Utsuro, m. & Sugimoto, M. (1977). *J. Nucl. Sci. Technol.* **14**, 390-392.

Yamazaki, M., Tanaka, M., Inoue, T., Suzuki, Y., Nibu, Y., Shimada, H. & Shimada, R. (2000). *Bull. Chem. Soc. Jpn.* **73**, 837-842.

Chapter 7
Conclusions

7.1 Conclusions

Simple small organic molecular systems are of interest as they allow intermolecular interactions to be studied in the absence of other effects and could provide vital information for developing computational techniques and understanding more complex systems. The compounds studied in this thesis illustrate that even seemingly simple molecules exhibit complex phase behaviour, therefore understanding the behaviour of even the simplest molecules with a single functionality could potentially provide a wealth of information on intermolecular interactions.

Varying the conditions of temperature is widely applied in polymorph screening however the use of pressure is not extensively used. Some of the compounds studied in this thesis highlight the importance of surveying the effect of both temperature and pressure in characterising the polymorphic behaviour of a compound. This is clearly illustrated by formamide which exhibits only one phase under conditions of varying temperature but has been found to exhibit four polymorphs in the pressure range 0.3 - 3.6 GPa.

The use of complementary experimental methods is often essential in fully characterising the phase behaviour of a compound, particularly when identifying subtle changes in structure. Identification of the changes in methyl group behaviour in N-methyl formamide and N,N-dimethyl formamide as a function of temperature was only revealed through combination of a number of techniques. Indeed, several compounds described in this thesis illustrate the significance of combining calorimetric and diffraction data.

Formamide and its methyl substituted analogues form a series of related compounds with only minor chemical modifications between them. Systematic studies of series of related compounds allow identification and, potentially, rationalisation of the phase transitions and structural motifs observed. Extending the studies of the compounds in this thesis to whole series of related compounds represents a large quantity of work. However the information on intermolecular interactions obtained

from such studies is of great significance in terms of being able to accurately model intermolecular interactions and, ultimately, accurately predict crystal structures.